DOKUZ EYLÜL UNIVERSITY
GRADUATE SCHOOL OF NATURAL AND APPLIED SCIENCES

ELECTROCHEMICAL MECHANICAL AND TRIBOLOGICAL PROPERTIES OF PLASMA ELECTROLYTIC OXIDE COATINGS ON TITANIUM ALLOYS

by
Kadir Cihan TEKİN

September, 2016
İZMİR

ELECTROCHEMICAL MECHANICAL AND TRIBOLOGICAL PROPERTIES OF PLASMA ELECTROLYTIC OXIDE COATINGS ON TITANIUM ALLOYS

A Thesis Submitted to the
Graduate School of Natural and Applied Sciences of Dokuz Eylül University
In Partial Fulfillment of the Requirements for the Degree of Doctor of Philosophy in Metallurgical and Materials Engineering,
Metallurgical and Materials Engineering Program

by
Kadir Cihan TEKİN

September, 2016
İZMİR

Ph.D. THESIS EXAMINATION RESULT FORM

We have read the thesis entitled **"ELECTROCHEMICAL MECHANICAL AND TRIBOLOGICAL PROPERTIES OF PLASMA ELECTROLYTIC OXIDE COATINGS ON TITANIUM ALLOYS"** completed by **KADİR CİHAN TEKİN** under supervision of **ASSOC. PROF. DR. UĞUR MALAYOĞLU** and we certify that in our opinion it is fully adequate, in scope and in quality, as a thesis for the degree of Doctor of Philosophy.

Assoc. Prof. Dr. Uğur MALAYOĞLU

Supervisor

Prof.Dr.Kazım ÖNEL

Thesis Committee Member

Prof. Dr. Rasim İPEK

Thesis Committee Member

Prof.Dr.Hüseyin ÇİMENOĞLU

Examining Committee Member

Doç.Dr.Murat Baydoğan

Examining Committee Member

Prof. Dr. Ayşe OKUR

Director

Graduate School of Natural and Applied Sciences

ACKNOWLEDGEMENTS

I am grateful to many people who have been part of my life and who have made this dissertation possible. Many of those individuals are listed below, however, many more have played a role in my development as a person and a scientist.

First and foremost, I would like to express my sincerest gratitude to my supervisor Assoc. Prof. Dr. Uğur MALAYOĞLU for his invaluable guidance and support throughout this work. I would also like to thank my committee members, Prof. Dr. Kazım ÖNEL and Prof. Dr. Rasim İPEK, for reviewing my work and offering valuable suggestions and sharing their visions about the content of my thesis.

I would like to express my sincere thanks to my parents for all their support throughout my work. The successful completion of this study would not have been possible without their constant love and encouragement.

Speical thanks to Assis. Prof. Dr. Mustafa EROL, Haydar KAHRAMAN, Serhan KÖKTAŞ, Ramazan DALMIŞ and Onur ERTUĞRUL for their collaboration in the laboratory studies and sharing their valuable experiences with me. I am most grateful to my friends, Mithat Kemal TOZAN and Hayri KESER for their invaluable assistance and kind friendship.

Kadir Cihan TEKİN

ELECTROCHEMICAL MECHANICAL AND TRIBOLOGICAL PROPERTIES OF PLASMA ELECTROLYTIC OXIDE COATINGS ON TITANIUM ALLOYS

ABSTRACT

Titanium and its alloys have been adopted as standard materials in aviation, biomedical and chemical industries owing to their outstanding properties involving high specific strength, high corrosion resistance and biocompatibility. But, an important shortcoming related to the application of titanium and its alloys is their poor wear resistance. When titanium slides against itself or other metals it tends to gall and cause adhesive wear damage. The high friction coefficient of titanium alloys may result in seizure of many tribological systems under high load such as bushings and bearings. In this study, oxide coatings on commercially pure titanium and Ti6Al4V alloys were produced using plasma electrolytic oxidation technique in order to enhance their electrochemical and tribological properties. Different electrolyte compositions were formulated to develop hard coating with less porosity and high load bearing capacity. Microstructure of coatings were investigated using scanning electron microscopy. Phase composition of coatings was identified by X-ray diffraction. Nano-indentation test was carried out to determine the micromechanical properties of the coatings. Scratch test was utilized to determine the adhesion strength of coatings. In order to investigate the tribological behavior of coatings, dry sliding wear tests were performed against steel and alumina balls. The electrochemical corrosion tests were conducted using potentiodynamic polarization and electrochemical impedance spectroscopy techniques in sodium chloride solution. Test results showed that the corrosion and wear resistance of titanium alloys can be increased considerably either by selecting a proper electrolyte composition or by application of a suitable post-treatment.

Keywords: Titanium alloy, plasma electrolytic oxidation, wear, corrosion, hardness

TİTANYUM ALAŞIMLARIN ÜZERİNDEKİ PLAZMA ELEKTROLİTİK OKSİT KAPLAMALARIN ELEKTROKİMYASAL MEKANİK VE TRİBOLOJİK ÖZELLİKLERİ

ÖZ

Titanyum ve alaşımları, yüksek özgül mukavemet, yüksek korozyon direnci ve biyouyumluluk gibi üstün özelliklere sahip olduğu için havacılık, biyomedikal ve kimya sanayilerinde standart malzeme olarak kabul görmüştür. Ancak, titanyum ve alaşımlarının kullanımıyla ilgili önemli bir eksikliği zayıf aşınma direncine sahip olmasıdır. Titanyum kendisine karşı veya diğer metallere karşı sürtündüğünde, birbirine yapışmaya eğilimlidir ve adeziv aşınma hasarına sebep olur. Titanyum alaşımlarının yüksek sürtünme katsayısı, burç ve rulman gibi yüksek yük altında çalışan birçok tribolojik sistemin aşınarak işlevsiz hale gelmesiyle sonuçlanmaktadır. Bu çalışmada, ticari saflıkta titanyum ve Ti6Al4V alaşımlarının elektrokimyasal ve tribolojik özelliklerini iyileştirmek amacıyla plazma elektrolitik oksidasyon yöntemi kullanılarak oksit kaplamalar üretilmiştir. Düşük gözenekliliğe ve yüksek yük taşıma kapasitesine sahip sert kaplama geliştirmek amacıyla farklı elektrolit bileşimleri oluşturulmuştur. Kaplamaların mikroyapısı elektron mikroskobuyla incelenmiştir. Kaplamaların faz bileşimi X-ışını kırınımıyla tespit edilmiştir. Kaplamaların mikro-mekanik özelliklerini belirlemek için nanoiz testi yapılmıştır. Kaplamaların yapışma mukavemetini belirlemek için kazıma testi kullanılmıştır. Kaplamaların tribolojik davranışını incelemek için çelik ve alumina bilyalara karşı kuru kaymalı aşınma testleri yapılmıştır. Potansiyodinamik polarizasyon ve elektrokimyasal empedans spektroskopisi teknikleri kullanılarak sodyum klorür çözeltisi içerisinde elektrokimyasal korozyon testleri yapılmıştır. Test sonuçları göstermektedir ki, titanyum alaşımların korozyon ve aşınma direnci gerek doğru bir elektrolit seçimi gerekse uygun bir son işlem uygulanarak önemli ölçüde arttırılabilir.

Anahtar kelimeler: Titanyum alaşımı, plazma elektrolitik oksidasyon, aşınma, korozyon, sertlik

CONTENTS

Page

Ph.D. THESIS EXAMINATION RESULT FORM ii
ACKNOWLEDGEMENTS iii
ABSTRACT iv
ÖZ v
LIST OF FIGURES ix
LIST OF TABLES xiv

CHAPTER ONE - INTRODUCTION 1

1.1 Background 1
1.2 Thesis Outline 2

CHAPTER TWO - PLASMA ELECTROLYTIC OXIDATION 4

2.1 Background 4
2.2 Historical Development of PEO Process 4
2.3 Coating Formation 8
2.3.1 Electrochemical Characteristics 8
2.3.2 Breakdown of Anodic Oxide Films 9
2.3.3 Discharge Characteristics 12
2.3.3.1 The Size and Spatial Density of Discharges 12
2.3.3.2 The Optical Emission Spectroscopy of Discharge Events 14
2.3.3.3 The Lifetime of Discharge Events 16

CHAPTER THREE - CORROSION PROPERTIES OF TITANIUM ALLOYS 17

3.1 Corrosion of Titanium and Its Alloys 17
3.2 Types of Corrosion 18
3.2.1 General Corrosion 18

3.2.2 Crevice Corrosion 18
3.2.3 Anodic Pitting 19
3.2.4 Hydrogen Uptake 20
3.2.5 Stress Corrosion Cracking 21
3.3 Corrosion Behavior of PEO Coatings 22

CHAPTER FOUR - TRIBOLOGICAL PROPERTIES OF TITANIUM ALLOYS 28

4.1 Adhesive Wear of Titanium Alloys 28
4.1.1 Electron Structure 28
4.1.2 Crystal Structure 30
4.1.3 Thermal Conductivity 32
4.1.4 Lubrication 33
4.2 Abrasive Wear of Titanium Alloys 34
4.3 Mechanical Properties and Wear Behavior of PEO Coatings 38

CHAPTER FIVE - EXPERIMENTAL DETAILS 46

5.1 PEO Processing Equipment 46
5.2 Specimen Preparation 47
5.3 Coating Thickness Measurement 48
5.4 Preparation of Cross-Section of Coating 48
5.5 Microstructural Investigation 49
5.6 Surface Profilometry 50
5.7 X-Ray Diffraction 51
5.7.1 Through-Thickness Phase Profile 52
5.7.2 Quantitative Phase Analysis 52
5.8 Electrochemical Corrosion Tests 53
5.8.1 Experimental Setup 53
5.8.2 Potentiodynamic Polarization 54
5.8.3 Electrochemical Impedance Spectroscopy (EIS) 57

5.9 Measurement of Hardness and Elastic Modulus 63
5.10 Scratch Test 65
5.11 Wear Test 67

CHAPTER SIX - RESULTS 70

6.1 Introduction 70
6.2 The Voltage-Time Response 70
6.3 Surface Morphology and Cross-Sectional Analysis 72
6.4 Phase Analysis 78
6.5 Electrochemical Corrosion Properties 85
6.5.1 Potentiodynamic Polarization 85
6.5.2 Electrochemical Impedance Spectroscopy 86
6.6 Mechanical Properties 90
6.6.1 Hardness Measurement and Nanoindentation 90
6.6.2 Scratch Test 93
6.7 Tribological Properties 101
6.7.1 Wear Behavior 101
6.7.2 Wear Mechanisms 107

CHAPTER SEVEN - CONCLUSIONS 112

REFERENCES 116

LIST OF FIGURES

Page

Figure 2.1 The current-voltage plot for PEO treatment 9

Figure 3.1 The comparison of the corrosion ranges of metals 17

Figure 4.1 Variation of friction coefficient of some metals rubbing against gold with the percent d-valence bond character. Sliding velocity: 0.7 mm/min, load: 1 g, temperature: 23°C and pressure: 10^{-8} Pa 30

Figure 4.2 Variation of friction coefficient of some metals with c/a lattice ratio. Vacuum: 10^{-9} mm of Hg, sliding velocity: 400 fpm, load: 1 kg, no external sample heating 32

Figure 4.3 Schematics of (a) a soft surface that is rubbed against a harder surface or a surface mounted with abrasive grits, and (b) loose abrasive grits entrapped between two mating surfaces, at least one of them is softer than the abrasive grits 35

Figure 4.4 Schematic views of abrasive wear processes due to plastic deformation 36

Figure 4.5 The ratio of microcutting to microploughing as a function of the ratio of the attack angle to the critical attack angle 37

Figure 5.1 Schematic of PEO processing equipment used in experimental studies . 46

Figure 5.2 Electrochemical cell used in corrosion studies 53

Figure 5.3 Tafel plot for activation controlled corrosion rates 55

Figure 5.4 A typical Tafel plot representing the linear extrapolations to OCP 56

Figure 5.5 Determining Tafel slopes from Tafel plots 56

Figure 5.6 Cycle nature of AC voltage 57

Figure 5.7 AC voltage-current phase angle 59

Figure 5.8 Electrical double layer for an uncoated, oxide-free corroding metal 60

Figure 5.9 Vector nature of voltage and current 61

Figure 5.10 Single time constant complex plane plot 62

Figure 5.11 Single time constant (a) Bode magnitude plot and (b) Bode phase plot 63

Figure 5.12 (a) Schematic of indentation cross-section and (b) typical load–displacement curve 65

Figure 5.13 Schematic example of progressive damage in scratch track in a progressive load scratch test 67
Figure 5.14 Schematic of CSM Instruments standard tribometer 68
Figure 6.1 Variation of voltage during PEO processing of CP-Ti and Ti6Al4V alloys in phosphate-based electrolyte 71
Figure 6.2 Voltage-time responses for PEO processing of Ti6Al4V in aluminate-based electrolytes 72
Figure 6.3 Surface morphology and cross-sections of coatings produced on CP-Ti and Ti6Al4V alloys using phosphate-based electrolyte 73
Figure 6.4 Surface morphology of coatings produced in aluminate-based electrolytes 74
Figure 6.5 Detailed SEM images showing the surface morphology of coatings formed in aluminate-based electrolytes 75
Figure 6.6 Cross-sectional SEM images of coatings produced on Ti6Al4V alloy using aluminate-based electrolytes 76
Figure 6.7 Surface morphology of coating with silane treatment and cross-section of coating with MoS_2 topcoat 77
Figure 6.8 XRD patterns of coatings produced on CP-Ti and Ti6Al4V alloys using phosphate-based electrolyte 79
Figure 6.9 XRD patterns of powder material that is obtained by rubbing the PEO coatings produced on Ti6Al4V alloy using aluminate-based electrolytes 80
Figure 6.10 Through-thickness phase profile of coatings produced in aluminate electrolyte 82
Figure 6.11 Through-thickness phase profile of coatings produced in aluminate-phosphate electrolyte 82
Figure 6.12 Through-thickness phase profile of coatings produced in aluminate-pyrophosphate electrolyte 83
Figure 6.13 Through-thickness phase profile of coatings produced in aluminate-tartrate electrolyte 83
Figure 6.14 Through-thickness phase profile of coatings produced in aluminate-tungstate electrolyte 84

Figure 6.15 Through-thickness phase profile of coatings produced in aluminate-borate electrolyte 84
Figure 6.16 Potentiodynamic polarization graphs of coatings tested in a naturally aerated 3.5 wt.% NaCl solution at a scan rate of 0.25 mV/s at ambient temperature 86
Figure 6.17 (a) Nyquist and (b) Bode plots of bare CP-Ti alloy in wt.% 3.5 NaCl solution 88
Figure 6.18 (a) Nyquist and (b) Bode plots of as-prepared coating on CP-Ti in wt.% 3.5 NaCl solution 88
Figure 6.19 (a) Nyquist and (b) Bode plots of thin coating on CP-Ti with silane treatment in wt.% 3.5 NaCl solution 88
Figure 6.20 Equivalent circuit models that were used in fitting the impedance spectra of (a) bare CP-Ti, (b) CPT-PH and CPT-PH-Silane coatings .. 89
Figure 6.21 (a) The hardness and (b) elastic modulus values that were measured by in-plane indentations on cross-section of coatings produced in aluminate-based electrolytes 92
Figure 6.22 The Vickers hardness values that were measured by out-of-plane indentations on polished surfaces of coatings produced in aluminate based electrolytes 93
Figure 6.23 Supplementary data graphics which were obtained during scratch tests of coatings formed in phosphate-based electrolyte up to a maximum load of 30 N 95
Figure 6.24 Optical microscope images of scratch tracks on coatings formed in phosphate electrolyte with and without top-coat. The maximum applied load and the scratch length are 30 N and 6 mm, respectively. 95
Figure 6.25 Optical microscope images of scratch tracks on polished coatings of 25 μm thickness. The maximum applied load and the scratch length are 30 N and 6 mm, respectively 96
Figure 6.26 Supplementary data graphics which were obtained during scratch tests of polished coatings of 25 μm thickness formed in aluminate-based electrolytes up to a maximum load of 30 N 97

Figure 6.27 Optical microscope images of scratch tracks on polished coatings of 25 μm thickness. The maximum applied load and the scratch length are 70 N and 10 mm, respectively 99
Figure 6.28 SEM images of scratch tracks that were formed using a maximum load of 30 N on the coatings which were formed in phosphate-based electrolyte..... 100
Figure 6.29 SEM images of scratch track that was formed using a maximum load of 30 N on the polished coating which was formed in aluminate-borate electrolyte. The image on the left hand-side represents the first cohesive damage event such as cracking or cohesive chipping, and the image on the right hand-side corresponds to the endpoint of scratch track 100
Figure 6.30 SEM images of scratch track that was formed using a maximum load of 70 N on the polished coating which was formed in aluminate electrolyte..... 101
Figure 6.31 (a) Wear rates of coatings formed in phosphate-based electrolyte against AISI 52100 steel ball at an applied load of 10 N and (b) wear rates of AISI 52100 steel ball rubbed against polished coatings (25 μm) formed in aluminate-based electrolytes at an applied load of 10 N.... 102
Figure 6.32 Wear profiles of coatings formed in phosphate-based electrolyte against AISI 52100 steel ball at an applied load of 10 N..... 102
Figure 6.33 Friction coefficient of bare titanium alloys and coatings formed in phosphate-based electrolyte with and without top-coat against AISI 52100 steel ball at an applied load of 10 N..... 103
Figure 6.34 Friction coefficient of polished coatings (25 μm) formed in aluminate-based electrolytes against AISI 52100 steel ball at an applied load of 10 N..... 104
Figure 6.35 Wear rates of polished coatings (25 μm) formed in aluminate-based electrolytes against aluminum oxide ball..... 105
Figure 6.36 Wear profiles of polished coatings (25 μm) formed in aluminate-based electrolytes against aluminum oxide ball..... 106
Figure 6.37 (a,b) Macro and detailed SEM images of worn coatings produced on Ti6Al4V using phosphate-based electrolyte without top-coat and (c,d)

detailed SEM images of worn coatings produced on Ti6Al4V using phosphate-based electrolyte with MoS_2 top-coat..... 108
Figure 6.38 (a,b) Macro and detailed SEM images of wear track on polished coating (25 μm) produced on Ti6Al4V using aluminate electrolyte..... 109
Figure 6.39 The optical microscope image of flattened surface of steel ball rubbed against PEO coating produced on Ti6Al4V using aluminate electrolyte 109
Figure 6.40 (a) Macro and (b) detailed SEM images of wear track obtained by applying 1 N normal load on polished coating (25 μm) formed in aluminate electrolyte..... 110
Figure 6.41 (a) Macro and (b) detailed SEM images of wear track obtained by applying 2 N normal load on polished coating (25 μm) formed in aluminate electrolyte..... 110
Figure 6.42 (a) Macro and (b) detailed SEM images of wear track obtained by applying 3 N normal load on polished coating (25 μm) formed in aluminate electrolyte..... 111
Figure 6.43 (a) Macro and (b) detailed SEM images of wear track obtained by applying 4 N normal load on polished coating (25 μm) formed in aluminate electrolyte..... 111

LIST OF TABLES

Page

Table 5.1 Experimental parameters used to produce PEO coatings on titanium alloys 47
Table 6.1 Surface roughness and thickness of coatings 78
Table 6.2 Relative amounts of phase constituents in PEO coatings produced using aluminate-based electrolytes 81
Table 6.3 Corrosion properties of coatings that were obtained by Tafel extrapolation 86
Table 6.4 EIS fitting results obtained using the equivalent circuit models 89
Table 6.5 Critical load values that indicate the first cohesive damage event (L_{c1}) and spallation of coating (L_{c2}) 98

CHAPTER ONE
INTRODUCTION

1.1 Background

Titanium alloys have been adopted as standard materials in aviation, biomedical and chemical industries owing to their outstanding properties involving high specific strength, high corrosion resistance and biocompatibility. These alloys are commonly used for producing corrosion resistant equipment such as valves, fittings, pipes and other equipment in the chemical process industry, heat exchanger and condenser tubes in nuclear power generation and deep sea production risers in petroleum industry. They have also been used in manufacturing the landing gear parts of aircrafts as a replacement of steel, where aluminum and magnesium alloys could not possess the desired mechanical properties.

Titanium alloys have an immunity to corrosion associated with many natural corrosive environments, including seawater and body fluids. However, when the pieces of equipment made from titanium alloys are in contact with more electrochemically active materials such as aluminum, magnesium, zinc or copper, a galvanic couple is developed and the counter material corrodes preferentially due to the extremely passive nature of titanium. In order to prevent galvanic coupling, the contact of titanium with other dissimilar metals are avoided or the contact surfaces are isolated with suitable coating techniques. Another shortcoming associated with titanium is galling. When titanium slides against itself or other metals it tends to gall and cause adhesive wear damage. Accordingly, cold-welding of threaded joints made of titanium makes disassembly difficult. The high friction coefficient of titanium alloys may result in seizure of many tribological systems under high load such as bushings and bearings. In aerospace applications, the parts made of titanium undergo fluctuating major loads and vibrations which cause a potential fretting wear damage. The small slip amplitudes at the mating surfaces may also lead to the loss of interfacial fits or clearances.

In order to prevent the problems mentioned above, various surface modification technologies have been adopted including physical vapor deposition (PVD), chemical vapor deposition (CVD), thermal spray, laser cladding, anodizing and plasma electrolytic oxidation (PEO). More recently, the PEO processing of light alloys has seen widespread interests due to its unique capabilities including the possibility of obtaining a highly adherent ceramic-like conversion oxide layer on the metal parts with complex shapes and irregular surface geometry in relatively short processing periods at nearly ambient substrate temperature. To date, there have been several studies concerning the electrochemical, mechanical and tribological properties of PEO coatings on titanium alloys. Some of these studies focused on the development of hard and wear resistant oxide coatings on titanium alloys and compare their tribological performance with the uncoated substrates. It has been reported that the load bearing capacity of coatings is improved with increasing thickness and this resulted in enhanced wear resistance. In previous studies, it has been also reported that further improvement in the wear resistance was achieved by applying solid lubricant top-coats such as graphite and PTFE on PEO coating.

In this study, commercially pure titanium (CP-Ti) and Ti6Al4V alloys were coated by Keronite G2 PEO equipment using various electrolyte compositions. The tribological behavior of PEO coatings were assessed using different counter materials such as AISI 52100 steel and aluminum oxide under dry sliding condition. To investigate the effect of solid lubrication on the frictional properties, MoS_2 friction modifier was applied on PEO coatings. Electrochemical corrosion properties of coatings were investigated in sodium chloride solution at room temperature using potentiodynamic polarization and electrochemical impedance spectroscopy (EIS) methods.

1.2 Thesis Outline

Chapter 2 provides a brief description of plasma electrolytic oxidation, including its historical development and coating formation mechanism. A literature review is

presented on how discharges are initiated. Detailed information on the discharge characteristics are given.

Chapter 3 presents the corrosion behavior of titanium alloys and provides a literature review on the corrosion of PEO coatings produced on titanium and its alloys.

Chapter 4 presents the tribological properties of titanium alloys and provides a literature review on mechanical properties and wear behavior of PEO coatings produced on titanium and its alloys.

Chapter 5 includes the experimental techniques used in this study. These involve specimen preparation, PEO coating process, phase analysis using X-ray diffraction (XRD), microstructural characterization using scanning electron microscopy (SEM), nano-indentation, electrochemical corrosion test, scratch test and wear test.

Chapter 6 consists of the experimental results of structural examination, electrochemical corrosion, mechanical and wear tests. Surface morphology and cross-sectional microstructures of PEO coatings are revealed using SEM. Through-thickness phase composition is determined and the quantitative phase analysis is conducted. Structural properties of coatings produced in different electrolytes are compared with each other and the effect of microstructure and phase composition on the mechanical properties of coatings are discussed. Electrochemical corrosion resistance of bare and coated titanium alloys is determined using the corrosion rate and impedance values. The wear behavior of bare and coated titanium alloys that were rubbed against different counter materials including steel and aluminum oxide is studied. The effect of solid lubricant top-coat on the tribological behavior of PEO coating is studied. The wear rates of bare and coated titanium alloys are determined by measuring the total volume loss.

Chapter 7 presents the main conclusions that can be drawn from this work and suggestions for the future work.

CHAPTER TWO
PLASMA ELECTROLYTIC OXIDATION

2.1 Background

Plasma electrolytic oxidation (PEO) is a generic term which is used to describe a variety of high voltage electrochemical processes, and refers to the same process as “micro arc oxidation”, “anodic spark deposition”, “microplasma oxidation” and “plasma anodizing”. It is a promising and environmentally friendly coating method which is based on plasma-assisted anodic oxidation that forms a protective and well adhered ceramic oxide coating on “valve metals” (magnesium, aluminum and titanium) which act as diodes or rectifiers after the oxide layer has grown on their surfaces.

The PEO process involves creation of a plasma discharge around a component which is immersed in an electrolyte containing various types of anodic inhibitors which promote the growth of oxide film on the metal surface. The mechanism of oxide layer formation during the PEO process represents very complex combinations of oxide growth with subsequent fusing, re-crystallization of the oxide film and also involves partial substrate metal dissolution at microscopic levels. While the PEO process can be considered as very aggressive due to extensive plasma discharges on the surface and oxide eruptions at very high local pressures (believed to be several GPa), these discrete processes occur at microscopic levels and the treated component including the working surface receive no heat affected zones or distortion.

2.2 Historical Development of PEO Process

Discharge phenomenon during the anodizing of metals was first observed in 1880 by Sluginov, who investigated the behavior of metal electrodes in aqueous electrolytes under high voltages (Yerokhin, Nie, Leyland, Matthews & Dowey, 1999). In 1930’s, a more detailed study on “spark discharge” was conducted by Günther-Schulze and Betz. They worked on the theory of electrolytic valve action

(Güntherschulze & Betz, 1932) and investigated the spark discharge phenomena during the anodizing of aluminum and tantalum (Güntherschulze & Betz, 1937). They noted that the dielectric breakdown of electrolytic barrier films under extreme electrical field strengths causes sparks which appear and disappear while being distributed over the entire surface of the anode, giving the impression of movement. They observed that the sparks increase in size and become less mobile as the voltage increases towards the maximum.

Spark discharge during anodizing soon applied to obtain protective oxide coatings on metals such as aluminum, magnesium and tantalum. Brennan & Leona (1944) patented a high-voltage spark discharge process to obtain corrosion resistant coatings on film forming metals including aluminum and magnesium. Another early patent of spark discharge is assigned to Finsterwalder Isolations GmbH (1954) for the production of oxide coatings on aluminum and its alloys. This process yields a snow-white oxide coating similar in appearance to sintered porcelain and having a high hardness value, which makes it suitable for grinding or honing of hard metals. In 1955, a patent for the electrolytic coating of magnesium and its alloys in an alkaline electrolytic bath was issued to Harry A. Evangelides, who is also the inventor of HAE process, named after him (Evangelides, 1955). A similar patented spark discharge process, named DOW 17, was developed by DOW Chemical Company for producing protective oxide coating on magnesium and its alloys in an acidic electrolytic bath (Long, 1959). Both of these low-voltage spark discharge processes, HAE and DOW 17, soon became two of the most commonly used anodizing processes for magnesium. However, these coatings have a porous structure, which is detrimental to the mechanical properties and further need an application of sealant for desired corrosion resistance. In addition to providing improved corrosion and wear resistance, spark discharge process was also utilized for obtaining an oxide coating with heat radiation ability on tantalum anode of the type used in electron tubes (Dwyer, 1955).

Since then, the main research efforts have been pursued by Gruss, McNeill and coworkers at the Frankford Arsenal in Philadelphia, and by Brown, Wirtz, Kriven

and coworkers in the University of Illinois at Urbana-Champaign. McNeill (1958) utilized spark discharges to synthesize cadmium niobate ($Cd_2Nb_2O_7$) on a cadmium anode in an aqueous solution of potassium niobate. Subsequently, they took out a patent for “method of making cadmium niobate” in 1958 (Mcneill & Nordblom, 1958). This study opened the way for obtaining complex oxide structures involving both the anions from the electrolyte and constituents from the anode metal. They also produced CdS films on cadmium anodes using a solution of $Na_2S{\cdot}9H_2O$ in ethanol (McNeill, Gruss & Husted, 1965). This study demonstrated the feasibility of using non-aqueous electrolytes in spark discharge process. Later on, Mcneill & Gruss (1966) studied a wide range of anode-electrolyte combinations and filed a patent for "anodic spark reaction processes and reactions", which describes the application of hard alumina, silicate or tungsten trioxide-based coatings to a variety of metals. Further study for obtaining crystalline oxide structures involving electrolyte species was conducted by Brown, Kuna & Van (1971). They reported that the coatings produced in the aluminate electrolyte contained a greater proportion of crystalline phase than those produced in the silicate electrolyte. The crystalline material in the coatings produced in the aluminate electrolyte was primarily α–Al_2O_3 with minor amounts of β and possibly γ forms. Crystalline phases in the coatings produced in the silicate electrolyte were either oxidized anode metal or compounds of these oxides and silica. In another study by Gruss & Mackus (1973), it is shown that several rare earth metals are suitable for anodizing under spark discharges in both sodium aluminate and sodium silicate electrolytes. Following their study, Van, Brown & Wirtz (1977) proposed a mechanism for anodic spark deposition.

In 1970s and 1980s, significant research and developments were carried out by Markov and coworkers in the USSR, and by Krysmann, Kurze, Dittrich and coworkers in East Germany. Researchers were mainly focused on the development of the conventional anodizing of aluminum. During 1970s, anodic oxidation of aluminum utilizing spark discharges was studied and improved by Markov and co-workers (Markov & Markova, 1976; Nikolaev, Markov & Peshchevitskii, 1977). They used ‘microarc oxidation’ term for the spark discharge process (Markov, Tatarchuk & Mironova, 1983) and studied the process in many aspects including the

transition stages in voltage-time response and the effect of anodic and cathodic voltage pulses on the physico-mechanical characteristics and wear resistance of coatings (Belevantsev, Markov, Terleeva & Shulepko, 1989; Karanik, Markov, Minin, Nikolaev & Peshchevitskij, 1977; Malyshev et al., 1985; Markov, Belevantsev, Slonova & Terleeva, 1989; Markov, Belevantsev & Terleeva, 1988; Markov, Shulepko & Terleeva, 1989). Their studies were the origin of Russian research into the spark discharge process. The German process developed by Kurze, Krysmann and co-workers is called "anodic oxidation by spark discharge" (the German acronym for which is ANOF “Anodische Oxidation unter Funkenentladung”). Kurze and co-workers took out the early German patents related to the anodic oxidation of aluminum and titanium under spark discharges (Kurze, Krysmann & Marx, 1980; Kurze, Marx, Krysmann & Dittrich, 1982). They studied the structure and properties of ANOF coatings produced on aluminum anodes using a variety of electrolytes (Dittrich, Krysmann, Kurze & Schneider, 1984). They found that the adhesion strength between the substrate and coating was higher than the internal bond strength of the coating. In other words, the coatings failed in cohesion rather than adhesion, including many cracks within the coating. They also reported potential application fields of ANOF coatings including medical industry, electrical engineering, electronics, and vacuum engineering (Kurze, Krysmann & Schneider, 1986). In another study by the same researchers, it is indicated that a wide range of colors can be obtained on aluminum anodes adding different metal salts into the basic electrolyte (Kurze, Krysmann, Schreckenbach, Schwarz & Rabending, 1987).

Further studies in more detail on the development of PEO process were conducted by Snezhko and co-workers (Snezhko, Papanova, Tikhaya & Tchernenko, 1990; Snezhko, Tikhaya, Udovenko & Tchernenko, 1991), Markov and co-workers (Belevantsev et al., 1998; Markov & Shulepko, 1995; Markov, Shulepko, Terleeva & Slonova, 1994; Markov, Slonova & Terleeva, 1997; Slonova, Terleeva & Markov, 1997; Slonova, Terleeva, Shulepko & Markov, 1992), Gordienko and co-workers (Gnedenkov, Sinebryukhov, Skorobogatova & Gordienko, 1998; Gordienko, Nedozorov, Zavidnaya & Yarovaya, 1991; Krisanfova, Volkova, Gnedenkov, Kaidalova & Gordienko, 1995; Rudnev, Gordienko, Kurnosova & Ovsyannikova,

1991; Yarovaya, P.S., Rudnev, Nedozorov & Zavidnaya, 1994), and Hradcovsky and co-workers (Hradcovsky, 1978, 1987; Hradcovsky & Bayles, 1974; Hradcovsky & Bayles Jr., 1976). The detailed studies in Russia and Germany improved the PEO technique and led to its commercialization. Currently, PEO technique is employed for protecting the surface of light alloys against corrosion and wear in many engineering applications.

2.3 Coating Formation

2.3.1 Electrochemical Characteristics

Yerokhin, & et al. (1999) overviewed electrical plasma process and described the current-voltage characteristics during the PEO process. Figure 2.1 represents the current-voltage characteristics of a system where oxide film formation occurs during the PEO process. Firstly, at relatively low voltages ($<U_1$), the electrochemical system conforms to Faraday's laws and the current-voltage characteristics of the cell vary according to Ohm's law. Thus, the voltage increases proportionally to the current in the region from 0 to U_1. In this region, the passive film formed on valve metal surface grows as the applied voltage increases. At U_2, which corresponds to the corrosion potential of the metal, the previously formed passive film begins to dissolve. Then, in the region from U_2 to U_3, which is the conventional anodizing stage, repassivation occurs and a porous insulation film with a columnar structure perpendicular to the metal substrate is formed.

At point U_3, which corresponds to the breakdown potential of the oxide film, the dielectric breakdown occurs by impact or tunneling ionization in some scattered weak regions across the oxide film, accompanied by the phenomenon of spark discharges. In this case, a large number of fine and uniform sparks are generated on the metal surface. These move rapidly across the surface of oxide film, facilitating its continued growth. At point U_4, the mechanism of impact ionization is supported by the onset of thermal ionization processes. In the region from U_4 to U_5, microarc discharges occur within the oxide film, gradually building up the coating thickness.

Above the point U_6, the microarc discharges occurring throughout the film transform into powerful arcs, which may be destructive and inhibit further growth of the oxide film. To obtain high-quality coatings, this arc discharge stage should be avoided as far as possible.

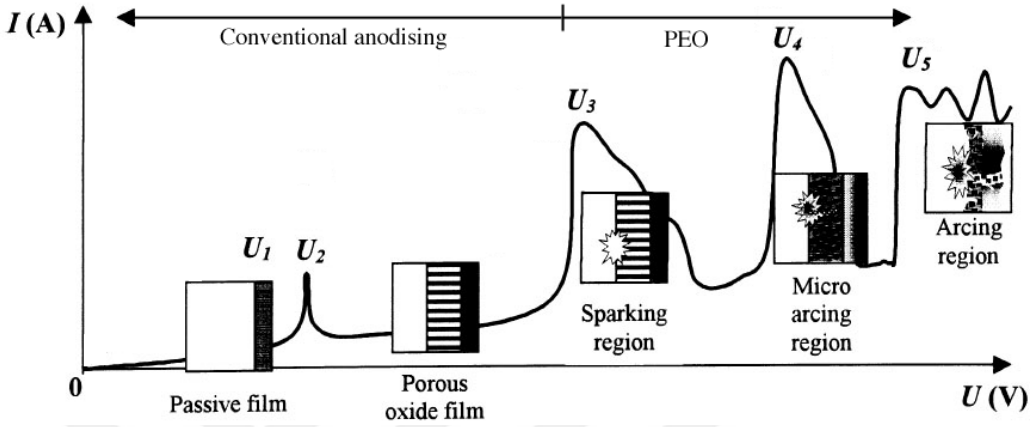


Figure 2.1 The current-voltage plot for PEO treatment (Yerokhin et al., 1999)

2.3.2 Breakdown of Anodic Oxide Films

There are mainly three types of breakdown mechanisms in solid dielectrics, namely, thermal, electrochemical and electrical breakdown. When an electric field is applied to a dielectric, conduction current flows through the material. This current heats up the dielectric and increases its temperature. During the application of the electric field, the heat generated is transferred to the surrounding medium by conduction and radiation. Equilibrium is reached when the heat generated is equal to the heat dissipated. If the heat generated exceeds the heat dissipated, thermal breakdown occurs, resulting in local melting. In presence of air and other gases, dielectric materials undergo chemical changes when subjected to continuous electrical stresses. Consequently, the electric insulation property of dielectric material deteriorates, causing electrochemical breakdown phenomenon.

Electrical breakdown is assumed to be electronic in nature and occurs in a very short time of the order of 10^{-8} s. Von Hippel (1937) proved that the electrical breakdown in solid dielectrics occurs through the mechanism of electron impact

ionization. When an electric field is applied, electrons gain energy and cross the forbidden gap from the valance to the conduction band. Above a certain critical electric field, the conduction electrons gain sufficient energy to ionize the negative ions of the lattice and liberates electrons from the lattice atom by collisions. This process is repeated again and again causing the formation of an electron avalanche sweeping through the crystal towards the anode and eventually breakdown occurs similarly as in gases.

The dielectric breakdown of the growing anodic oxide film is the common mechanism for the initiation of discharges. According to Wood & Pearson (1967), the avalanche type of breakdown as suggested by Von Hippel (1937) is suitable to explain the initiation of discharges during anodic oxidation of valve metals. Electrons supplied to the oxide by the electrolyte are multiplied by their interaction with atoms in the oxide, giving ionization, and eventually cause a large current to flow through the oxide, resulting in sparking. However, the presence of an electrolytic contact makes the breakdown features quite different from those of dry dielectric involving metal/anodic film/metal system.

According to Vijh (1971), dielectric breakdown and sparking only occurs after a certain critical thickness of the oxide has been reached at high voltages during anodizing. At this point, the side reactions such as oxygen evolution undergo a change in mechanism from tunneling to avalanche multiplication, because the avalanche multiplications provide a path of lower activation energy for the oxygen evolution reaction.

There have been several electron avalanche models for the electrical breakdown of anodic oxide films, however, the major differences in each model arise from the source of the primary electron current. The first attempt to propose a quantitative model for the electrical breakdown of anodic films is made by Ikonopisov (1977). According to this model, the primary electron current is directly injected from the electrolyte into the anodic oxide film either by Fowler-Nordheim (tunnel) or a Schottky mechanism. The electrons are then accelerated by the high electric field to

achieve a sufficient energy to free other electrons by impact ionization of the lattice atoms in the oxide, thus an avalanche multiplication occurs. In Ikonopisov's model, the current measured during anodic oxidation in electrolytes, which do not dissolve the oxide film remarkably, consists of two components, namely the ionic current and electronic current. The ionic current results from the movement of metal and oxygen ions under the influence of the electric field, whereas the electronic current is due to the occurrence of reactions of electron transfer at the oxide film/electrolyte interface, such as oxygen evolution. The ionic current initiates the growth of the anodic film, however the electronic current through the anodic oxide film does not have an influence on its thickness. It has been concluded that the electronic current, usually called "leakage current", is dependent on the oxide nature, as well as the composition and conductivity of electrolyte (Ikonopisov & Elenkov, 1978). Using an empirical equation, which includes the electronic current, it has been demonstrated that the breakdown voltage is dependent on the electrolyte resistivity. The breakdown occurs after the anodic film has reached a critical thickness sufficient to cause an increase of the electronic current up to a critical value.

The role of electrolyte anions on breakdown process, which is uncertain in Ikonopisov's model, is taken into account by Albella, Montero & Martínez-Duart (1984). It is assumed that the primary electron current originates from the incorporated electrolyte species into the oxide film during anodizing, instead of being injected through the electrolyte/oxide interface. The electrolyte species may act as impurity centers close to the oxide conduction band, so that they can act as a source of electrons, which can be released from these centers by a field-assisted Poole-Frenkel mechanism. In this model, the primary electron current is considered to be only a fraction of the current consumed in the incorporation of the oxyanions, which is also assumed to be a certain proportion of the anodizing current. According to these statements, a quantitative model for the calculation of the breakdown voltage and primary electron current has been given by Albella, Montero & Martinez-Duart (1987). According to this model, the breakdown voltage decreases with the logarithm of the anion concentration in the electrolyte. This model also explains the change in breakdown voltage when the metal successively anodized in different electrolyte

compositions (Albella, Montero, Fernandez, Gomez-Aleixandre & Martínez-Duart, 1985). When the metal first anodized until breakdown in a concentrated electrolyte, the primary electron current is that corresponding to this concentrated electrolyte. If the anodized metal is then immersed in a dilute electrolyte and subsequently anodized, the primary electron current is decreased to a new value and hence the avalanche current is also decreased. Consequently, the oxide grows further until a new critical breakdown voltage corresponding to the last electrolyte is achieved.

Di Quarto, Piazza & Sunseri (1988) proposed an alternative model for the injection of the primary electrons of the avalanche from the electrolyte into the oxide, while maintaining the general basis of the Ikonopisov's model. According to this model, it has been assumed that the primary electrons injected at the electrolyte/oxide interface originates from the oxidation reaction of the -OH radicals adsorbed on the oxide surface. The primary electron current has been assumed to be influenced by the double layer potential at the interface, which is in turn determined by the electrolyte concentration. This model also explains the independence of the breakdown voltage on the electrolyte pH.

2.3.3 Discharge Characteristics

Since the spark discharges determine thermal and chemical conditions, and influence the microstructure, surface morphology, and phase composition of the coatings, it is essential to understand the discharge behavior to characterize the PEO process.

2.3.3.1 The Size and Spatial Density of Discharges

Discharges occur at discrete weak (frequently thinner) sites of the oxide film, where the dielectric breakdown field strength is surpassed. The size and spatial density of discharges reported in the literature have a wide range of values. Sundararajan & Rama Krishna (2003) measured the diameter of micropores on SEM images and associated them with the size of discharge channels. According to their

results, the average size of the discharge channels was about 1.3 μm at the first minute of the processing time, then increased to about 2.4 μm over 30 minutes. He also presented the variation of density of discharge channels as a function of time. At the first minute of the process the discharge density is of the order of 1.1 x 10^{16} m^{-2}, but gradually decreases to about 10^{15} m^{-2} after 10 min. Since the micropores on SEM image represents the total discharge channels formed after a period beginning from the PEO processing, this calculation method does not give the instantaneous spatial density of discharges. Thus, real-time imaging of discharges is further studied to determine the spatial density of discharges more precisely.

Yerokhin et al. (2003) recorded the discharges occurring on an aluminum alloy H30T by a video camera with 10x magnification at 24 Hz frame rate. According to the image analysis results, the micro discharge spatial density decreases from an initial density of 3.2 x 10^{6} m^{-2} to 7.7 x 10^{5} m^{-2} over 65 minutes. The average cross-sectional area of discharges is in the range from 0.01 mm^2 to 1.35 mm^2. If the discharge channel is assumed to be circular, then the diameter of discharge channels is found in the approximate range from 100 μm to 1.3 mm. Discharge areas have been reported from PEO processing of titanium (99.5% purity), which, if again assumed to be circular, would indicate discharge diameter nearly in the range from 180 μm to 880 μm. (Stojadinović, Vasilić, Petković & Zeković, 2011). In another study by Matykina, Berkani, Skeldon & Thompson (2007), real-time images of discharges during PEO processing of titanium (3000 ppm Fe, 750 ppm O, 55 ppm N, <800 ppm C) for 960 s were recorded utilizing a camera recorder. During PEO process, the precision of the measurements was limited by the frame interval of 40 ms and the shutter speed of 10 ms. The calculated discharge size was in the range from 80 μm to 380 μm. The discharge density was about 5 x 10^{6} m^{-2} s^{-1} at about 160 s from the beginning of the process. It increased to 3 x 10^{7} m^{-2} s^{-1} after 760 s then decreased slightly to 2 x 10^{7} m^{-2} s^{-1} after about 920 s. In another study, using a digital camera having a shutter speed of 1 ms and 0.5 ms, the discharge diameter is found in the range from 70 μm to 1 mm (Cheng, Wu, Matykina, Skeldon & Thompson, 2012).

The video recorders used in previous studies are limited to observe long-lived discharges due to the low recording speed. Unlike above studies, Arrabal, Matykina, Hashimoto, Skeldon & Thompson (2009) used a high speed camera, which has a shutter speed of 1/fps and a maximum recording speed of 20,000 frames per second (fps), to record real-time images of discharges on various magnesium alloys including commercially pure magnesium (99.9%), magnesium/aluminum/zinc, magnesium/zinc/copper and magnesium/rare-earth containing alloys. The discharge density calculated using the real time images taken at 5400 fps during a period of 185 μs was in the range from 8 x 10^4 m^{-2} to 6.3 x 10^5 m^{-2}. Further study on PEO processing of an aluminum alloy revealed that the discharge frequency falls from initial values in the range 3-3.5 x 10^8 m^{-2} s^{-1} to about 10 mm^{-2} s^{-1} by the end of the process (Dunleavy, Curran & Clyne, 2013).

2.3.3.2 The Optical Emission Spectroscopy of Discharge Events

During the last decade, optical emission spectroscopy is widely employed for studying the discharge events in PEO processing. This technique is based on collecting the light emission generated during the spark discharge process and identification of characteristic spectral lines in order to specify the ionized elements and estimate the electron density and temperature in the discharge channel.

In an early OES study by Kharitonov, Gutsevich, Novikov & Fridman (1988), the chemical processes in a discharge channel was proposed and the complex structure of the discharge channel, in which a hot core (of 6800-9500 K) and cold circumferential area (of 1600-2200 K) was identified. Then, the physical properties of the plasma within the discharge channel were investigated by Klapkiv (1996), and the chemical reactions taking place within a discharge channel, and the internal structure of the plasma, were also later discussed by Klapkiv (1999). Klapkiv, Nykyforchyn & Posuvailo (1995) calculated that the plasma electron temperature in a discharge channel is in the range from 6600 to 7100 K, which is nearly similar to that obtained by Kharitonov et al. (1988), and the plasma electron density is in the range from 3.2 x 10^{22} to 7 x 10^{22} m^{-3}. He also proposed a plasma structure, nearly

similar to that proposed by Kharitonov, comprising a central hot core containing free electrons, ionic and atomic species, surrounded by lower temperature areas, in which different plasma constituents and reactions are taken place. Dunleavy, Golosnoy, Curran & Clyne (2009) reported that plasma emission spectra are indicative of there being two distinct regions in a discharge channel, a central hot core of high temperature (about 16.000 ± 3500 K), with a high plasma electron density (about 5 x 10^{17} cm^{-3}), and a peripheral region, probably extending into the surrounding electrolyte, which is much cooler (in the range from 3000 to 4000 K) and less dense (about 10^{15} cm^{-3}). This evidence supports the earlier results obtained by Kharitonov et al. (1988) and Klapkiv (1999).

Hussein and co-workers studied the OES of spark discharges during PEO processing of commercially pure aluminum and AJ62 magnesium alloys (Hussein, Nie & Northwood, 2010, 2013). In case of aluminum substrate, the intensity ratio of the recorded Al I (396.2 nm) to Al I (309.1 nm) spectral lines was used to calculate the plasma electron temperature, whereas the intensity ratio of H_α (656.3 nm) to H_β (486.1 nm) Balmer lines was utilized to calculate the electron temperature of spark discharges on AJ62 magnesium alloy. The measured plasma temperature was in the range from 4000 to 7000 K for commercially pure aluminum and in the range from 4000 to 5800 K for AJ62 magnesium alloy.

Stojadinovic and co-workers investigated the discharge events using OES on various metals including aluminum (Jovovic, Stojadinovic, Sisovic & Konjevic, 2011), magnesium (Jovović, Stojadinović, Šišović & Konjević, 2012), tantalum (Stojadinović, Jovović, Petković, Vasilić & Konjević, 2011) and titanium (Stojadinović, Vasilić, et al., 2011). They observed that the analysis of H_β line shape indicates the presence of two types of discharges during PEO processing. They calculated that the plasma electron densities according to H_β Balmer line were 0.8 x 10^{21} m^{-3} and 2.5 x 10^{22} m^{-3} for aluminum, 1.2 x 10^{21} m^{-3} and 2.3 x 10^{22} m^{-3} for magnesium, 0.9 x 10^{21} m^{-3} and 2.2 x 10^{22} m^{-3} for tantalum, 0.8 x 10^{21} m^{-3} and 2.1 x 10^{22} m^{-3} for titanium. In case of aluminum and magnesium, the plasma electron temperature was about 4000 K when the calculation was made according to Mg I

spectral lines but when O II lines were employed for temperature calculation, a high plasma electron temperature of about 33.000 K was found (Jovović et al., 2012).

2.3.3.3 The Lifetime of Discharge Events

Matykina et al. (2007) showed that the duration of discharges on a titanium substrate varies from 40 ms to 800 ms. The lifetimes of discharges were determined at selected voltages by analysis of successive frames over a period of about 1 s. Arrabal et al. (2009) used a high speed camera (capable of recording up to 20.000 fps) to reveal the lifetime of discharges during PEO processing of magnesium alloys. He found that the duration of discharges is in the range of 0.05-4 ms. Besides fast video imaging several other researchers also used electrical signals to reveal the lifetime of discharge events. Electrical monitoring and fast video imaging (up to 100.000 fps) studies showed that the lifetime of weak smaller discharges is less than 10 μs, which are predominant in the initial period of processing, whereas, the intense larger discharges, developed in the later stages of PEO processing, have a lifetime of about several hundred ms, even though these are terminated by the cathodic cycles of 5 ms (Habazaki, Tsunekawa, Tsuji & Nakayama, 2012). Dunleavy et al. (2009) revealed that individual discharge events have a short lifetime in the range from 10 μs to 100 μs, but these pulses occur in cascades (extended discharge sequences) with short intervals (tens to hundreds μs) between each pulse. Thus, a cascade, which has a duration of a few ms up to a few tens of ms in direct current (DC) PEO processing, includes large numbers of individual discharges (tens or hundreds). Further study by the same author on electrical monitoring of plasma discharges showed that the lifetime of discharges during AC PEO processing is in the range from 20 μs to 400 μs (Dunleavy et al., 2013). As the author proposed in his earlier paper (Dunleavy et al., 2009), individual discharges tend to occur in sequences (cascades) at localized regions during parts of the anodic half cycle where the applied potential is sufficiently high (>300 V).

CHAPTER THREE
CORROSION PROPERTIES OF TITANIUM ALLOYS

3.1 Corrosion of Titanium and Its Alloys

Although titanium and its alloys are used essentially for their unique mechanical properties, among which the most remarkable is their high strength-to-weight ratio, another notable property of titanium and its alloys is their excellent corrosion resistance to many highly corrosive environments. Except for the fluoride containing medium, commercially pure (CP) titanium has great corrosion resistance in most corrosive environments, including chemical process industry. Titanium also exhibits excellent resistance to atmospheric corrosion in both marine and industrial environments. The excellent corrosion resistance of titanium and its alloys arises from the formation of very stable continuous, highly adherent, and protective oxide films (Schutz, 2005). The surface oxide films form immediately when titanium exposed to air and/or moisture, since titanium metal is very reactive and has a great affinity with oxygen. When the oxide film is damaged either by mechanical impact or other environmental effect, the film repairs itself if oxygen or water present in the environment. A general comparison of corrosion resistance of titanium and its alloys with some other metals is given in Figure 3.1.

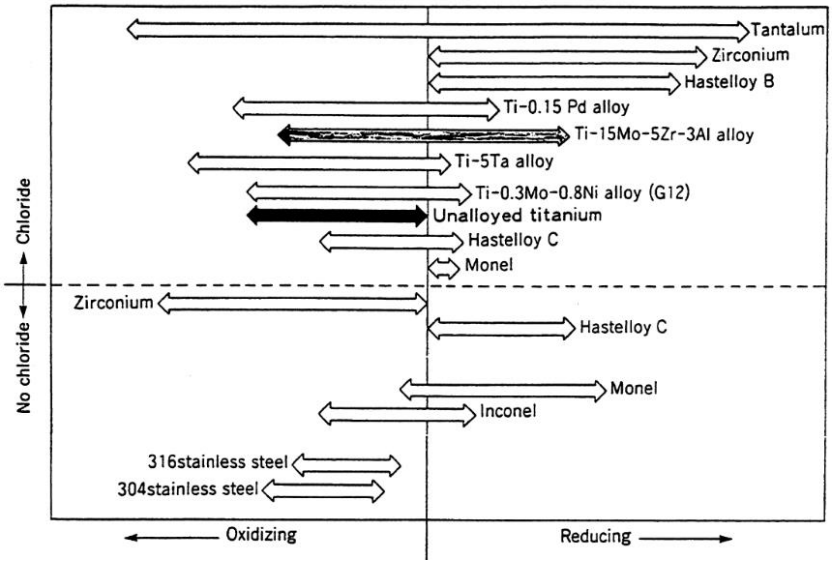


Figure 3.1 The comparison of the corrosion ranges of metals (Donachie, 2000)

3.2 Types of Corrosion

Titanium alloys, as such in other metals, are susceptible to corrosion in certain environments. General corrosion, crevice corrosion, anodic pitting, hydrogen embrittlement and stress-corrosion cracking are the principal types of corrosion seen on titanium alloys.

3.2.1 General Corrosion

General corrosion is a type of corrosion that occurs at almost the same rate on the surface of the entire metal which is exposed to the corrosive environment. This type of corrosion is most frequently observed in reducing acid environments, such as sulfuric, hydrochloric, hydrofluoric and phosphoric acids, especially as acid concentration and temperature increase (Caprani & Frayret, 1979; Schutz & Grauman, 1986; Singh & Hosseini, 1993). In hot reducing acid containing environments, the protective nature of the oxide film on titanium breaks down, resulting in the increased corrosion rate. For example, titanium dissolves very rapidly in hydrofluoric acid over the full range of concentrations and temperatures, mainly because this acid causes the oxide film to break down and forms highly stable, soluble complexes with titanium. In many the industrial applications of titanium including reducing acids, the stability and integrity of the protective titanium oxide film can be improved by adding inhibitors (oxidizing species) to these corrosive environments. Anodic protection is also an effective method for passivating and protecting titanium alloys in reducing acids.

3.2.2 Crevice Corrosion

Crevice corrosion is a localized form of corrosion generally associated with a stagnant solution in tight crevices. The crevices can stem from structural features such as gasket-to-metal flange and other seal joints, or it may be the result of buildup of surface scales or deposits. Dissolved oxygen or other oxidizing species present in the bulk solution are depleted within the crevice, because of the small and restricted

volume of solution. These species are consumed faster than they can be replenished by diffusion from the bulk solution. Crevice pH levels as low as 1 can develop causing severe and rapid localized active corrosion within crevice. Consequently, the metal potential in the crevice becomes more negative compared to that exposed to the bulk solution. This sets up an electrolytic cell with the metal in the crevice acting as the anode and the metal outside the crevice acting as the cathode. Metal dissolves at the anode under the influence of the resulting current.

Titanium alloys can be subject to localized attack in tight crevices exposed to hot chloride, bromide, iodide, and sulfate-containing solutions (Griess, 1968). It has been demonstrated that alloying titanium with palladium (Takamura, 1967), ruthenium (Schutz, 1996), molybdenum and nickel (Satoh, Shimogori & Kamikubo, 1987) can increase its resistance to crevice attack. Surface pickling, which removes the smeared iron metal from titanium surface is also an effective method for increasing crevice corrosion resistance of unalloyed titanium. It is believed that unalloyed titanium can suffer attack similar to pitting when an iron particle smeared on titanium metal corrodes in saline environments. The electrode potential difference between titanium and iron gives rise to establishment of an electrochemical cell in which the iron would be consumed as the anode. As the iron is consumed, a pit has started to grow in which local acid conditions develop preventing the formation of a passive film.

3.2.3 Anodic Pitting

Pitting corrosion is a localized form of corrosion by which cavities are produced in the metal. Pitting is initiated by the development of a local electrochemical cell which includes an anodic site (usually imperfections in the oxide film) surrounded by a cathode site. Since it is more difficult to detect, predict and design against, pitting corrosion is considered to be more dangerous than uniform corrosion damage.

Pitting takes place when the electrode potential of the metal exceeds the breakdown potential of the oxide film on the metal surface. When the corrosion potential of the metal is equal to or higher than the anodic breakdown potential under

a given set of conditions, spontaneous pitting can be expected. Fortunately, titanium exhibits high anodic breakdown potentials in most environments thus this type of corrosion is generally not of concern for titanium alloys. For example, pitting potentials exceed +80 V (vs. the saturated calomel electrode) in sulfate and phosphate solutions and are typically in the range from +5 to +10 V for chlorides. However, anodic breakdown potential values of titanium alloys are significantly lower in bromide solutions, and these values decrease with increasing temperature. Thus, pitting of titanium alloys may be possible in pure bromide solutions at higher temperature if highly oxidizing conditions prevail (Welsch, Boyer & Collings, 1993).

3.2.4 Hydrogen Uptake

Titanium and its alloys are generally used in hydrogen containing environments and under conditions in which galvanic couples or cathodic charging causes hydrogen evolution on the surface of titanium. The protective oxide film on titanium is an effective barrier to hydrogen diffusion. If the film is damaged by abrasion, it then may be susceptible to hydrogen absorption in absence of moisture or oxygen traces. It has been demonstrated that anhydrous hydrogen gas atmospheres may lead to hydrogen absorption in titanium with increasing hydrogen pressure and temperature (Williams, Koehl & Bartlett, 1969). The cathodic charging of titanium gives rise to hydrogen absorption that increases with decreasing solution pH (as low as 0.3) and increasing temperature (up to 100 °C) (Phillips, Poole & Shreir, 1974). The surface preparation of titanium is also an effective factor on determining the severity of hydrogen absorption during cathodic charging. Abraded specimens exhibited greatest hydrogen absorption whereas pickled and vacuum annealed specimens has least.

In titanium alloys, excessive hydrogen uptake can induce the precipitation of titanium hydride in the α phase. Small amounts of hydride precipitates are not detrimental from an engineering standpoint in most cases, but cause severe reduction in alloy ductility and toughness when present in greater amounts (Briant, Wang & Chollocoop, 2002).

3.2.5 Stress Corrosion Cracking

Stress corrosion cracking (SCC) is cracking due to a process involving conjoint corrosion and straining of a metal due to residual or applied stresses. Titanium alloys are subject to this form of corrosion in a few specific environments such as absolute methanol, red fuming nitric acid, nitrogen tetroxide, several liquid metals such as cadmium and mercury, and aqueous halide solutions (Brown, 1972).

Alloy composition and interstitial solute content significantly influence susceptibility to SCC. It has been found that increased content of the interstitial oxygen atoms from 0.25 up to 0.4 wt.% increase the susceptibility of titanium to seawater SCC (Simbi & Scully, 1995). Interstitial nitrogen and carbon have a similar effect on the susceptibility of titanium by their effect upon the mechanical properties. Addition of iron (~ 0.2 wt.%) improve the seawater SCC of commercially pure titanium possibly by reducing the grain size of α phase (Simbi & Scully, 1995). Addition of aluminum above a critical value (> 5 wt.%) can lead to the formation of Ti_3Al precipitate during low-temperature aging, which both lowers the threshold stress intensity factor for SCC (K_{ISCC}) and increases the crack growth rate (Brown, 1972). The presence of tin further decreases the SCC resistance. Whereas SCC in sea water is not a concern for the lower strength commercially pure grades, susceptibility can be lowered substantially in higher strength aluminum-containing alloys by lowering the oxygen content, as, for example, in the case of Ti 6-4 ELI (Grade 23).

Stress corrosion cracking susceptibility is influenced by the concentration of solution species, pH, temperature, and viscosity. It has been shown that the halide anions CI^-, Br^- and I^- either accelerate cracking in titanium alloys susceptible to SCC in distilled water or induce susceptibility in alloys immune to SCC in distilled water. Increasing the concentration of these halide ions usually increases the velocity of cracking. Other neutral or inhibiting ions such as NO^{3-}, SO_4^{2-}, OH^-, CrO_4^{2-}, and $PO4^{3-}$ produce neither of the above effects related to halide ions and may in some cases inhibit SCC. Reducing the pH results in a greater susceptibility to SCC. Crack

velocity was found to increase with increasing temperature and decreasing viscosity (Brown, 1972).

3.3 Corrosion Behavior of PEO Coatings

Titanium and its alloys have excellent resistance to corrosion in many environments owing to the compact and protective oxide film formed on their surface immediately when exposed to air or moisture. In many cases, this oxide film provides sufficient corrosion resistance, but in reducing environments, the damage of oxide film can increase the corrosion rate. Additionally, the oxygen depleted zones formed on metal parts made of titanium alloys may lead to crevice corrosion, where the thin oxide film is deteriorated since it cannot heal itself in the absence of oxygen. PEO technique is generally utilized to increase the thickness of natural oxide film and to change the amorphous oxide into crystalline oxide phases, thereby improving the corrosion and wear properties. Some of the studies on corrosion behavior of PEO-coated titanium alloys are summarized in this section.

Yerokhin, Nie, Leyland & Matthews (2000) coated Ti6Al4V alloy using a series of electrolyte compositions including sulfate, phosphate, silicate, aluminate and some of their combinations. They studied the corrosion behavior of PEO coatings using potentiodynamic polarization method in 3.5% NaCl, 0.5 N H_2SO_4 solutions and a physiological solution (8.74 g/l NaCl, 0.35 g/l $NaHCO_3$ and 0.28 g/l $Na_3PO_4 \cdot 12H_2O$), which are degassed with Ar for 1 h before immersion of test electrodes. The anodic polarization was performed with a constant rate of 40 mV/min until a potential of +2 V versus saturated calomel electrode (SCE). They have been reported that the coatings produced in silicate containing electrolytes showed the best corrosion resistance in sulfuric acid solution, since the silica and titanium oxide present in their structure remain stable over a wide range of potentials in low pH value. The coatings produced in aluminate containing electrolytes showed less protection against corrosion in sulfuric acid solution, where the aluminum oxide is possibly dissolved releasing aluminum cations into the solution. On the other hand, the coatings produced in aluminate and phosphate containing electrolytes exhibited

the best corrosion protection in sodium chloride and physiological solutions. This was attributed to the dense film structure of coatings, which suppresses the penetration of chloride ions into the substrate.

Gnedenkov, Sinebryukhov & Sergienko (2006) produced thermal oxide and PEO coatings on CP-Ti (grade 2) alloy to compare their electrochemical corrosion properties. PEO coatings were produced using phosphate and hypophosphite-aluminate containing electrolytes. The thermal oxide coating was formed by oxidation of bare substrates at a temperature of 750 °C for 3 h. EIS tests were conducted in 1 M HCl solution at room temperature to evaluate the electrochemical corrosion behavior. Impedance spectra was acquired at frequencies extending from 1 MHz to 10 mHz with an AC voltage amplitude of ± 10 mV. The equivalent circuit model used for fitting the impedance spectra of thermal oxide and PEO coating produced in phosphate electrolyte consists of two time constants revealing a double-layered structure with an outer porous and inner compact layer, whereas the coating produced using hypophosphite-aluminate electrolyte exhibited a third time constant which is attributed to a heterogeneous composition of the nonporous sublayer of the coating, consisting of aluminum oxide modified with electrolyte components. By comparing the absolute impedance values in Bode plots, it was concluded that thermal oxide and PEO coating formed in phosphate electrolyte showed nearly identical corrosion resistances.

Shokouhfar, Dehghanian & Baradaran (2011) investigated the corrosion behavior of PEO-coated pure titanium using potentiodynamic polarization and EIS test methods in Ringer's solution (8.6 g/l NaCl, 0.3 g/l KCl and 0.33 g/l $CaCl_2 \cdot 2H_2O$). They were coated pure titanium in aluminate and carbonate containing electrolytes. It has been demonstrated that the PEO coatings decreased the corrosion rate of bare titanium, and the lowest corrosion current density was obtained with coating produced in aluminate containing electrolyte. EIS plots contained two time constants which correspond to outer porous layer and inner compact layer. The barrier property of intact inner layer was found to be responsible for the increased corrosion resistance of coatings. In another study by Shokouhfar, Dehghanian, Montazeri &

Baradaran (2012), pure titanium was coated using silicate, phosphate and borate electrolytes at constant applied voltage of 350 V. The coating produced in phosphate containing electrolyte showed the best corrosion protection, which was attributed to decreased pore size and increased amount of rutile besides anatase.

Cheng et al. (2013) studied the corrosion properties of PEO coatings produced on Ti6Al4V alloy using silicate-hexametaphosphate containing electrolyte with a pulsed bipolar electrical regime for different processing times changing from 10 s to 60 min. The corrosion tests were conducted by potentiodynamic polarization method in a naturally-aerated 3.5 wt.% NaCl solution in which the test electrodes were immersed for 30 min and 24 h before starting the anodic polarization. It has been observed that the coatings obtained at longer processing times showed higher passive current density, indicating that enhanced corrosion resistance is provided by a thinner coting with less imperfections in the microstructure. The increased immersion times in corrosive medium resulted in increased passive current density at high anodic potentials, indicative of less protective coating.

Venkateswarlu et al. (2012) used a sodium phosphate based main electrolyte to produce PEO coatings on CP-Ti and added other chemicals such as sodium carbonate (Na_2CO_3), sodium nitrite ($NaNO_2$) and urea ($CO(NH_2)_2$) into this main electrolyte to investigate their effects on the structural and corrosion properties of PEO coatings. The corrosion properties of bare substrate and PEO coatings were evaluated using both potentiodynamic polarization and EIS test methods in Kokubo's simulated body fluid (SBF) conditions at a temperature of 37 °C. Additionally, salt spray test was performed in 5 wt.% NaCl solution at 35 °C for 168 h. The open circuit potential (OCP) measurements indicated that the coatings have higher OCP values than bare substrate, suggesting less tendency to take place in electrochemical corrosion reactions. The lowest corrosion rate was obtained with sodium carbonate additive, and this improved corrosion resistance was attributed to increased amount of rutile and decreased structural imperfections such as porosity. To compare the corrosion performance of coatings, the barrier layer resistance obtained by fitting the impedance spectra was utilized since the outer layer is porous and is highly

permeable to corrosive ions. It has been shown that sodium carbonate additive provided higher corrosion resistance when compared to other additives.

Zhang, Jiang, Yao & Wu (2010) studied the effect of calcium hypophosphite addition into the aluminate electrolyte on the structural properties and electrochemical corrosion behavior of PEO coatings produced on Ti6Al4V. The corrosion behavior was evaluated using potentiodynamic polarization and EIS test methods in naturally aerated 3.5 wt.% NaCl solution. In EIS plots, two time constants were observed in the high frequency range representing the outer porous layer and in the low frequency region corresponding to inner compact layer. Addition of small amount of calcium hypophosphite increased the resistance of inner compact layer but further increasing the additive concentration reduced its resistance. The lowest corrosion current density in potentiodynamic polarization test was also achieved by addition of small amount of calcium hypophosphite. As in EIS analysis results, addition of large amount of additive into the aluminate electrolyte increased the corrosion current density, indicative of reduced corrosion resistance.

Di, Guo, Lv, Yu & Li (2015) produced PEO coatings on commercially pure titanium (99.005 wt.% Ti) using silicate-based electrolyte containing CeO_2 nanoparticles at various quantities. The corrosion properties of coatings and bare substrate were examined using potentiodynamic polarization test method in 3.5 wt.% NaCl solution. It has been demonstrated that CeO_2 nanoparticles below a critical concentration were incorporated into the coating structure through discharge channels during PEO process, but with increasing concentration of nanoparticles in the electrolyte, these particles deposited on the coating surface covering the whole surface area instead of forming a composite structure with oxide film. The electrochemical corrosion test results showed that the incorporated nanoparticles decreased the corrosion current and improved the corrosion resistance of coatings.

Quintero et al. (2015) studied the effect of different electrolyte compositions on the growth and corrosion properties of PEO coatings on Ti6Al4V alloy. In PEO treatment, the electrolytes contained sodium hypophosphite as the main component

and other chemicals including sodium silicate and aluminum sulfate were added into the hypophosphite containing reference electrolyte. PEO coating was applied by either constant current mode or constant voltage mode at various treatment times. The electrochemical properties of coatings were determined using EIS test method in 0.018 M NaCl solution, with an AC voltage amplitude of ±10 mV over a frequency range from 100 kHz to 5 mHz. EIS analysis revealed a double-layered structure including porous outer layer and dense inner layer. It has been demonstrated that the coatings produced using constant voltage mode showed higher corrosion resistance than those produced using constant current mode in the same electrolyte. Silicate additive provided to obtain the highest impedance values, whereas the addition of sulfate into the main electrolyte resulted in decreased impedance values, indicating poorer corrosion resistance. The improved corrosion resistance was related to the formation of a denser and thicker inner barrier layer.

Babaei, Dehghanian & Vanaki (2015) produced PEO coatings on CP-Ti (grade 2) using a pulsed DC power supply at a constant voltage of 500 V with two different pulse frequencies of 100 Hz and 1 kHz. The reference electrolyte contained sodium dihydrogen phosphate and the effect of sodium zirconate and sodium silicate additives on the structural and corrosion properties of coatings was investigated. The corrosion behavior of coatings was evaluated using EIS test method in 3.5 wt.% NaCl solution for different immersion times of 0.5, 2, 20 and 48 h. The impedance spectra were obtained over a frequency range from 100 kHz to 100 mHz with an AC voltage amplitude of ±10 mV. The impedance values of both compact inner layer and porous outer layer are decreased with increasing the immersion time for all coatings, and this was attributed to the penetration of the corrosive ions into the coating structure through micropores. It has been observed that the increased amount of sodium zirconate improved the corrosion resistance of coatings produced at a frequency of 1 kHz, whereas at a frequency of 100 Hz, a moderate amount of zirconate additive was sufficient to increase the corrosion resistance but further addition of zirconate degraded the corrosion properties. It was suggested that the decreased frequency resulted in formation of long-lived microdischarges, which deteriorate the inner compact layer and reduce the corrosion resistance.

Sarbishei, Faghihi Sani & Mohammadi (2016) investigated the effect of alumina nanoparticles concentration on the structural and corrosion properties of PEO coatings on CP-Ti alloy. They used a silicate-based electrolyte containing different concentrations of alpha alumina nanoparticles (80 nm) up to 10 g/l. Corrosion properties of coatings were studied using EIS and potentiodynamic polarization test methods in 3.5 wt.% NaCl solution. It has been observed that the surface porosity and pore size were reduced with increasing concentration of alpha alumina nanoparticles in the electrolyte, due to the plugging of micropores with nanoparticles during PEO processing. As a consequence of incorporation of nanoparticles, the alpha alumina content in coating structure increased, while the rutile content decreased. In polarization tests, the lowest corrosion rate and highest polarization resistance were obtained with highest concentration of nanoparticle, indicating the suppression of the corrosive ion penetration towards the substrate owing to reduced surface porosity. In EIS analysis results, the resistance of compact inner layer increased with increasing nanoparticle concentration.

CHAPTER FOUR
TRIBOLOGICAL PROPERTIES OF TITANIUM ALLOYS

4.1 Adhesive Wear of Titanium Alloys

When two solid surfaces come into contact under load, adhesion or bonding occurs at the asperity contacts at the interface, and these contacts are sheared by sliding, which may lead to the detachment of fragments from one surface to adhere to the other. The tendency of contacting surfaces to adhere arises from the attractive forces that exist between the surface atoms of the two materials (Rabinowicz, 1995). As the sliding continues, the fragments may break off the surface on which they are adhered and be adhered back to the original surface, or else form loose wear particles.

Titanium has strong tendency to adhesion when it slides against itself or other materials including metals and ceramics. It has been reported that the friction coefficient of titanium (99.99%wt) sliding against itself in vacuum (10^{-9} mm Hg) ranges from 0.6 to 0.8 depending on the sliding velocity (Buckley & Johnson, 1966). When titanium slides against polycrystalline aluminum oxide in vacuum (10^{-9} mm Hg), surface of the aluminum oxide indicated transfer of metal to the its surface and the friction coefficient value increased to about 1.3 (Buckley, 1967).

High friction leading to stick-slip behavior and poor adhesive wear behavior against both itself and steel have been major industrial problems both during processing and application of these alloys. A particular feature of this problem is the metal transfer which occurs to produce smeared layers on the counterface materials.

4.1.1 Electron Structure

In 1949, Pauling developed a resonating valence bond theory of metals and intermetallic compounds, and quantified the percentage of d-valence bond character for transition metals. Since the d-valence bonds are partially filled in transition

metals, they are in charge of such physical and chemical properties as cohesive energy, shear modulus and chemical reactivity of the surfaces.

Buckley used Paulings' theory to explain the interfacial interaction of transition metals placed into contact with other dissimilar metals in the atomically clean state (Buckley, 1977). He concluded that the intermetallic bonds that are formed between two metal surfaces depend heavily on the character of bonding in each of the metals. The data in Figure 4.1 shows the coefficients of friction as a function of percent d-valence bond character for transition metals in contact with gold. These data show a decrease in coefficient of friction with an increase in d-valence bond character, as predicted from Paulings' theory. The metals with greater percentage of d-valence bond character possess less chemical surface activity and lower coefficient of friction. Similar relation between the percent d-valence bond character and coefficient of friction values have been observed when transition metals are in contact with nonmetallic materials such as diamond, manganese-zinc ferrite, boron nitride and silicon carbide (Miyoshi & Buckley, 1982). Since titanium is chemically very active, it possessed strong adhesive forces when in contact with dissimilar metals and nonmetallic materials. When the adhesive bond forces between titanium and counter material were stronger than the cohesive bond forces in either titanium or other metal, material transfer from the weaker metal surface to the other one occurred during sliding tests. Thus, the low percentage d-valence bond character and high chemical activity of titanium can be used to explain its poor tribological properties when slid against metals or nonmetallic materials.

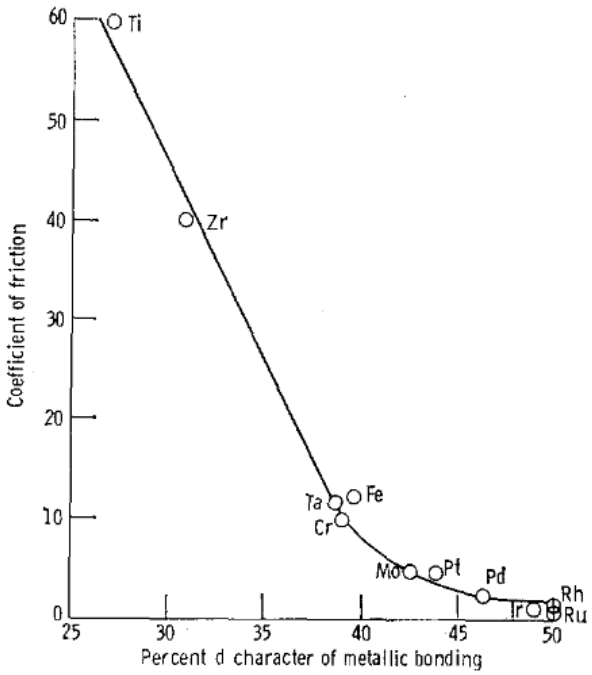


Figure 4.1 Variation of friction coefficient of some metals rubbing against gold with the percent d-valence bond character. Sliding velocity: 0.7 mm/min, load: 1 g, temperature: 23°C and pressure:10^{-8} Pa (Buckley, 1977)

4.1.2 Crystal Structure

The true contact area of two mating surfaces is expected to increase with the improved ability of materials to deform plastically. Since the plastic deformation mechanism is characterized by the number of operable slip systems present in the various crystal structures, it might therefore be expected that the crystal structure would exhibit an influence on adhesion and friction. There are twelve possible slip systems with face-centered-cubic (FCC) metals. Body-centered-cubic (BCC) metals have twelve main operable slip systems and thirty-six secondary slip systems which require higher shear stresses to produce slip. With hexagonal close-packed metals (HCP), however, there are only three operable basal slip systems at room temperature. Thus, there is a greater tendency for the transition to multiple slip in case of the BCC and FCC metals rather than the HCP metals. The limited slip behavior in the HCP metals, therefore, seems to indicate that the HCP metals might well exhibit lower adhesion behavior than either BCC or FCC metals (Buckley, 1968). The above predictions based on the crystal structure are confirmed by the

experimental results. It has been concluded that the HCP metals have lower adhesion than the cubic metals (Sikorski, 1964) and their friction and wear are also less (Buckley, 1967; Buckley & Johnson, 1966).

Some HCP metals, such as magnesium, cobalt, zinc and cadmium, having c/a ratios of either near ideal (1.633) or higher than ideal, slip primarily on the basal plane (0001), which is the only slip plane operates at low temperatures. For other HCP metals, such as titanium and zirconium, the distance between basal planes is reduced giving a c/a ratio of less than ideal. Since the compression along the c-axis results in stronger atomic bonding forces between basal planes, the prismatic and pyramidal planes become more favorable for slip than the basal plane. It has been demonstrated that with oriented titanium single crystals sliding on polycrystalline titanium a lower friction coefficient was obtained when the single crystals were oriented with the prismatic plane $(10\bar{1}0)$ parallel to the direction of sliding than when the crystals were oriented with the basal plane (0001) in the same direction (Buckley, 1965). In case of titanium exhibiting non-basal slip, a greater number of slip systems are operative during sliding wear, which can result in an increase in true contact area and also work hardening. This gives rise to an increased shear resistance in sliding contacts because there is multiple, intersecting slip plane dislocations, hence higher friction might be expected for titanium. As seen in Figure 4.2, the friction coefficient for titanium is higher than that obtained with the hexagonal metal cobalt. Cobalt has a c/a ratio close to ideal hexagonal packing, which gives rise to slip primarily on the basal plane (0001). In contrast, however, hexagonal titanium primarily exhibits slip on the prismatic planes. Since the critical resolved shear stress on prismatic plane for titanium is greater than that on the basal plane for cobalt, higher friction coefficients are observed for titanium than for cobalt.

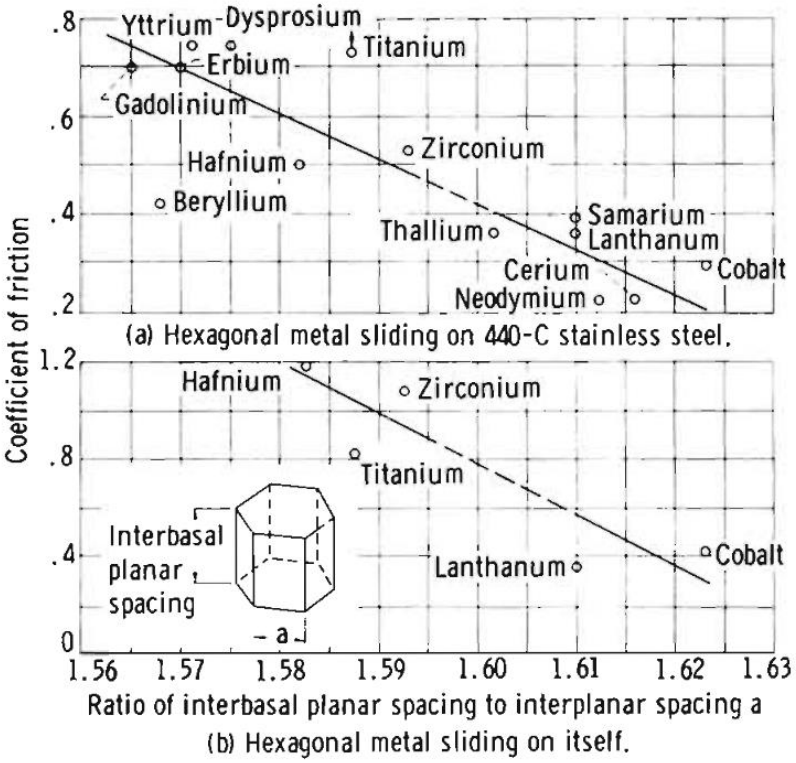


Figure 4.2 Variation of friction coefficient of some metals with c/a lattice ratio. Vacuum: 10^{-9} mm of Hg, sliding velocity: 400 fpm, load: 1 kg, no external sample heating (Buckley & Johnson, 1966)

4.1.3 Thermal Conductivity

When the solid surfaces are in contact and slide together, almost all the energy dissipated in friction appears in the form of heat at the interface. Since the contact between solid surfaces is made over a few isolated junctions, substantial amounts of thermal energy is accumulated at these junctions. It is known that the temperature rise at the junctions during sliding motion is inversely proportional to the thermal conductivities of the two contacting materials (Rabinowicz, 1995). As the flash temperature increased at the interface due to the low thermal conductivity of titanium, which inhibits the heat dissipation from the interface to the bulk substrate, thermal softening at the junctions occurs as soon as the yield point of the titanium starts decreasing significantly. Thus, the high plastic strain rate at the junctions causes junction growth yielding the severe adhesive wear of titanium.

4.1.4 Lubrication

Lubrication of solid surfaces is mostly used to decrease the friction force, the amount of wear or the degree of surface adhesion in many engineering applications. But in case of titanium, the commercial lubricants (mineral oils and greases) do not appear to be effective. The surface film may be used to explain the poor adhesion of ordinary lubricants to titanium. The chemisorbed layer of oxygen and nitrogen (oxide film) on titanium surface is resistant to most chemicals, corroding appreciably only in strong acids or hot alkalis. Thus, in order to form a chemically bound lubricating layer, the lubricant must either react directly with the oxide, or remove the oxide layer to react with the underlying metal. Apparently, lubricants are unable to combine with this layer or to penetrate the layer to form a bond with bare titanium (Burns, 1967; Kostman, 1968). It has been concluded that, of all the lubricants evaluated, only the halogenated hydrocarbons produced any beneficial effect, reducing the coefficient of friction to about 0.2-0.3 from the unlubricated value of 0.49 (Miller & Holladay, 1958). These halogenated compounds, especially those containing fluorine, penetrate the oxide layer and chemically attack the titanium surface. The bond formed is sufficiently strong to hold the lubricant on the surface, but, not all halogenated compounds are equally effective. Straight-chained hydrocarbons with halogen atoms distributed along the molecule are more effective than cyclic halogenated molecules. Roberts & Owens (1963b) reported that the friction coefficient of titanium sliding against itself can be reduced to about 0.25 to 0.38 using a lubricant, which consists of a charge-transfer complex of iodine and an aromatic hydrocarbon. The lubrication mechanism proposed by Roberts & Owens (1963a) was the formation of titanium diiodide (TiI_2), a low shear strength laminar solid at the wearing interface but further results of sliding-contact studies with aluminum, gold, and glass show that it is not essential to form a diiodide layer-lattice structure in order to reduce friction or wear with iodine in oil (Furey, 1966).

These liquid lubricants providing boundary lubrication may be useful for machining operations but are not applicable to high-load tribological applications, where severe adhesive wear (seizure) may occur. Another shortcoming of the

application of lubricants is the low thermal conductivity of titanium, which causes higher temperatures at contacting surfaces, resulting in some desorption of the boundary lubricant (Hutchings, 1992).

4.2 Abrasive Wear of Titanium Alloys

Abrasive wear takes place when asperities of a hard surface or hard particles slide against a softer surface and cause material removal by plastic deformation or fracture (Bhushan, 2013). Two general conditions for abrasive wear are shown in Figure 4.3. In the first situation, the material removal is caused by two-body abrasion which involves a hard surface rubbing on a soft surface. This type of abrasive wear is observed in mechanical operations, such as grinding, cutting and machining. In the second situation, the hard surface causing abrasive wear is a third body, usually a small abrasive particle, trapped between the two sliding surfaces. These particles are sufficiently hard to abrade either one or both of the mating surfaces (third body abrasion). This type of abrasive wear is observed in free-abrasive lapping and polishing.

During abrasion of metals, the material removal from a surface can take place as a result of plastic deformation in various deformation modes such as plowing/ploughing, wedge formation and cutting (Figure 4.4). Plowing leads to a series of grooves parallel to the sliding direction as a consequence of the plastic flow of the softer material. While the harder surface slid against the softer surface, material is transferred from a groove to the sides without the removal of material. However, after several successive passage over the softer surface, material removal can occur by a low-cycle fatigue mechanism. When plowing takes place, ridges are developed on the edges of the grooves. These ridges are flattened by repeated loading and unloading cycles, and ultimately fracture causing material removal.

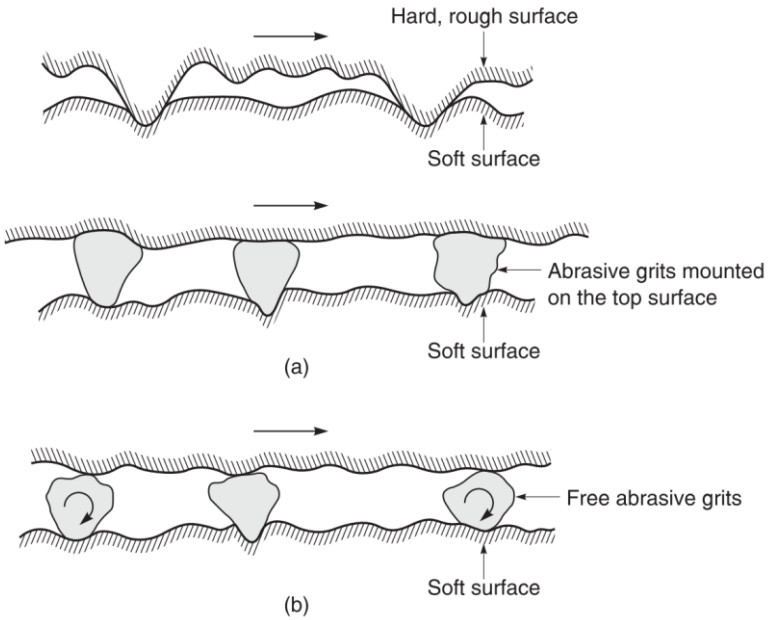


Figure 4.3 Schematics of (a) a soft surface that is rubbed against a harder surface or a surface mounted with abrasive grits, and (b) loose abrasive grits entrapped between two mating surfaces, at least one of them is softer than the abrasive grits (Bhushan, 2013)

When an abrasive tip plows a groove, a wedge is formed in front of it. The wedge formation is commonly observed when the ratio of shear strength of the interface relative to the shear strength of the bulk is high (about 0.5–1) (Bhushan, 2013). In this case, some of the material displaced from the groove comes out as a wedge, apart from the material displaced to the sides. In case of cutting form of abrasive wear, a groove is plowed by an abrasive tip and the material removed from the surface forms discontinuous or ribbon-shaped wear debris particles which resemble that produced in a metal cutting process.

These three deformation modes are controlled by some factors including the properties of the worn material and the operating conditions such as attack angle and friction coefficient. With increasing hardness of the worn material, the transition from predominant plowing to predominant cutting occurs (Hokkirigawa, Kato & Li, 1988). The schematic of an abrasive particle removing material from counter body is given in Figure 4.5 showing the ratio of microcutting to microploughing as a function of the ratio of the attack angle to the critical attack angle. The attack angle is defined as the angle between the leading face of a contacting abrasive particle and

the worn surface. There is a critical angle beyond which the deformation mode is changed from plowing and wedge formation to cutting (Zum Gahr, 1987).

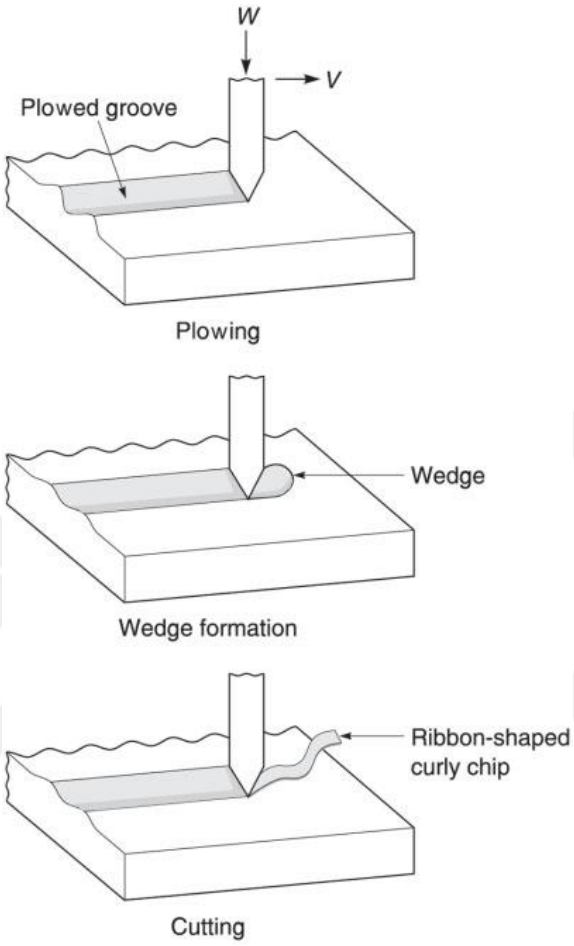


Figure 4.4 Schematic views of abrasive wear processes due to plastic deformation (Bhushan, 2013)

It is commonly recognized that the abrasive wear resistance of materials increases with increasing hardness (Khruschov, 1974). It is known that titanium and its alloys are relatively soft, hence their abrasive wear resistance is poor as compared with steel which is easily hardened by martensitic transformation after quenching.

The abrasive wear behavior of CP-Ti and Ti6Al4V alloys against silicon carbide and alumina sandpapers was evaluated using pin-on-disc apparatus under conditions of controlled atmospheric compositions including oxygen, dry nitrogen and dry argon gases, and air (Mercer & Hutchings, 1988). Both grades of titanium showed a linear wear loss during repeated sliding over the same wear track in air. However,

during abrasion in inert gas atmospheres, two linear sections were observed in the wear loss versus time graph. The wear rate of the Ti6Al4V was higher in the initial period then decreased to lower values during sliding in inert gas atmospheres. Consequently, the mean rate of wear in inert gas atmospheres was lower (by up to 70%) than that obtained in air. The wear rate in pure oxygen atmosphere was also linear as for dry air atmosphere but it was increased by about 30% compared to that obtained in dry air. It has been suggested that the removal of interstitial atoms (especially oxygen) in inert gas atmospheres led to increased surface ductility. Since the protective oxide film was not regenerated on the wear track during abrasion, the metallic debris adhered to the titanium alloy surface and accumulated in extensive, heavily deformed sheets which decrease the wear rate.

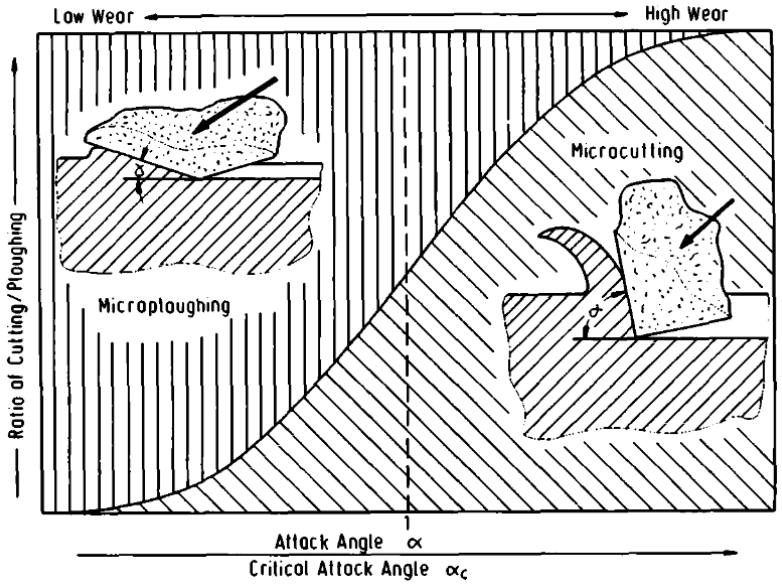


Figure 4.5 The ratio of microcutting to microploughing as a function of the ratio of the attack angle to the critical attack angle (Zum Gahr, 1987)

Budinski (1991) assessed the abrasive wear resistance of CP-Ti (Grade 2) and Ti6Al4V alloys using the ASTM G65 dry sand–rubber wheel abrasion test and he compared their abrasion resistance with some other materials. The test sample is pressed against a rubber-tired wheel and 50-70 mesh silica sand is supplied to the interface between sample and rotating wheel. Test results indicated that both grades of titanium have poor abrasion resistance. The abrasion rates of tested titanium alloys were almost 15 times that of D2 hardened tool steel and were about 7 times that of

1080 carbon steel. In addition, neither grade had an abrasion resistance comparable to soft austenitic stainless steel. Consequently, it has been suggested that titanium should be avoided for applications involving low stress abrasion from hard particles.

4.3 Mechanical Properties and Wear Behavior of PEO Coatings

Previous studies on PEO coating of titanium and its alloys have shown that the electrolytes based on aluminate are usually recognized as generating coatings with high wear resistance (Yerokhin et al., 2000). The incorporation of aluminum species into the coating results in the formation of complex phase structures including aluminum titanium oxide (Al_2TiO_5) and α-alumina (Al_2O_3), which are harder than anatase and rutile phases that are generally existed in the structure of coatings produced in silicate- and phosphate-based electrolytes (Fei, Hai, Chen & Yangjian, 2009; Wang, Jia, Guo, Lei & Jiang, 2005). Yerokhin et al. (2000) employed various electrolytes containing silicate, phosphate, aluminate and sulfate anions and some of their combinations to form oxide coatings on Ti6Al4V alloy using AC plasma electrolytic oxidation. Using aluminate-phosphate electrolytes provided to obtain the most uniform, dense and adherent coatings. The coatings produced in aluminate-phosphate electrolyte were mainly composed of Al_2TiO_5 and rutile phases with minor amounts of pure aluminum oxide and complex aluminophosphates, and had a thickness of 50-60 μm and a Knoop microhardness of 575 kg/mm^2. Harder and thicker coatings formed in an aluminate-phosphate electrolyte provided the maximum wear resistance, however, the friction coefficient was relatively high, in the range 0.6-0.7. Further investigation into the effects of process parameters such as the electrical charge density, aluminate concentration and pH of the electrolyte on the structural and mechanical properties of PEO coatings produced on Ti6Al4V alloy was conducted by Yerokhin, Leyland & Matthews (2002). Increasing both the electrolyte concentration and electrical charge density increased the thickness of coating over 60 μm. The coating structure was composed of Al_2TiO_5 matrix, TiO_2 grain-boundary network and Al_2O_3-enriched inclusions. The hardness values of inclusions and matrix were in the ranges of 1050-1480 and 300-845 HK.

Xue, Wang, Chen & Deng (2002) examined the structure and mechanical properties of coatings produced on Ti6Al4V alloy using an aluminate containing electrolyte (10 g/l). The coating thickness was nearly 50 μm after a process duration of 5 h. The coatings were composed of Al_2TiO_5 and rutile phases. The rutile content increased in the inner layer of coating, whereas the amount of Al_2TiO_5 was higher than that of rutile in the outer layer. The maximum hardness and elastic modulus of coatings measured using nanoindentation test method were 13 GPa and 230 GPa, respectively. Wang, Lei, Jiang & Guo (2004) studied the growth kinetics and mechanical properties of coatings formed in a phosphate-based electrolyte with sodium aluminate addition. A stepped current regime with initial current density of 6 A/dm^2 was used to obtain optimum microstructure of relatively compact coatings. The treatment time was gradually increased to investigate the growth kinetics. The maximum coating thickness was about 40 μm and the coatings were mainly composed of phase modifications of titanium oxide, namely anatase and rutile. The hardness and elastic modulus across the coating thickness were found to remain high (5.5 and 69.1 GPa, respectively) in the compact layer and low (5.1 and 65.6 GPa, respectively) in the looser layer. In another study by Wang, Jiang, Lei & Guo (2006), ceramic coatings were produced on Ti6Al4V alloy by a pulsed bipolar power supply using a silicate-based electrolyte with phosphate and aluminate additions. The maximum hardness and elastic modulus measured across the coating of nearly 45 μm thickness were 8.5 GPa and 87.4 GPa, respectively. The dry sliding wear tests performed against SAE 52100 steel ball and the friction coefficient as low as 0.2-0.3 was obtained below 1 N normal load. Wang, Jiang, Guo & Lei (2006) also studied the effect of solid lubricant top-layer on the tribological properties of PEO coating produced in phosphate-based electrolyte with sodium aluminate addition. The graphite solid lubricant improved the wear resistance of coating by reducing the friction coefficient values from 0.2-0.8 to about 0.12.

Ceschini, Lanzoni, Martini, Prandstraller & Sambogna (2008) compared the tribological performance of PEO coating with that of PVD coatings including TiN, (Ti,Al)N and CrN/NbN. All coatings were produced on Ti6Al4V by industrial facilities. The thicknesses of PVD coatings were between 2.5 μm and 4.1 μm, while

PEO coating showed a significantly higher thickness of 18 ± 4 μm. Wear tests of coatings were conducted using flat-on-cylinder tribometer against an Al_2O_3 (87 vol.%)-TiO_2 (13 vol.%) plasma-sprayed coating on a steel substrate. Tests results showed that PEO coating reduced both friction and wear of substrate alloy, even under high normal loads (up to 35 N), whereas PVD coatings were removed from the surface by ceramic countermaterial during wear causing severe wear damage. The improved wear resistance of PEO coating over PVD coatings was attributed to its high load bearing capacity due to its increased thickness.

Li, Cheng, Xue, Zheng & Cheng (2008) prepared PEO coating on γ-TiAl alloy (at.% 48 Al, at.% 2 Cr and at.% 2 Nb) using an electrolyte of Na_2SiO_3 and KOH. The coating thickness measured using an eddy-current thickness gauge after a processing time of 120 min was about 110 μm. XRD analysis results showed that the inner dense layer and outer loose layer of coating were composed of Al_2TiO_5 and rutile. In addition to these phase constituents, the XRD spectrum of outer loose layer exhibited a broad hump below a diffraction angle of 40° (2θ), suggesting the presence of amorphous SiO_2. The maximum hardness of 13.5 GPa was obtained in the inner dense layer at a distance of 10 μm from the coating/substrate interface. The hardness decreased to lower values towards the coating surface. The wear test of coating was conducted using ball-on-disc configuration under dry sliding condition with an applied load of 5 N. AISI 52100 bearing steel ball was used as the counter material for sliding wear test. Before wear test, two different coatings with thicknesses of 20 μm and 50 μm were obtained by polishing-off the outer loose layer. Both coatings increased the wear resistance of substrate alloy. Besides, the polished coating of 20 μm thickness showed the smallest wear loss due to its increased hardness value.

Habazaki et al. (2012) investigated the effect of electrolyte temperature on the structural properties and wear behavior of PEO coatings. They produced coatings on Ti–15–3 alloy (14.91 wt.% V, 3.01 wt.% Al, 3.15 wt.% Cr, 2.88 wt.% tin, 0.22 wt.% iron and 0.10 wt.% oxygen) using an alkaline electrolyte containing 0.15 M $K_2Al_2O_4$, 0.02 M Na_3PO_4 and 0.015 M NaOH at varying electrolyte temperatures from 278 K to 313 K. Cross section analysis by SEM revealed that the coating produced at 278 K

exhibited the lowest porosity. XRD results showed that all coatings contained Al_2TiO_5 and γ-Al_2O_3, whereas α-Al_2O_3 was detected only in the coating produced at 278 K. Wear behavior of the coatings was evaluated using ball-on-disc tribometer under dry sliding condition. The wear tests were conducted at ambient atmosphere, with a sliding speed of 10.0 mm/s, for a sliding distance of 25 m, under a load of 1-4 N against AISI 52100 steel ball of 6 mm diameter. The coating produced at lowest electrolyte temperature of 278 K showed the highest wear resistance, which was attributed to the reduced porosity and presence of α-Al_2O_3.

Aliasghari, Skeldon & Thompson (2014) formed PEO coatings on CP-Ti (99.6 wt.% purity) using an alkaline electrolyte containing sodium silicate (10.5 g/l specific gravity 1.5), phosphoric acid (2 ml/ l) and potassium hydroxide (2.8 g/l). The coatings used in tribological tests were formed for 900 s at 500 mA/cm^2, with a duty cycle of 50 Hz and a negative/positive voltage amplitude ratio of 1. In order to investigate the effect of solid lubricant on the wear behavior of coatings, PEO treatment was conducted with and without addition of PTFE emulsion (5 g/l) into the electrolyte. The thicknesses of coatings were in the range from 35 μm to 40 μm. XRD analysis results showed that the coatings were composed of rutile, anatase and Ti_2O_5. The wear tests were conducted using a ball-on-disc apparatus, at a normal load of 5 N, against AISI 52100 steel ball at a rotation rate of 20 rpm, and with a track diameter of 5 mm. The wear test results indicated that the addition of PTFE into the electrolyte improved the frictional properties but reduced the wear resistance of PEO coating. Both coatings with and without PTFE emulsion addition showed a limited wear resistance since they were removed from the surface after a short sliding distance. The relatively poor wear resistance of the coatings was attributed to the high porosity and the large amount of amorphous silica, which contributed to the formation of outer loose layer.

Cheng et al. (2013) prepared PEO coating on Ti6Al4V alloy using an alkaline electrolyte containing 8 g/L $Na_2SiO_3 \cdot 9H_2O$ and 15 g/L $(NaPO_3)_6$ for a treatment time of up to 60 min. The maximum thickness of coating after 60 min was in the range from nearly 42 μm to about 46 μm. XRD results indicated that the coatings were

composed of anatase and rutile. Besides, a broad hump between 15 and 30° (2θ) in XRD spectrum was attributed to the presence of amorphous material including silicon and phosphorus species. The wear behavior of PEO coating was evaluated using a ball-on-flat test configuration, utilizing a chromium steel ball as counter material of 9.5 mm diameter and of 62 HRC hardness. The applied load, stroke length and oscillation frequency were 10 N, 7.5 mm and 5 Hz, respectively. In dry sliding wear tests, the wear performance of bare substrate was compared with that of three different coatings which formed for 3 min, 20 min and 60 min, respectively. It has been observed that the coating formed for 60 min remained on the substrate during wear test and protected it from severe wear damage. However, the coatings formed for 3 min and 20 min exhibited a transition point in the friction coefficient curve, where the coating removed from the substrate surface. SEM analysis showed that the coatings formed for 3 min and 20 min were completely removed from the substrate leaving a scratched surface indicating abrasive wear by plowing operation. On the other hand, the coating produced for 60 min possessed a transfer layer on its surface which was formed by the adhesion of steel material. It was suggested that the improved wear resistance of the thicker coating was possibly attributed to its modified properties such as increased adhesion to the substrate, enhanced rutile content, and altered porosity and roughness.

Quintero et al. (2015) studied the effect of different electrolyte compositions on the growth and wear properties of PEO coatings formed on Ti6Al4V alloy. In PEO process, the electrolytes contained sodium hypophosphite as the main component and other chemicals including sodium silicate and aluminum sulfate were added into the hypophosphite containing main electrolyte. PEO coating was applied by either constant current mode or constant voltage mode at various treatment times ranging from 300 s to 1000 s. The wear behavior of PEO coatings against AISI 420 stainless ball of 6 mm diameter as counterbody was evaluated using ball-on-disc test configuration under dry sliding condition at ambient atmosphere. The sliding velocity of 60 rpm, a total sliding distance of 22 m, and a normal load of 4 N were the parameters used in sliding wear test. PEO coatings produced in hypophosphite-silicate electrolytes showed the highest hardness in the range of 400-500 HK, which

was attributed to having a less porous microstructure. Wear test results indicated that all the coatings improved the wear resistance of the substrate alloy, with the coatings produced in potentiostatic mode showing a better tribological performance than those produced in galvanostatic mode. The highest wear rate was observed for coatings produced in hypophosphite-sulfate electrolyte. SEM analysis of wear tracks on coatings indicated the adhesive wear mechanism.

Qin, Xiong & Li (2015) prepared PEO coating on laser surface-textured Ti6Al4V alloy using an alkaline electrolyte comprised of 12 g/L sodium aluminate ($NaAlO_2$), 1.6 g/L trisodium phosphate ($Na_3PO_4 \cdot 12H_2O$) and a small amount of sodium hydroxide (NaOH). Following the PEO processing for 60 min, a solid lubricating MoS_2 film was deposited on the coating surface. The substrate surface was textured to create the microdimple arrays using a pulsed Nd:YAG laser. The microdimples have an approximate diameter of 260 μm, with a spacing of 500 μm between the centers of two dimples. XRD results showed that the coatings were mainly composed of Al_2TiO_5 along with a small amount of γ-Al_2O_3. The tribological performance of PEO coatings was evaluated against AISI 52100 steel ball of 4 mm diameter using ball-on-disc test configuration at the loads of 0.3-5 N and a constant velocity of 0.1 m/s. Wear test results showed that PEO coatings decreased the wear rate of substrate alloy, significantly. Further improvement in the wear resistance was achieved by laser surface-texturing with PEO coating, which was thought to be due the entrapment of the wear debris in microdimples during sliding motion. The solid lubricant top layer prolonged the wear life of PEO coating by reducing the friction coefficient value from about 0.65 to nearly 0.3. Further improvement in the wear resistance of substrate alloys was obtained with laser-surface textured and PEO coated surface with solid lubricant layer. It was suggested that the micropores and microdimples on the coating surface improved the adhesion of solid lubricant layer and provided a continuous lubrication during sliding wear.

Martini, Ceschini, Tarterini, Paillard & Curran (2010) obtained PEO coatings on Ti6Al4V alloy from aluminate-phosphate electrolytes with an initial current density of 20 A/dm^2 using AC regime at 50 Hz. The measured thicknesses of coatings

produced in aluminate-rich and phosphate-rich electrolytes were 41 ± 6 μm and 22 ± 6 μm, respectively. Both coatings contained Al_2TiO_5 and rutile. The coating formed in aluminate-rich electrolyte also involved α-Al_2O_3 and γ-Al_2O_3. The hardness values of coatings produced in aluminate- and phosphate-rich electrolytes were 5.6 ± 0.3 GPa and 4.8 ± 0.3 GPa, respectively. Since the main phase constituent of coatings was Al_2TiO_5, the increased hardness of coating produced in aluminate-rich electrolyte was attributed to the existence of alumina phase, which is harder than Al_2TiO_5, rutile and anatase. As a consequence of dry sliding wear tests, the coating produced in aluminate-rich electrolyte exhibited the highest wear resistance. Wheeler, Collier, Paillard & Curran (2010) investigated the mechanical properties of coatings produced on Ti6Al4V alloy using aluminate-, phosphate- and silicate-based electrolytes with an initial current density of 20 A/dm^2. The thicknesses of coatings after 60 min. of processing time were 60, 13 and 60 for aluminate-, phosphate- and silicate-based electrolytes, respectively. All coatings contained phase modifications of titanium oxide; rutile and anatase. Aluminate- and phosphate-based electrolytes, which include aluminate anions, contained Al_2TiO_5. The increased concentration of aluminate anions in the aluminate based electrolyte led to the formation of α-Al_2O_3 and γ-Al_2O_3, which was thought to be the reason for the increased hardness and elastic modulus of the coating.

Tsunekawa, Aoki & Habazaki (2011) produced ceramic oxide coating on Ti-15V-3Al-3Cr-3Sn alloy using a bipolar square waveform at 100 Hz, with current densities of 20 A/dm^2 and 10 A/dm^2 corresponding to the positive and negative half cycles, respectively. The coating formed in the aluminate-phosphate electrolyte had a thickness of about 10 μm. It was mainly composed of Al_2TiO_5 phase. Rutile and γ-Al_2O_3 were also present in the coating structure as minor oxides. This coating exhibited high wear resistance but poorly adhered to the substrate due to the existence of voids and micropores in the oxide film close to the substrate/coating interface. In order to improve the adhesion of coating to the substrate, two-step PEO treatment was used. The specimen coated in aluminate-phosphate electrolyte was anodized subsequently in an acidic solution containing phosphoric and sulfuric acids. This resulted in formation of a new oxide film with amorphous structure close to the

substrate. The voids and micropores were filled during the second anodizing step in acidic solution and the porosity was reduced resulting in improved adhesion of coating to the substrate.

CHAPTER FIVE
EXPERIMENTAL DETAILS

5.1 PEO Processing Equipment

The equipment used for PEO process is shown in Figure 5.1. PEO processing equipment is similar to that used for conventional anodizing, but differs by the circumstance that pulsed bipolar AC current is utilized and higher potentials exceeding the dielectric breakdown of anodic oxide film are applied. The power supply consists of an array of capacitor banks, which can be charged by a 50 Hz three phase electric power. Their capacitance may be controlled to produce pulses of positive and negative charge to a pair of electrodes at a frequency of 50 Hz. The PEO process is carried out in an electrolyte bath, made of a polymeric material, in which the perforated 316 stainless steel plate is placed as counter electrode. The electrolyte is cooled by pumping through a heat exchanger during the coating treatment. The component to be coated is cleaned and degreased. It is then electrically connected via an insulated titanium jigging arrangement to the copper busbar.

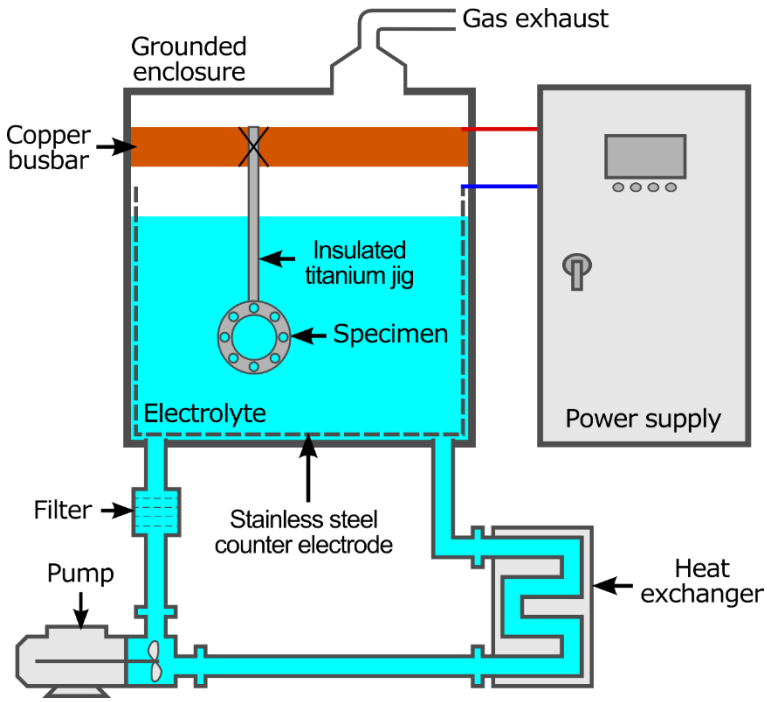


Figure 5.1 Schematic of PEO processing equipment used in experimental studies

5.2 Specimen Preparation

Disc specimens of Ø 25 mm x 10 mm thickness were prepared from Ti6Al4V (Grade-5) (wt.% 6.44 Al, 4.2 V, 0.131 Fe, 0.024 C, 0.014 N, 0.001 H, 0.09 O and bal. Ti) and CP-Ti (Grade-2) (wt.% 0.10 Fe, 0.02 C, 0.008 N, 0.001 H, 0.11 O and bal. Ti) bar stocks. The specimen surface was ground flat on 800 grit SiC papers, subsequently immersed into the solution of 2% vol. HF (38-40%) and 20% vol. HNO_3 (65%), then washed with distilled water. The specimens were coated using Keronite laboratory-scale PEO system as described in Section 5.1. The details of PEO process including electrolyte composition, current density and process duration are listed in Table 5.1.

Table 5.1 Experimental parameters used to produce PEO coatings on titanium alloys

Substrate	**Designation**	**Chemical**	**Concentration (*g/l*)**	**Duration (*min*)**	**Current density (*A/dm²*)**
CP-Ti	CPT-PH	$Na_3PO_4 \cdot 12H_2O$ NaOH	6 2	10	20
Ti6Al4V	T64-PH	$Na_3PO_4 \cdot 12H_2O$ NaOH	6 2	10	20
Ti6Al4V	T64-AL	$NaAlO_2$	12.5	75	20
Ti6Al4V	T64-AL-PH	$NaAlO_2$ $Na_3PO_4 \cdot 12H_2O$	12.5 3.5	75	20
Ti6Al4V	T64-AL-PY	$NaAlO_2$ $Na_4P_2O_7 \cdot 10H_2O$	12.5 4.1	75	20
Ti6Al4V	T64-AL-TA	$NaAlO_2$ $KOCOCH(OH)CH(OH)COONa \cdot 4H_2O$	12.5 2.6	75	20
Ti6Al4V	T64-AL-TU	$NaAlO_2$ $Na_2WO_4 \cdot 2H_2O$	12.5 3	75	20
Ti6Al4V	T64-AL-BO	$NaAlO_2$ $Na_2B_4O_7 \cdot 10H_2O$	12.5 3.5	75	20

$Na_3PO_4 \cdot 12H_2O$: Sodium phosphate tribasic dodecahydrate (CAS number: 10101-89-0; molecular weight: 380.12 g/mol)

NaOH: Sodium hydroxide (CAS number: 1310-73-2; molecular weight: 40 g/mol)

$NaAlO_2$: Sodium aluminate (CAS number: 11138-49-1; cation traces: Al (Al_2O_3): 50-56%, Na (as Na_2O): 40-45%)

$Na_4P_2O_7 \cdot 10H_2O$: Sodium pyrophosphate tetrabasic decahydrate (CAS number: 13472-36-1; molecular weight: 446.06 g/mol)

$KOCOCH(OH)CH(OH)COONa \cdot 4H_2O$: Potassium sodium tartrate tetrahydrate (CAS number: 6381-59-5; molecular weight: 282.22 g/mol)

$Na_2WO_4 \cdot 2H_2O$: Sodium tungstate dihydrate (CAS number: 10213-10-2; molecular weight: 329.85 g/mol)

$Na_2B_4O_7 \cdot 10H_2O$: Sodium tetraborate decahydrate (CAS number: 1303-96-4; molecular weight: 381.37 g/mol)

The most promising electrolytes for producing thick PEO coatings on titanium alloys commonly consist of aluminates. The coatings that are formed in aluminate-based electrolytes have high load bearing capacity and high hardness, which are the required specifications in tribological applications. In this study, it is aimed at producing PEO coatings on Ti6Al4V alloy using aluminate-based electrolytes and investigating the effect of various electrolyte additives on the properties of coatings. The molarities of electrolyte additives in aluminate-based electrolyte were kept the same. In addition to aluminate-based electrolytes, relatively thin coatings were also produced on CP-Ti and Ti6Al4V alloys using phosphate-based electrolyte to compare their electrochemical and tribological properties with thick coatings. Friction modifier (FM) MoS_2 top-coat was applied on some coatings that were formed in phosphate-based electrolyte by dipping in a solution containing solid lubricant MoS_2 particles (average size of 1 μm) and then drying in atmosphere. In order to improve the corrosion resistance of some coatings that were produced on CP-Ti using phosphate-based electrolyte, silane treatment was applied by immersing the coated specimens into a solution of 90 vol.% triethoxymethylsilane (%99, Sigma-aldrich), 6 vol.% distilled water and 4 vol.% methyl alcohol at room temperature for 60 min. Subsequently, the specimens were heat-treated at 120 °C for 1 h.

5.3 Coating Thickness Measurement

The coating thickness was measured non-destructively using Mitutoyo Digiderm 1100 coating thickness gauge.

5.4 Preparation of Cross-Section of Coating

In order to examine the through-thickness microstructure of coatings, PEO coated substrates were sectioned, mounted in resin and finally polished. Sectioning was carried out using SiC-precision cut-off wheel (For Titan, Cut057, from Cloeren Technology GmbH,) mounted on Struers Labotom-5 manual cut-off machine. The coated specimen clamped in the vise and positioned so that the wheel enters the coated side and exits the substrate side, thus substantially avoiding the delamination

of coating from the substrate due to the drag of the cut-off wheel. After sectioning, the specimen was ultrasonically cleaned in ethanol to remove any residue coming from cooling liquid.

After sectioning, cold mounting with epoxy resin (EpoFix, from Struers) was performed at room temperature without the application of vacuum. This method is free from high pressure and temperature which tend to cause damage to the coatings. Epoxy resins have less shrinkage than cold mounting acrylic resins. Curing time is relatively long, but the adhesion to the specimen is excellent. Owing to its low viscosity, epoxy resin can penetrate into the porosities and cracks in the coating meeting the high edge retention requirements during grinding and polishing steps. Fine grinding was then carried out using diamond on a composite fine grinding discs, which retain flatness and assure a good material removal rate. Fine grinding finished with a 2000 grit SiC paper. Polishing was then performed using 3 μm diamond paste in an alcohol-based lubricant. Final polishing was performed with 50 nm colloidal silica suspension. The orientation of the specimen during grinding and polishing steps can have a significant impact on the preparation results. Thus, to eliminate the adhesive failure of coating, the direction of the abrasive was ensured to be through the coating and into the substrate.

5.5 Microstructural Investigation

For microstructural investigation, Nikon Eclipse ME600 optical microscope and JEOL 6060 SEM were used. The optical microscope is equipped with Nikon DS-Fi1 CCD camera that captures the image at a high resolution of 2560 x 1920 pixels. The SEM is equipped with a range of secondary electron (SE) and back-scattered electron (BE) detectors, and an energy dispersive X-ray spectrometer (EDS) attachment.

Since the as-prepared coating has a rough top surface having numerous open pores, the optical microscope is limited only to investigate the polished cross-sections of coatings. The microstructural examination of those allowed to assess the porosity qualitatively and to measure the coating thickness.

To eliminate electron charging due to the low electrical conductivity of coatings, low accelerating voltages were used during SEM analysis, and in addition to this, the specimens were coated with a thin gold-palladium conductive film using Polaron Range SC7620 sputter coater (at 9 mA for three minutes) before being placed into the SEM vacuum chamber. The surface morphology of the coating was investigated in SE mode, whereas the BE mode was used to detect contrast between areas with different elemental compositions, and to reveal the surface topography and sub-surface features and defects. The coating thickness measured using optical microscope or SEM was used to confirm the accuracy of non-destructive thickness measurements.

5.6 Surface Profilometry

Stylus surface profilometry uses an instrument that amplifies and records the vertical motions of a stylus displaced at a constant speed by the surface to be measured. The Ambios Technology XP-2 surface profilometer used in the present study, incorporates an optical deflection height measurement mechanism and magneto static force control system which results in a low force (loads as small as 0.05 mg) and low inertia stylus assembly. The stylus tip has a radius of 2 μm. Measurement of vertical features ranges from under 10 Å to approximately 400 μm with a vertical resolution of 1.5 Å at 10 μm setting and 15 Å at 100 μm setting, which are specified by the producing company.

The stylus arm is loaded against the specimen surface and the stylus is scanned over the surface using a traverse unit at a constant speed. As the sample moves, the stationary stylus rides over the specimen surface detecting surface deviations by the transducer. It produces a signal corresponding to the vertical stylus movement. This signal is then amplified, conditioned, and digitized. Then the surface profile data are used to measure the roughness of specimen according to ISO 4287:1997 standard, which specifies the roughness sampling lengths for the measurement of roughness parameters of non-periodic profiles.

In addition to surface roughness measurement, the stylus surface profilometry is used to determine the exact final shape of the wear surfaces and thereby to calculate the volume of material lost due to wear. A cross-section of the wear track is the area of the material removed from the original flat surface as viewed on a plane normal to the original surface and to the direction of sliding motion. On the wear profile made across the wear track, a straight line is drawn between the unworn areas on both sides of the wear track and the cross-sectional area of the wear groove, below that reference line, is used to compute the wear volume. In the present study, at least five wear profiles of the track were obtained at locations equally spaced along the track length to compute the average track cross-sectional area. Then, the average cross-sectional area was multiplied by the average track length to obtain the specimen volume loss.

5.7 X-Ray Diffraction

The PEO coating on titanium includes usually crystalline rutile and anatase phases with less amount of amorphous titanium oxide depending on the processing variables (i.e. voltage, current and electrolyte constituents), which directly affect the duration, size and temperature of plasma discharges. The chemical compounds in the electrolyte may also react with titanium to form complex oxide structures in the coating. Since the crystalline phase structure have considerable influence on the electrochemical and mechanical properties of the coating, the crystalline phase constituents and their relative amount were determined using X-ray diffraction method. In the present work, the phase composition of coating was studied using Rigaku D/max-2200/PC series X-ray diffractometer, which is equipped with SA-HF3 model X-Ray tube (Cu-Kα radiation). After recording the XRD spectrum, peak fitting was applied to identify the crystalline phases present by comparison of the angular positions of the peaks with reference patterns from the Powder Diffraction File (PDF2) from the International Centre for Diffraction Data (ICDD).

5.7.1 Through-Thickness Phase Profile

In order to reveal the phase structure through the thickness of PEO coating, the as-prepared coating was grinded on 1200 grit silicon carbide sandpaper successively, using an automated grinding machine, rotating at 150 rpm. After each grinding step, the coating thickness was measured using Mitutoyo Digiderm 1100 coating thickness gauge at multiple points across the surface, and an XRD scan was conducted. The thickness of the coating was reduced by about 10 μm after each grinding step.

Since conventional 2θ/θ scanning methods generally produces a weak signal from especially thin coating and an intense signal from the substrate due to the penetration of X-rays across the porous coating, 2θ scan mode with a low grazing incidence angle was used to avoid intense signal from the substrate and get stronger signal from the coating itself. In Grazing Incidence X-ray Diffraction (GIXRD) technique, only the detector moved, however the tube was held fixed at a low incidence angle of 3°. The X-ray tube voltage and current were 40 kV and 36 mA, respectively. The scan was run from 5° to 90°, with a sampling width of 0.02° and a scan speed of 2°/min. The divergence and scattering slits of 1° were used along with a receiving slit of 0.3 mm.

5.7.2 Quantitative Phase Analysis

The quantitative phase analysis was performed on powder oxide material, which was obtained by rubbing the PEO coated substrates against zirconium oxide ball under a normal load of 10 N. CSM Instruments tribometer was employed to remove the coating material from a total surface area of 6 cm^2, approximately. To avoid the incorporation of titanium metal powder into the coating material, rubbing was stopped when the coating became very thin. After a sufficient amount of powder material was obtained, XRD scan was conducted using 2θ/θ scanning method. The X-ray tube voltage and current were 40 kV and 36 mA, respectively. The scan was run from 5° to 90°, with a sampling width of 0.02° and a scan speed of 2°/min. The divergence and scattering slits of 1° were used along with a receiving slit of 0.3 mm.

In order to calculate the phase proportions, Rietveld refinement was performed using X'Pert Highscore Plus software.

5.8 Electrochemical Corrosion Tests

5.8.1 Experimental Setup

The electrochemical tests were conducted using a standard three electrode electrochemical cell setup with Ag/AgCl reference electrode, a platinum mesh as counter electrode and the test specimen as working electrode (Figure 5.2). The electrochemical behavior of uncoated and coated substrate alloys was studied using the potentiodynamic polarization and electrochemical impedance spectroscopy (EIS) techniques. Prior to starting of the polarization and EIS tests, the open circuit potential (OCP) of the test specimen was allowed to stabilize for 30 min. The naturally aerated solution of sodium chloride (3.5 wt.% NaCl) was used as corrosive medium. Gamry Reference 600 potentiostat was utilized to perform electrochemical measurements.

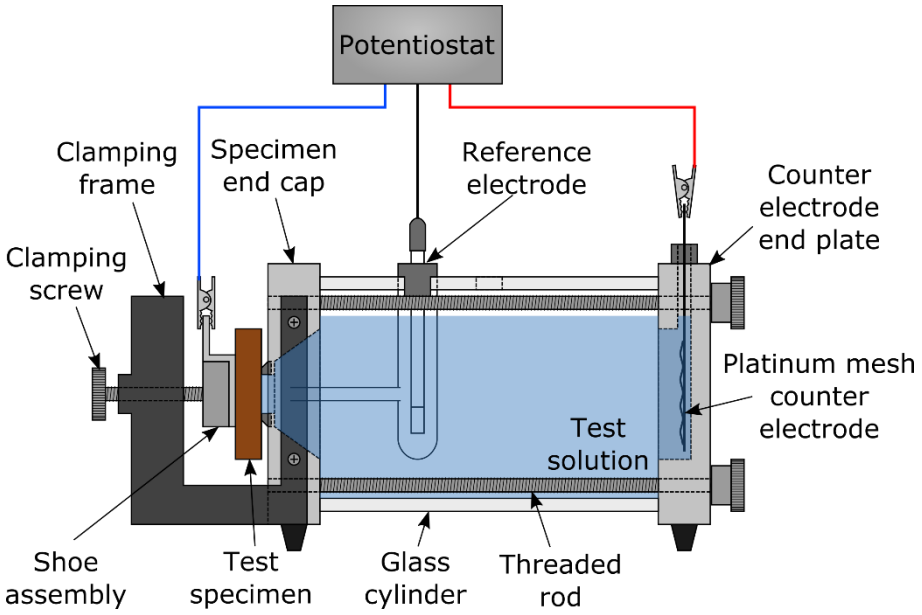


Figure 5.2 Electrochemical cell used in corrosion studies

5.8.2 Potentiodynamic Polarization

Potentiodynamic polarization scan allows considerable information on electrode processes to be acquired. Through this technique, information on the corrosion rate, pitting susceptibility, passivity, as well as the cathodic behavior of an electrochemical system may be obtained.

All DC electrochemical techniques for corrosion-rate determination are directed to measurement of the corrosion current density (i_{corr}), from which the corrosion intensity (in units of mass-loss per unit area per unit time), and the corrosion penetration rate (in units of loss in-dimension perpendicular to the corroding surface per unit time) are calculated. The most fundamental procedure for experimentally evaluating the corrosion current density is by Tafel extrapolation. Tafel plots are generated using one of two methods. In case of first method, Tafel plot anodic and cathodic branches are generated from the same test electrode. Polarization is begun at approximately -200 mV from OCP and increased until the potential is approximately +200 mV from OCP. In case of second method, separate test electrodes are used in the same electrolyte to generate Tafel plot anodic and cathodic branches. The cathodic branch is generated by polarizing one of the test electrodes from OCP to approximately -200 mV from OCP and the anodic branch is generated by polarizing the other test electrode from OCP to approximately +200 mV from OCP. Potential-current data are graphed as applied potential versus log values of current density (Figure 5.3). A potential scan of ± 200 mV about OCP is generally required to determine whether a linear region of at least one decade of current is present in the applied potential versus log values of current density graph such that a reasonably accurate extrapolation can be made to OCP.

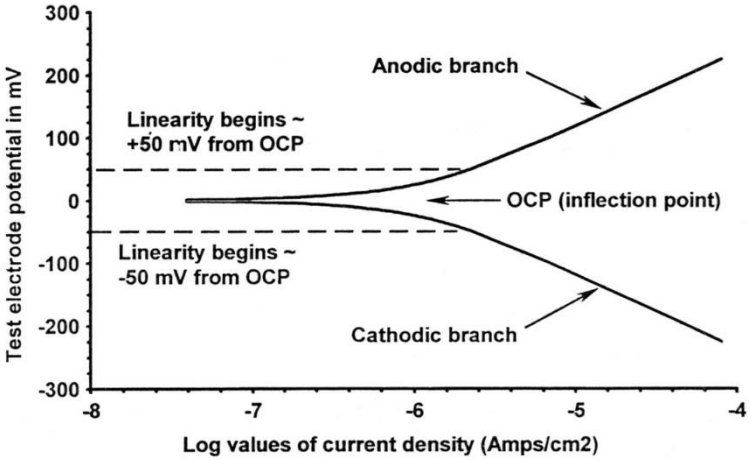


Figure 5.3 Tafel plot for activation controlled corrosion rates (Tait, 1994)

Figure 5.4 contains an example of a Tafel plot where corrosion reaction activation energy controls the corrosion rate. A characteristic of activation control is increasing current density magnitudes with potential increases for both branches. The corrosion current density can be estimated by extrapolating the linear portions of the anodic and cathodic branches in Tafel plot to OCP. Corrosion current for an activation controlled Tafel plot is the intersection of the anodic and cathodic linear extrapolations at OCP, as shown in Figure 5.4. The anodic and cathodic branches correspond to anodic and cathodic half reactions for metal corrosion. Corrosion rate is calculated using corrosion current density (i_{corr}) according to Faraday's law (Equation 5.1).

$$Corrosion\ rate\ \left({}^{mg}/_{dm^2 \cdot day}\right) = 0.0895 \cdot i_{corr}\left({}^{\mu A}/_{cm^2}\right) \cdot EW \tag{5.1}$$

where *EW* corresponds to the equivalent weight of the alloy used in corrosion test. Polarization resistance (R_p) of the alloy can be also calculated by Stern-Geary Equation;

$$R_p = \frac{\beta_a \cdot \beta_c}{2.303 \cdot i_{corr} \cdot (\beta_a \cdot \beta_c)} \tag{5.2}$$

where β_a and β_c correspond to the anodic and cathodic Tafel slopes, respectively. Tafel slopes have units of Volts per current-density-decade, where a decade is one

order of magnitude current density, such as from 0.1 A/cm^2 to 1 A/cm^2. The determination of Tafel slopes is shown in Figure 5.5.

In this study, the potential scan was started from -0.1 V (vs. OCP) and increased with a scan rate of 0.25 mV/s in the noble direction. The polarization from negative to positive potentials was performed in one sweep. The potential scan was stopped at 2 V (vs. OCP).

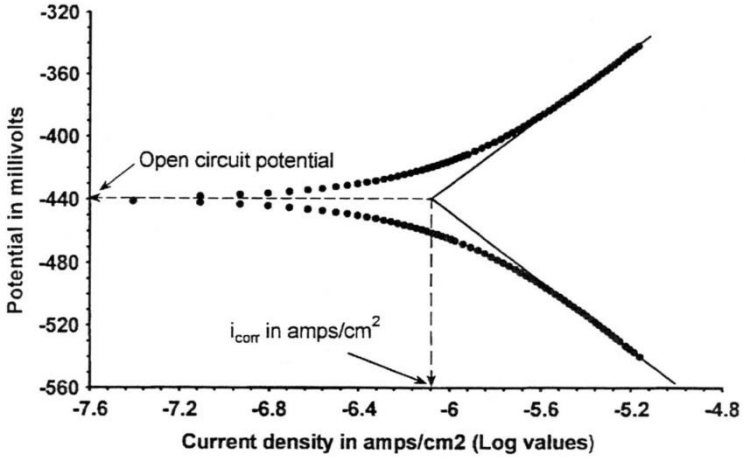


Figure 5.4 A typical Tafel plot representing the linear extrapolations to OCP (Tait, 1994)

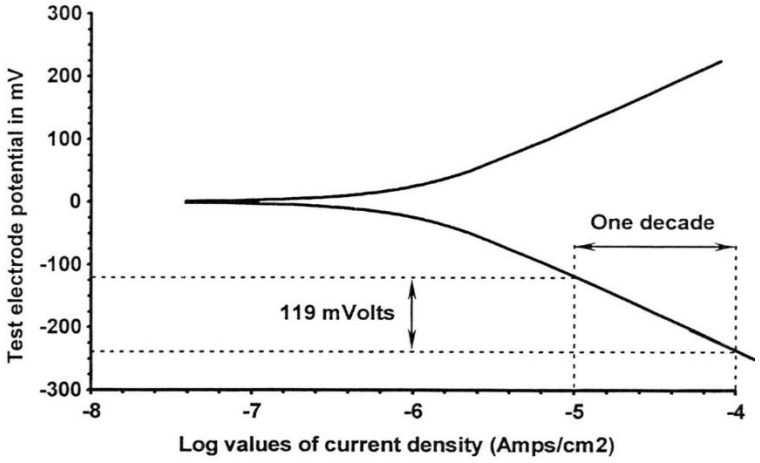


Figure 5.5 Determining Tafel slopes from Tafel plots (Tait, 1994)

5.8.3 Electrochemical Impedance Spectroscopy (EIS)

EIS employs a range of low magnitude polarizing voltages, which cycle from peak anodic to cathodic magnitudes (and vice versa) using a spectrum of alternating current (AC) voltage frequencies, instead of a range of single magnitude and polarity direct current (DC) voltages. EIS polarizing voltage amplitudes typically range from 5 to 20 mV and are generally centered around OCP, as shown in Figure 5.6. The AC voltage amplitude in Figure 5.6 is 5 mV (± 5 mV from OCP) and a complete cycle includes polarizing to a 5 mV peak anodic potential, discharging (to OCP = 0), polarizing to a -5 mV peak cathodic potential, discharging, and again polarizing to a 5 mV peak anodic potential. Two complete cycles are illustrated in Figure 5.6, thus the voltage frequency is 2 cycles/40 seconds, or 0.05 Hz (0.05 cycles per second). Voltage frequencies used for EIS measurements can range from 100 kHz to several mHz. Resistance and capacitance values are recorded at each frequency, and these values can provide information on corrosion behavior and rates, as well as coating properties.

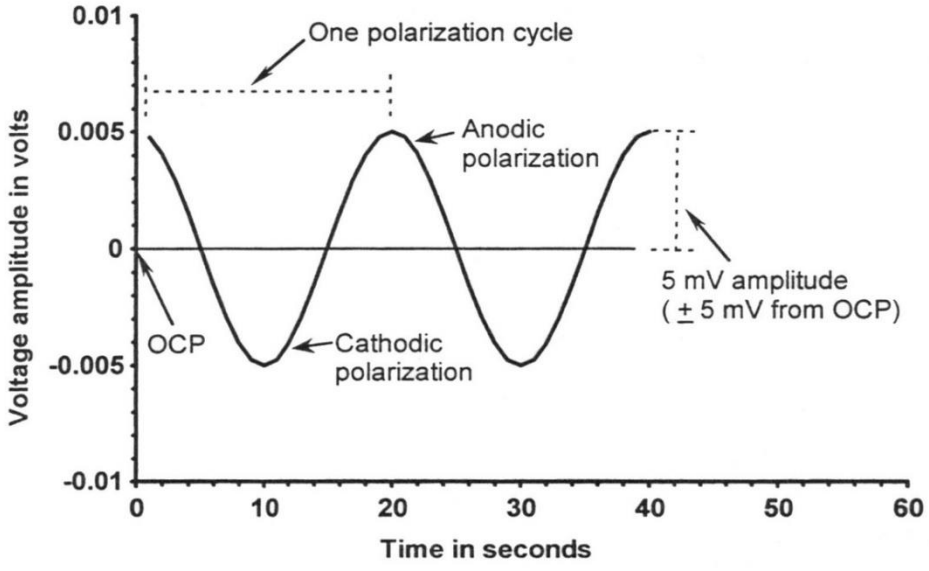


Figure 5.6 Cycle nature of AC voltage (Tait, 1994)

EIS data are usually analyzed by fitting to an electrical equivalent circuit model. Resistors, capacitors, and inductors are the most used equivalent circuit elements for

creating a model representing the physical structure of the electrochemical system. It takes time to fully charge a capacitor, and this charging-time creates a shift between current and voltage amplitude curves, as shown in Figure 5.7. The shift is referred to as the phase angle and its magnitude is different for each voltage frequency. As seen in Figure 5.7, the phase angle is the difference between current and voltage curves when their amplitudes are zero. Phase angle magnitudes are often plotted as positive quantities for EIS data, even though their values are negative. A resistor does not accumulate and separate charge when polarized by an AC voltage, thus it does not exhibit time behavior (or frequency dependency) during polarization and the phase angle is zero. In conclusion, the impedance of a resistor does not depend on frequency whereas an inductor or a capacitor have frequency-dependent impedance values (Orazem & Tribollet, 2008).

The impedance of a circuit element is defined to be:

$$Z = \frac{\Delta V}{\Delta I} \tag{5.3}$$

For a pure resistor, the above equation yields,

$$Z_{resistor} = R \tag{5.4}$$

For a capacitor,

$$Z_{capacitor} = \frac{1}{j\omega C} \tag{5.5}$$

and for an inductor,

$$Z_{inductor} = j\omega L \tag{5.6}$$

where j stands for imaginary number, ω is angular frequency, C and L represent the capacitance and inductance, respectively (Orazem & Tribollet, 2008).

To be useful, the elements used in the equivalent circuit model should have a basis in the physical electrochemistry of the system. For an example, the electrical behavior of an electrical double layer (EDL) on the corroding bare metal surface can be modelled using a simple electrical circuit composed of resistors and a capacitor such as that in Figure 5.8. EDL capacitive reactance is similar to C_{EDL} capacitor capacitance; R_{corr} is similar to corrosion resistance; and R_{Ω} is similar to uncompensated solution resistance (Tait, 1994).

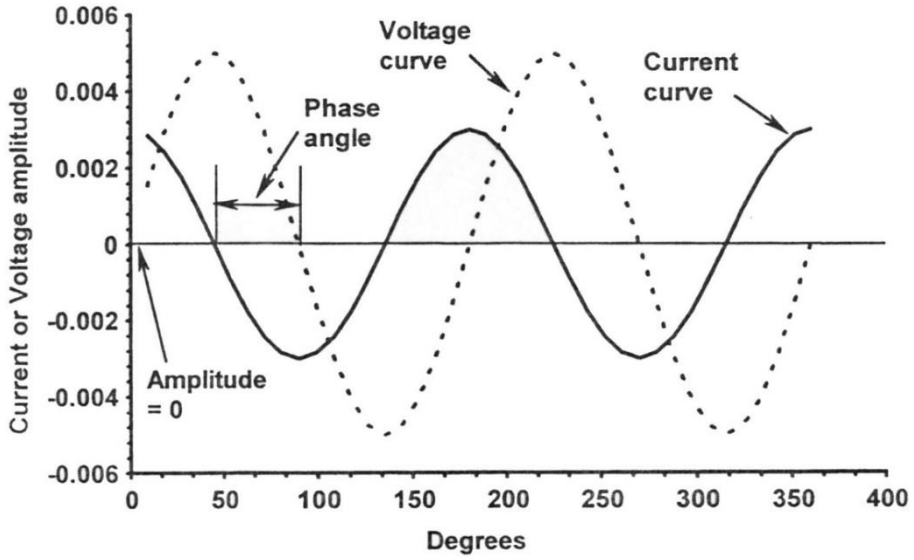


Figure 5.7 AC voltage-current phase angle

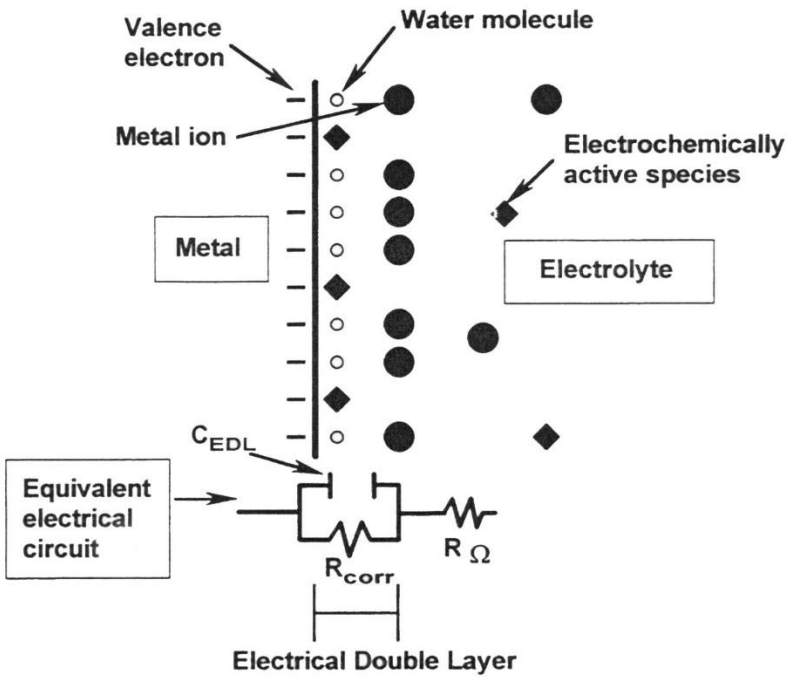


Figure 5.8 Electrical double layer for an uncoated, oxide-free corroding metal (Tait, 1994)

AC current and voltage waves can be characterized by vector analysis since they have magnitude and direction. Consequently, impedance is also a vector because it is AC voltage divided by current. An impedance vector can be resolved into component vectors as illustrated in Figure 5.9, where total impedance is represented by a solid arrow, and component vectors are dashed arrows. Phase angle is the angle between the X-axis and impedance vector. The X- and Y-components of total impedance vector are referred to as real and imaginary impedances, respectively. The total impedance magnitude for an electrical circuit as shown in Figure 5.8, is formulated as follows (PAR application note):

$$Z = R_\Omega + \frac{R_{corr}}{1 + (\omega R_{corr} C)^2} + j\left(\frac{(-\omega R_{corr}^2 C)}{1 + (\omega R_{corr} C)^2}\right) \tag{5.7}$$

In this equation, the second component on the right side represents the real impedance, whereas the third component on the right side is referred to as imaginary impedance since it is multiplied by the imaginary number, j. This equation indicates

that phase angle and total impedance vector takes different values when the polarizing voltage frequency is changed.

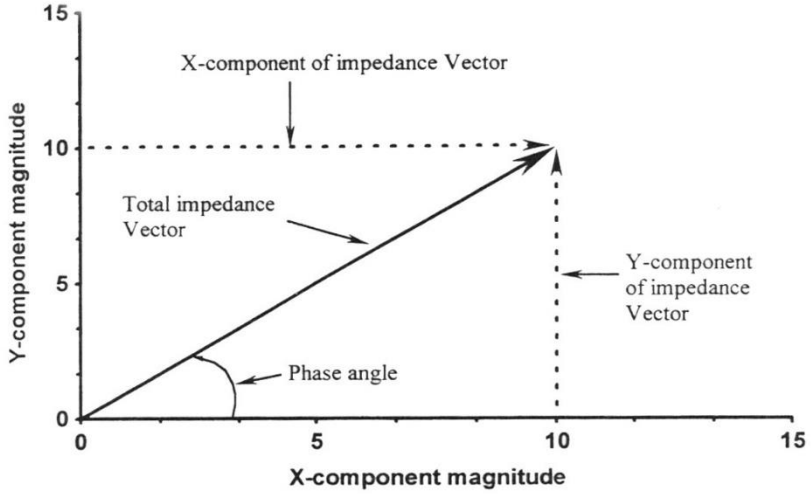


Figure 5.9 Vector nature of voltage and current (Tait, 1994)

EIS data can be graphed a number of different ways using component vector magnitudes, total impedance magnitudes, or phase angles. Three of the most common types of EIS graphs are complex plane plots, Bode magnitude, and Bode phase plots. Complex plane plots, which are also usually called Nyquist plots, include the real and imaginary impedance magnitudes for each polarization frequency. For an example, the first plus second terms in Equation 5.7 is real part and the third term in Equation 5.7 is imaginary part of total impedance. In Figure 5.10, a complex plane plot including a single time constant is shown along with the analogous electrical circuit diagram. The lowest and highest polarization frequencies are noted in parentheses on the right and left sides of semicircle, respectively. The semicircle shape of the plot is due to the existence of capacitive reactance or capacitor. If the parallel resistor in (R_2) is very large, the complex plane plot would look more like a straight line than a semicircle. In Figure 5.10, R_1 equals to uncompensated solution resistance, and R_2 equals to corrosion resistance.

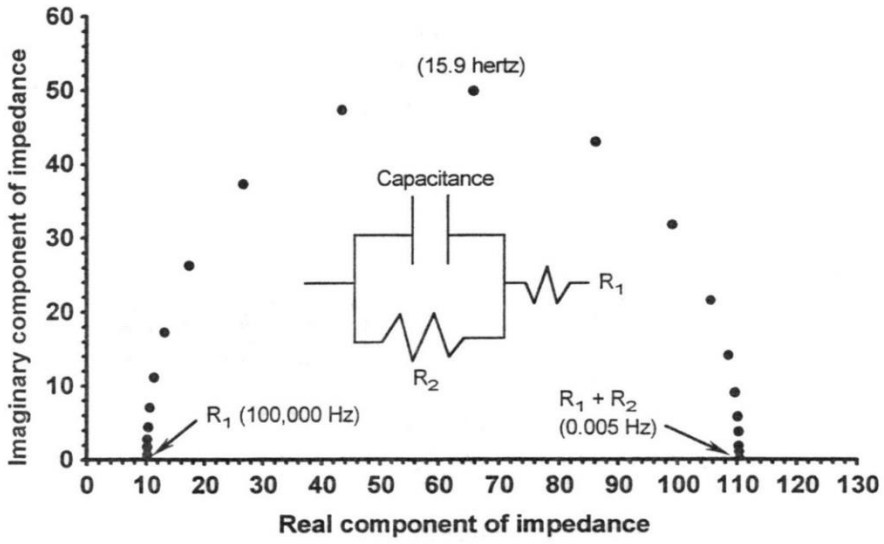


Figure 5.10 Single time constant complex plane plot (Tait, 1994)

The corresponding Bode magnitude and Bode phase plots for complex plane plot in Figure 5.10 are shown in Figure 5.11. In X-axis of both graphs, the log values of frequencies are shown, and in the Y-axis, log values of total impedance and phase angles are given for Bode magnitude and Bode phase plots, respectively. Since the impedance of resistor is not changed with polarization frequency, the slope of the Bode magnitude plot is zero when the polarization is through resistances. In addition, the slope of Bode magnitude plot is negative when the circuit response to a polarization is dominated by capacitive reactance. In Bode phase plot, the inflection point indicates the capacitive reactance and the resistances becomes part of circuit response when the slope is zero.

In this study, the EIS measurements were made by applying an AC signal amplitude of ±10 mV in a frequency range of 10^{5}-10^{-3} Hz with a sampling rate of 10 points per decade.

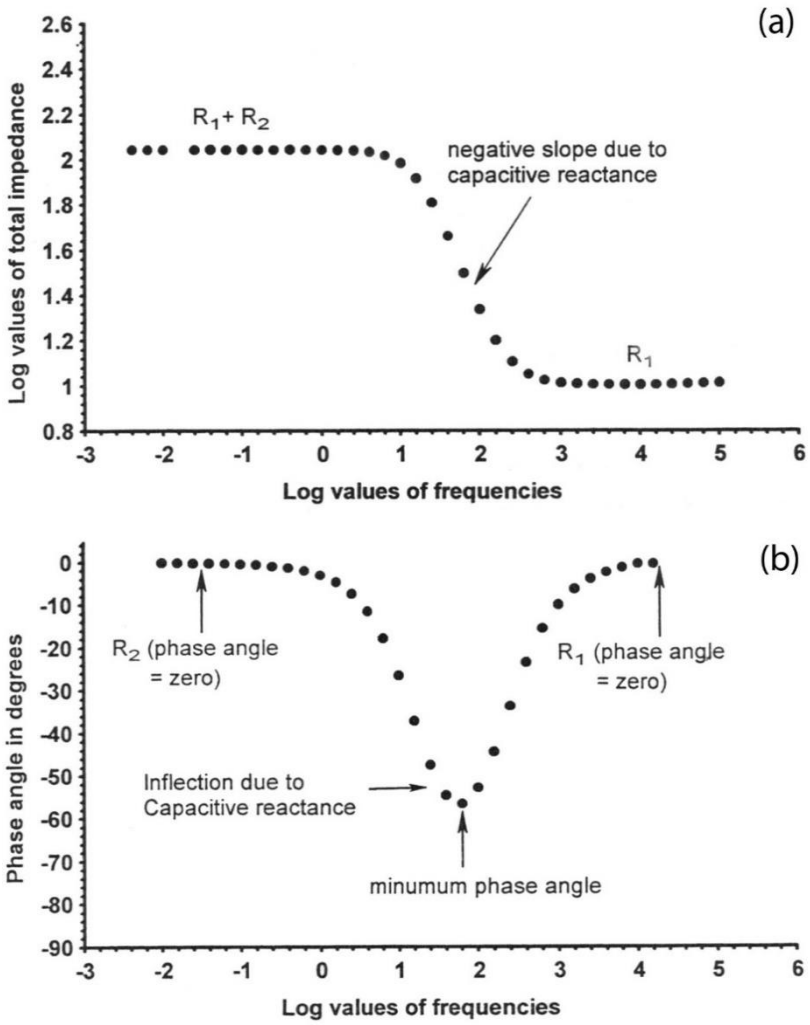


Figure 5.11 Single time constant (a) Bode magnitude plot and (b) Bode phase plot (Tait, 1994)

5.9 Measurement of Hardness and Elastic Modulus

Shimadzu HMV microVickers hardness tester was utilized to obtain the through-thickness hardness profile of coatings produced in aluminate-based electrolytes. The coating thickness was gradually decreased by polishing off a layer of about 10 μm in thickness at each polishing step. Then, out-of-plane indentations at a peak load of 0.025kg were made on polished surface of coating oriented parallel to the substrate surface. This loading value was chosen according to the maximum indentation depth obtained during indentation. It was ensured that the maximum indentation depth would not exceed 10% of the entire coating thickness beginning from the free

surface. This would result in the hardness value not being affected by the properties of the substrate.

Mechanical properties of the coatings such as elastic modulus (*E*) and hardness (*H*) were also obtained using CSM Instruments nanoindentation test machine, which is equipped with a Berkovich indenter and a high resolution optical microscope camera. In-plane indentations at a peak load of 80 mN were produced on polished cross-sections of specimens coated in aluminate based electrolytes with a lateral separation of about 10 μm. Since the coatings formed in phosphate-based electrolyte were thin and porous, out-of-plane nanoindentations were made on slightly polished surfaces of coatings at a peak load of 30 mN. The theoretical background of indentation test which was created by Oliver & Pharr (1992) was used in this study. A schematic view of an indentation and a typical load–displacement curve are given in Figure 5.12. It is stated that the unloading data for an elastic contact for many simple indenter geometries follows a power law that can be written as follows:

$$P = \alpha\left(h - h_f\right)^m \tag{5.8}$$

where P is the indentation load, h is the elastic displacement of the indenter, α and m are constants. Using the initial part of the unloading curve at about 20%, both stiffness S and contact depth h_c are determined by differentiating Equation 5.9 at the maximum depth of penetration, $h=h_{max}$. Then, the stiffness of the contact is given by:

$$S = \frac{dP}{dh} = \frac{2}{\sqrt{\pi}} E_r \sqrt{A_c} \tag{5.9}$$

where E_r is the reduced elastic modulus and A_c is the contact area. According to Oliver and Pharr method, reduced elastic modulus and contact area are calculated as follows:

$$\frac{1}{E_r} = \frac{(1 - v^2)}{E} + \frac{(1 - v_i^2)}{E_i} \tag{5.10}$$

$$A_c = 24.5h_c^2 \tag{5.11}$$

where E and ν are the elastic modulus and Poisson's ratio for the specimen and E_i and ν_i are the same parameters for the indenter, respectively. Similar to the conventional microhardness testing, the indentation hardness can be calculated using the following equation:

$$H = \frac{P_{max}}{A_c} \tag{5.12}$$

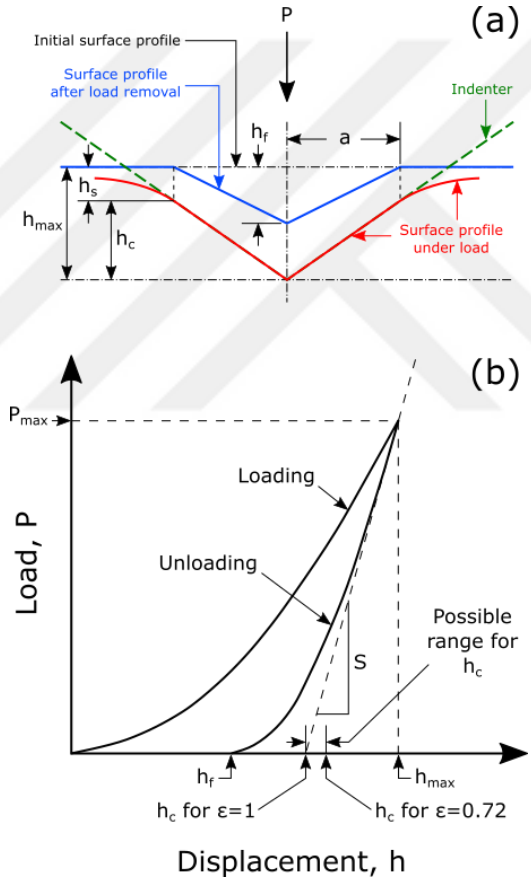


Figure 5.12 (a) Schematic of indentation cross-section and (b) typical load–displacement curve

5.10 Scratch Test

The scratch test is a widely used method to assess the adhesion quality of coatings on different types of substrates. This method consists of generating and assessing the damage events developed in a hard ceramic coating by single point scratch action

(Figure 5.13). A diamond stylus with spherical tip geometry is utilized to apply a normal force onto the coated specimen surface. Simultaneously, the coated specimen is displaced at constant speed while the normal force is increased. At a certain point, the stresses developed within the coating under the applied normal force cause coating damage events (cracking, spalling, chipping etc.). The applied normal force which produces a specific type/level of coating damage is defined as a critical scratch load (L_c). The critical loads are very precisely determined from the fluctuations in the tangential force data, from the acoustic emission signal or can be observed as specific surface deformation in the optical microscope or SEM. For a given substrate/coating combination, one or more different critical scratch loads can be defined for progressive levels of defined coating damage.

In the present work, practical adhesion strength of coatings was evaluated using two different scratch test machines, namely a CSM Instruments microscratch tester, which is able to apply a maximum load of 30 N and a Bruker Universal Mechanical Tester (UMT) that is utilized to apply higher loads than 30 N. Prior to the essential measurement, a pre-scan was performed on the coated surface to detect the surface inclination. Then, to study the progressive damage features in the coating, the normal load on diamond Rockwell stylus with a tip diameter of 200 μm was linearly increased from 0.05 N to 30 N at a normal loading speed of 50 N/min as the coated specimen is displaced at constant speed of 6 mm/min. The total scratch track length was 6 mm. To evaluate the scratch resistance of thick coatings formed in aluminate-based electrolyte, the normal load on diamond Rockwell stylus was linearly increased from 0.5 N to 70 N as the coated specimen is displaced at constant speed of 0.1 mm/s. After the scratch test, a post-scan at the surface was carried out to evaluate the elastic recovery of the coating-substrate system. During the scratch test, the normal load, penetration depth and acoustic emission signal were recorded to determine the critical scratch loads at which specific damage failures are observed. In addition to supplementary data graphics, the scratch on the coating surface was examined under optical microscope and SEM to precisely determine the position at which the coating damage events occurred.

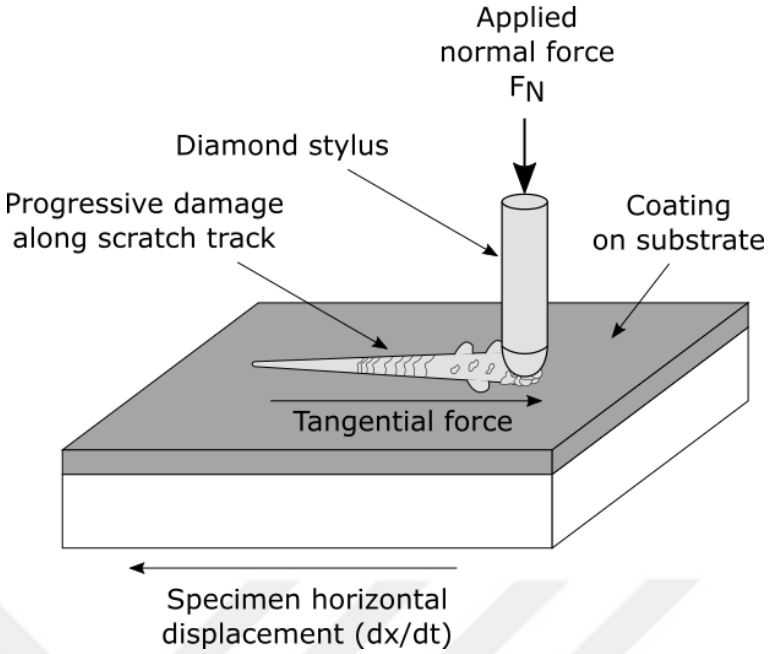


Figure 5.13 Schematic example of progressive damage in scratch track in a progressive load scratch test

5.11 Wear Test

The wear behavior of uncoated and coated substrates was studied using a linear reciprocating ball-on-flat configuration (Figure 5.14). This test method involves a spherically ended upper specimen (generally a ball-shaped specimen) and a flat lower specimen which slides against the ball specimen. The ball is rigidly mounted and the load is applied vertically downward through the ball specimen against the horizontally mounted flat specimen that is moved backwards and forwards in a reciprocating motion under a prescribed set of conditions (sliding velocity, sliding distance and stroke length, etc.). The friction force is determined during the test by measuring the deflection of the elastic arm with inductive displacement transducer and is used to obtain friction coefficient data. The friction coefficient data are usually required to assess the transitions in wear behavior, which are frequently associated with the changes in friction.

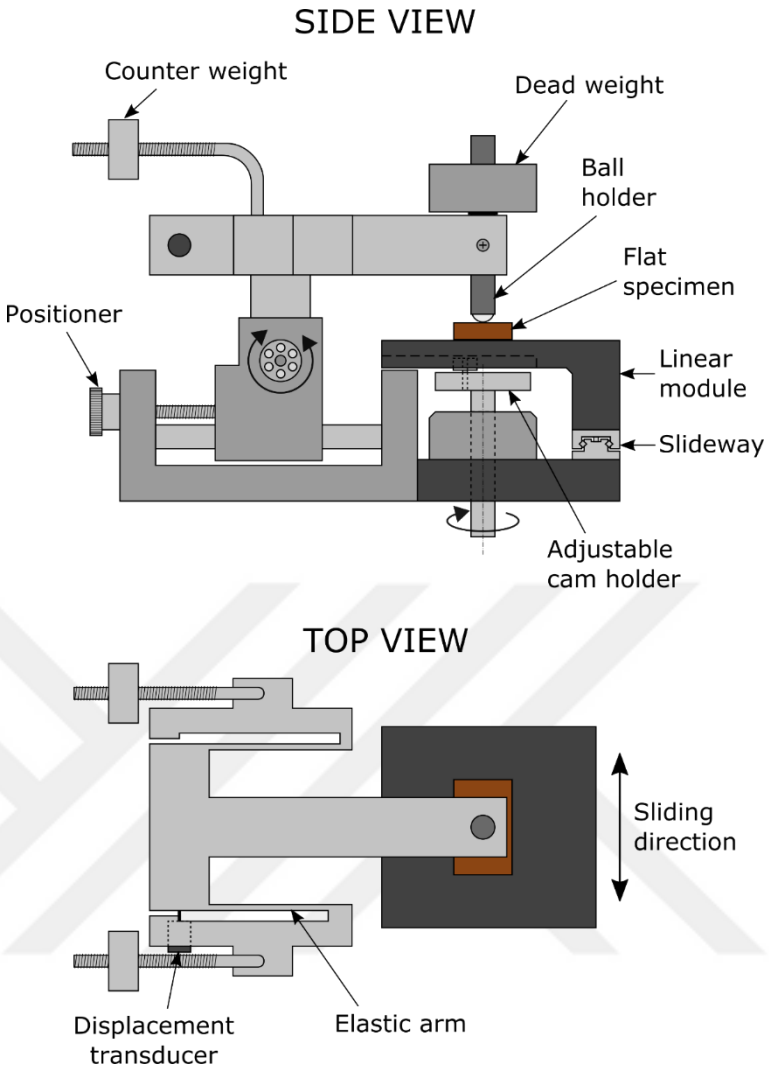


Figure 5.14 Schematic of CSM Instruments standard tribometer

In the present work, CSM Instruments standard tribometer was utilized to perform linear reciprocating wear tests. Prior to wear test, the bare substrates and thick coatings formed in aluminate-based electrolytes were grinded using 400, 800, 1200 and finally 2000 grit silicon carbide papers to obtain an almost similar surface finish. The thickness of thick coatings formed in aluminate-based electrolytes was decreased to 25 μm after grinding process. But thin coatings formed in phosphate-based electrolyte is used in as-coated condition due to its low surface roughness. After grinding step, the specimens were cleaned in ethanol ultrasonically for two minutes and dried in hot air subsequently. Dry sliding wear tests were performed at loads of 1-10 N by applying a constant sliding velocity of 0.06 m/s. The stroke length and the total sliding distance were 10 mm and 100 m, respectively. The ball

specimens (Ø 6 mm, grade 10) used in wear test were made of AISI 52100 steel and aluminum oxide.

After wear test, the wear track on coated substrate was investigated using SEM to reveal the wear mechanisms. The material loss for uncoated and coated substrates was estimated from the wear track profile using stylus profilometer, as described in Section 5.6. In some wear tests, the steel ball rubbed against coated specimen possessed significant wear loss. The wear volume of ball specimen with a flat wear scar was calculated using the following equations:

$$Volume\ loss, V_p = \left(\frac{\pi h}{6}\right) \cdot \left(\frac{3d^2}{4} + h^2\right) \tag{5.13}$$

$$h = r - \left(r^2 - \frac{d^2}{4}\right)^{1/2} \tag{5.14}$$

where d is the wear scar diameter and r is the ball radius.

CHAPTER SIX
RESULTS

6.1 Introduction

In the present study, PEO coatings were produced on CP-Ti and Ti6Al4V alloys using phosphate- and aluminate-based electrolytes with a pulsed bipolar AC power supply operating at a constant frequency of 50 Hz. Different chemicals were added into the aluminate-based electrolyte to investigate their effect on the structural, electrochemical, mechanical and tribological properties of coatings. Different post-treatments including silane-based sealer and MoS_2 solid lubricant were applied to relatively thin coatings formed in phosphate-based electrolyte in order to improve their electrochemical and tribological properties.

6.2 The Voltage-Time Response

The variation of voltage during PEO processing of CP-Ti and Ti6Al4V alloys in phosphate- and aluminate-based electrolytes are shown in Figure 6.1 and Figure 6.2, respectively. In the initial stage of PEO process, the voltage increased rapidly forming an anodic oxide film on the metal surface. After a certain time, the dielectric breakdown voltage of oxide film has been reached, where sparks began to appear around the edges of specimen, then spread to the whole specimen surface. The breakdown voltage is about 175 V for phosphate-based electrolyte, while this value ranges from 250 to 270 V for aluminate-based electrolytes. In case of aluminate-tungstate electrolyte, the time to reach the breakdown voltage is relatively longer compared to other aluminate-based electrolytes. After dielectric breakdown, sparks gradually evolved into more intense microarcs at first, then powerful arcs formed at the end of PEO processing in aluminate-based electrolytes. However, the sparks formed in phosphate-based electrolyte existed throughout the processing time and some microarcs, which are more intense and larger than sparks, appeared on the edges of the specimen as the process ended. In all stages of PEO treatment, gas evolution was accompanied by plasma discharges. As the process continues, the

voltage remained almost constant, except for the aluminate-phosphate and aluminate-pyrophosphate electrolytes, which showed some voltage oscillations in the last 15 min. These may be attributed to the powerful arcs which could damage the coating at some surface regions. The damaged coating area might have lower dielectric strength than surrounding surface regions, thus the voltage drops to lower values as in aluminate-phosphate electrolyte. After the damaged region is plugged with new oxide material either coming from the electrolyte species or substrate material, the voltage begins to rise.

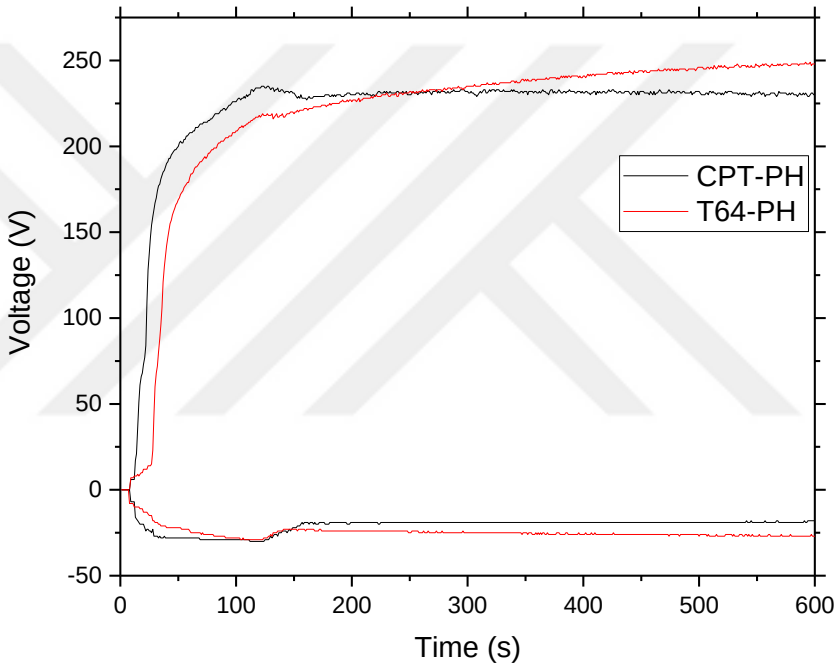


Figure 6.1 Variation of voltage during PEO processing of CP-Ti and Ti6Al4V alloys in phosphate-based electrolyte

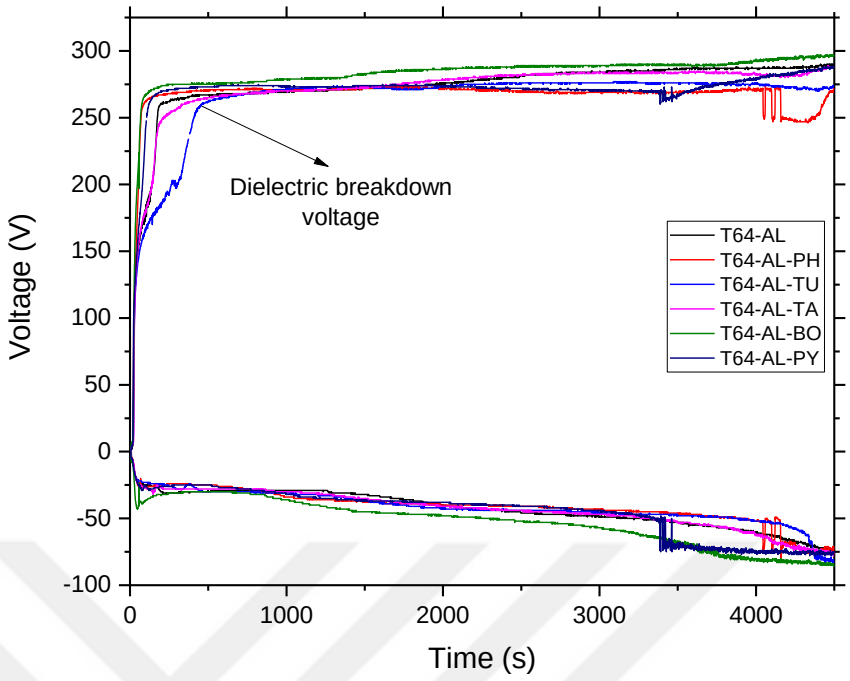


Figure 6.2 Voltage-time responses for PEO processing of Ti6Al4V in aluminate-based electrolytes

6.3 Surface Morphology and Cross-Sectional Analysis

The surface morphology and cross-sections of thin coatings produced on CP-Ti and Ti6Al4V alloys using phosphate-based electrolyte are shown in Figure 6.3. Since the coating produced on Ti6Al4V showed almost similar surface morphology with that produced on CP-Ti alloy, only the surface image of coating formed on CP-Ti alloy is given in this study. A large number of small-sized micropores are observed on the surface of coating. These are the traces of individual discharge channels formed during PEO treatment. There are no evident sintered particles on the surface. As is seen in the cross-sectional images, the coating has a two-layered structure including a non-porous barrier layer at the substrate/coating interface and a top porous layer, which is thicker than the underlayer.

The surface morphology of thick coatings produced on Ti6Al4V alloy using aluminate-based electrolytes differs from that of thin coatings produced in phosphate-based electrolyte. As seen in Figure 6.4 and with higher magnification in Figure 6.5, there are many small-scale pores and a few large-scale pores on the

surface. The molten oxide material emanating from discharge channel solidified immediately after coming in contact with the electrolyte. These are seen as sintered particles on the surface. It has been also observed that the thermal stress, which is caused by instantaneous local heating and cooling of the oxide material close to the discharge channel, resulted in cracking, as seen in detailed SEM images of coating surface (Figure 6.5).

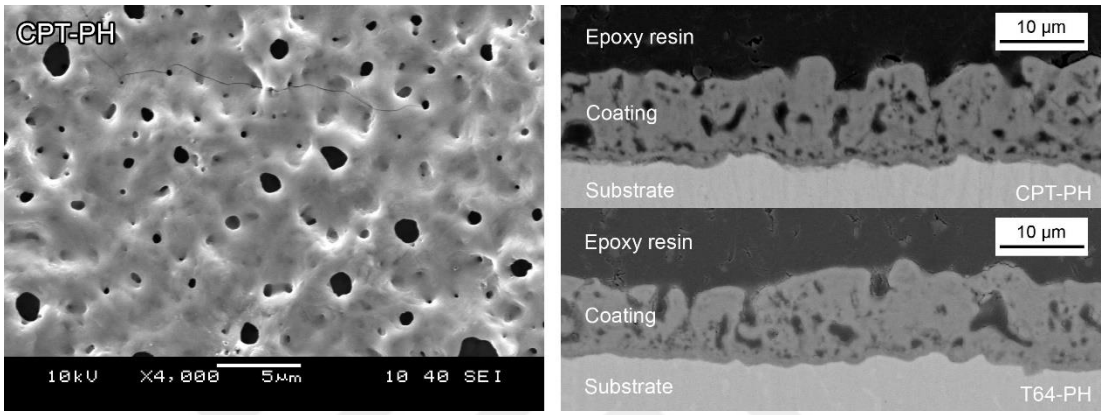


Figure 6.3 Surface morphology and cross-sections of coatings produced on CP-Ti and Ti6Al4V alloys using phosphate-based electrolyte

As seen from the cross-sectional images in Figure 6.6, the porosity of thick coatings formed in aluminate-based electrolytes is less than that of thin coatings (Figure 6.3) produced in phosphate-based electrolyte, however, the pore sizes of thin coatings are smaller than those of thick coatings. All coatings that were formed in aluminate-based electrolytes have almost a dense microstructure exhibiting some micro-scaled pores distributed throughout the section of coating and some of them are present at the coating/substrate interface. The micropores are probably the results of gas entrapment in discharge channels during the PEO process. The addition of different chemicals into the main electrolyte increased the size and amount of micropores, except for tungstate additive. It is also apparent that all coatings have a wavy boundary region which may be related to the powerful microarcs formed in the later stages of process duration and penetrated into the substrate alloy. Due to these powerful microarcs, the thermal gradient in the electrolyte/coating interface is increased and rapid solidification of molten oxides caused thermal shrinkage cracks on the outermost layer of coatings.

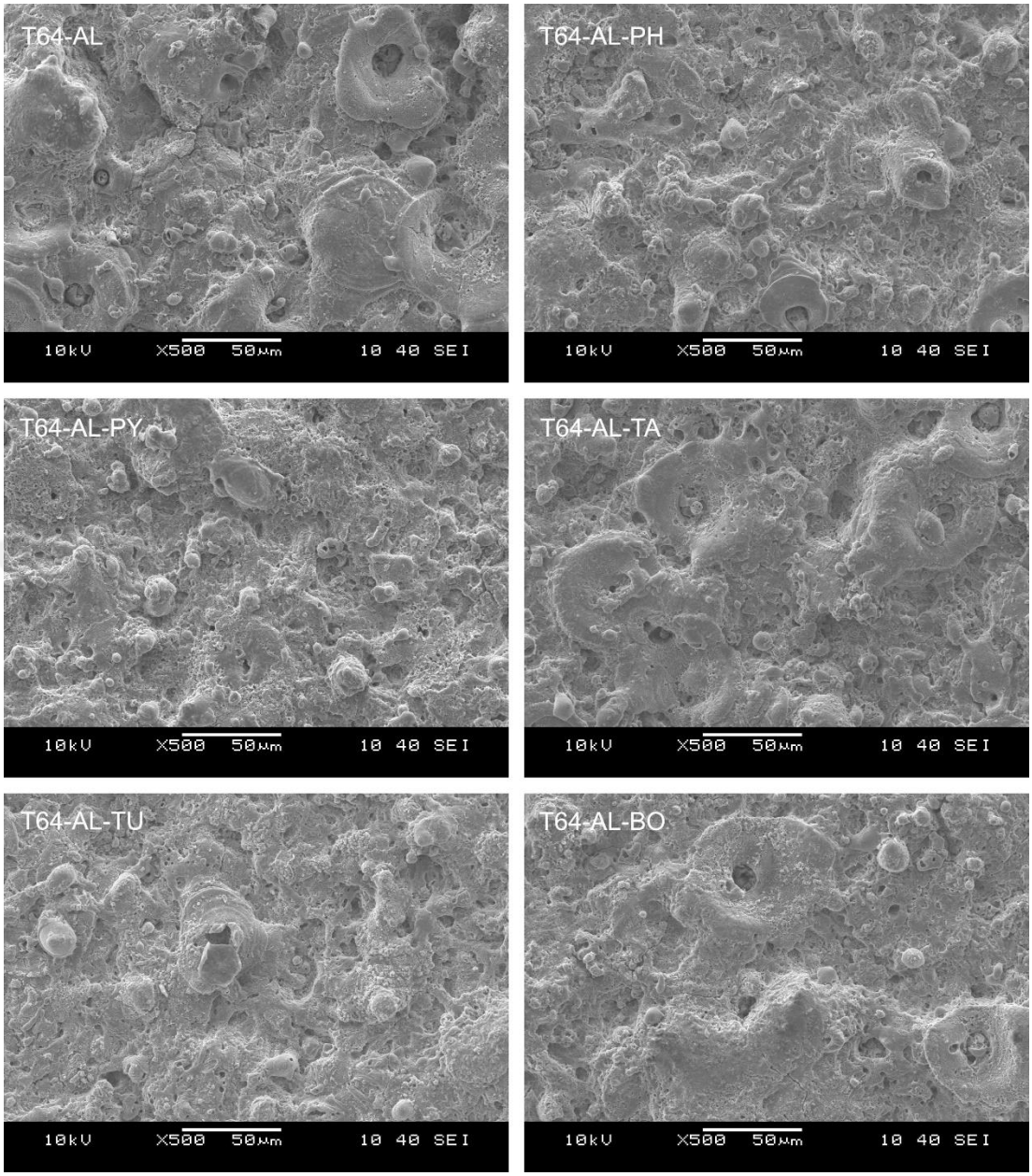


Figure 6.4 Surface morphology of coatings produced in aluminate-based electrolytes

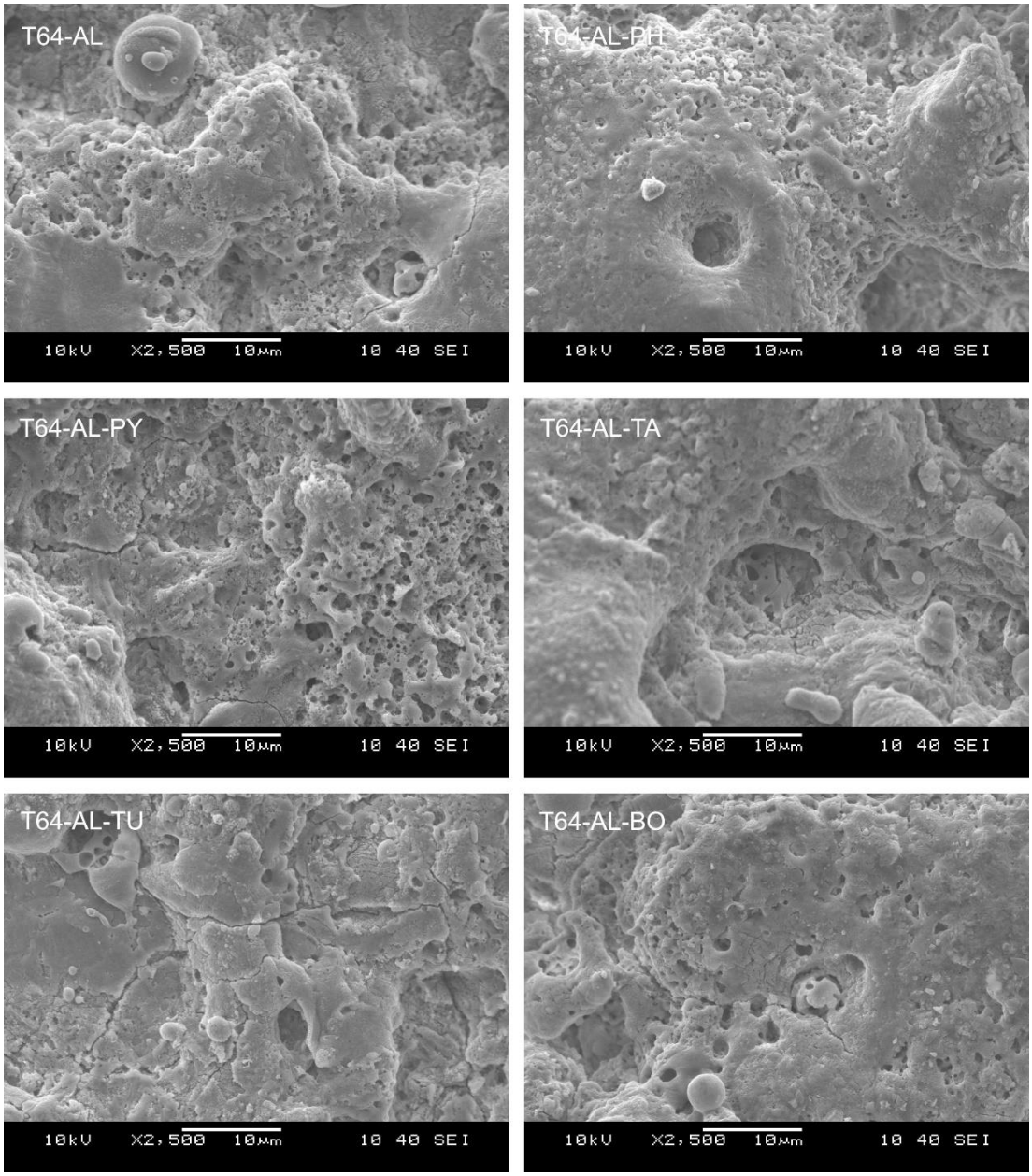


Figure 6.5 Detailed SEM images showing the surface morphology of coatings formed in aluminate-based electrolytes

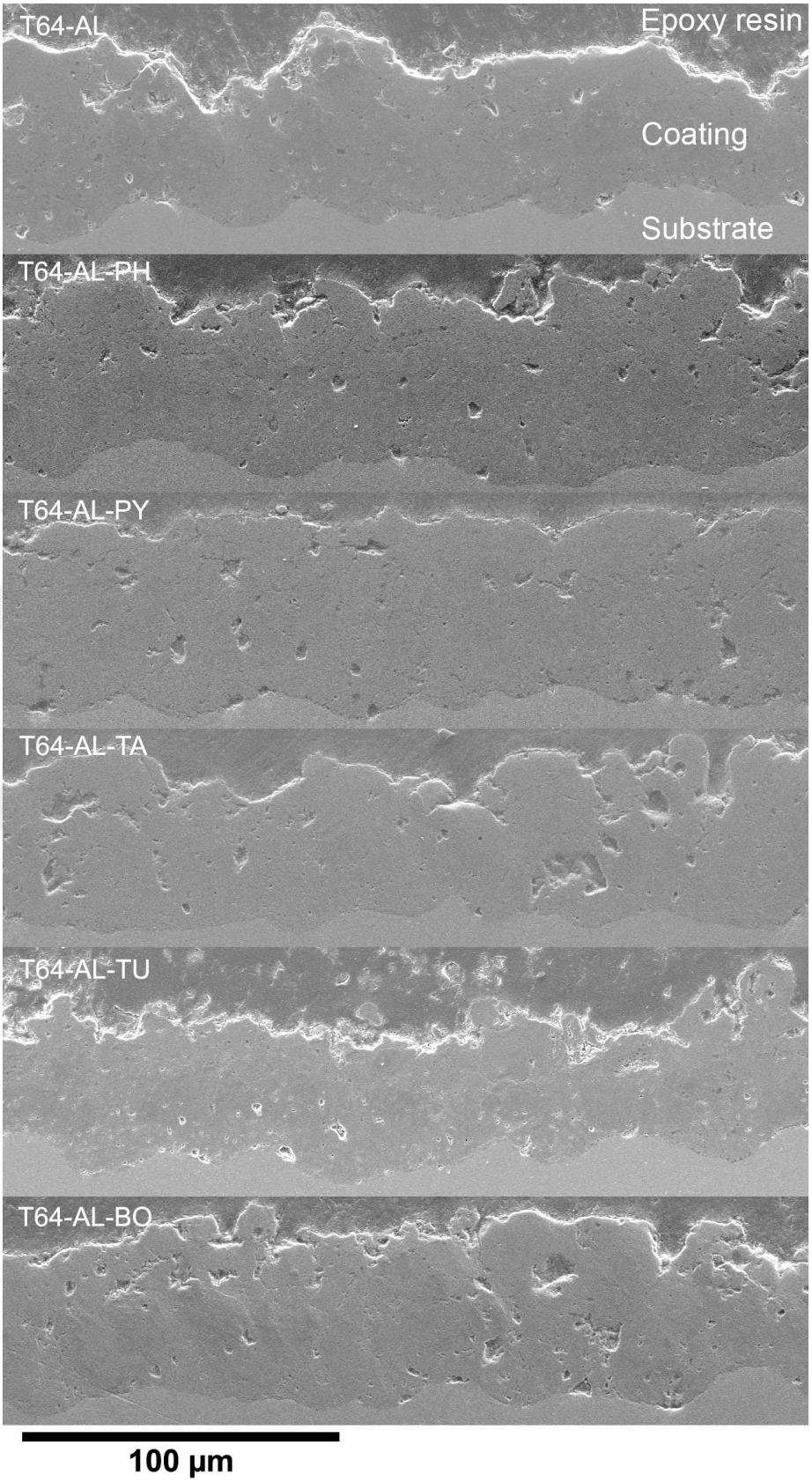


Figure 6.6 Cross-sectional SEM images of coatings produced on Ti6Al4V alloy using aluminate-based electrolytes

The surface morphology of silane-treated PEO coating produced on CP-Ti using phosphate-based electrolyte and the cross-section of PEO coating on Ti6Al4V with MoS_2 friction modifier are shown in Figure 6.7. It has been observed that the silane treatment did not change the surface morphology of as-prepared coating given in Figure 6.3 Silane-based solution penetrated into the micropores and microcracks to form a very thin surface film rather than forming a thick layer that covers the whole surface. The MoS_2 top-coat is uniformly distributed on the coating and has an average thickness of 3 ± 1 μm.

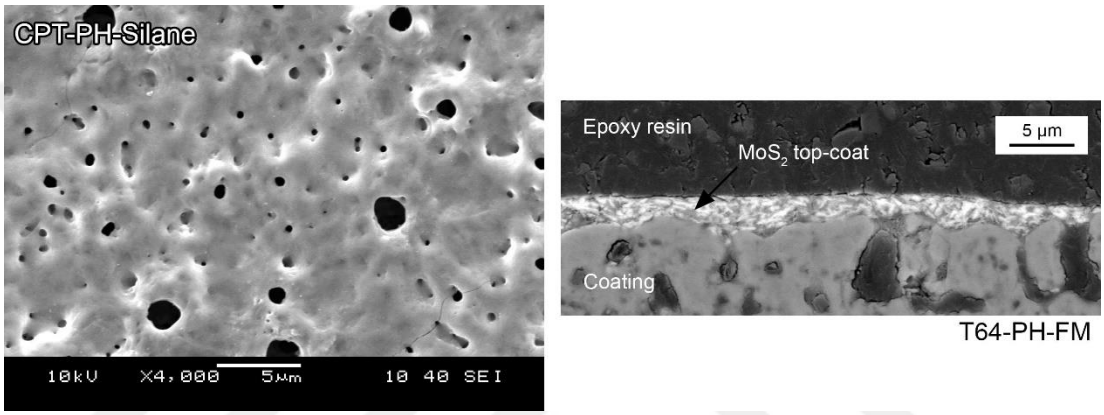


Figure 6.7 Surface morphology of coating with silane treatment and cross-section of coating with MoS_2 topcoat

The surface roughness of coatings measured using surface profilometer and thickness of coatings calculated by SEM image analysis are listed in Table 6.1. The coatings produced on CP-Ti and Ti6Al4V alloys using phosphate-based electrolyte have smother surface than that produced using aluminate-based electrolyte due to their low thickness. As PEO treatment progresses, it is observed that the size of discharges increased while their population decreased. Since the current density was kept constant during PEO process, the intensity of individual discharges increased causing more molten oxide material to erupt and solidify around the discharge channels irregularly, leading to obtain a rough coating surface. The addition of phosphate and pyrophosphate into the aluminate electrolyte decreased the surface roughness and increased the thickness, whereas in case of tungstate and tartrate containing electrolytes, average thickness is reduced and roughness values are almost

similar to the aluminate electrolyte. Borate addition did not have a significant influence on the roughness and thickness of coating.

Table 6.1 Surface roughness and thickness of coatings

Coating	R_a (µm)	R_z (µm)	R_t (µm)	Average thickness (µm)
CPT-PH	0.60 ± 0.02	3.54 ± 0.18	5.59 ± 0.26	10.5
T64-PH	0.48 ± 0.03	3.21 ± 0.16	4.20 ± 0.23	9.9
T64-AL	6.14 ± 0.39	41.87 ± 2.89	49.89 ± 2.3	51.7
T64-AL-PH	4.43 ± 0.22	30.93 ± 2.4	35.92 ± 2.27	57.7
T64-AL-PY	4.64 ± 0.08	31.1 ± 0.33	37.42 ± 0.96	57.3
T64-AL-TA	5.75 ± 0.17	37.27 ± 1.42	45.85 ± 4.09	45.6
T64-AL-TU	6.03 ± 0.37	41.13 ± 1.76	50.11 ± 5.69	44.8
T64-AL-BO	5.41 ± 0.12	38.49 ± 0.29	49.81 ± 6.91	50.3

6.4 Phase Analysis

During PEO treatment, the surface regions of oxide material in close proximity to a plasma discharge channel is locally heated and cooled, yielding to recrystallization of the substances deposited onto the surface. Consequently, decomposition of aluminum hydroxides to aluminum oxide, formation of complex oxide compounds including Ti-Al binary metal oxides, as well as high-temperature transformations of titanium oxide and aluminum oxide, can occur (Yerokhin et al., 2002). The type of oxide phases and their relative amounts are depended on the power of the discharges, which is determined by the oxide film thickness, so that more powerful and extended discharges are developed as the thickness of oxide layer is increased.

The XRD patterns of PEO coatings produced on CP-Ti and Ti6Al4V alloys using phosphate-based electrolyte are shown in Figure 6.8. PEO coatings exhibit phase modifications of titanium oxide, namely rutile and anatase, suggesting that the coating growth was mainly assisted by the anodic oxidation of substrate alloy. The XRD patterns of powder oxide material detached from coatings that were produced on Ti6Al4V in aluminate-based electrolytes are shown in Figure 6.9. In all coatings, the main structural component is aluminum titanium oxide (Al_2TiO_5), which

originates from the incorporation of electrolyte species, probably aluminum hydroxides, into the coating structure through the discharge channels. When aluminum hydroxides come into contact with the fused titanium oxide, they form crystalline aluminum titanium oxide phase in accordance with the plasma-assisted chemical reactions which are suggested by Yerokhin et al. (2002). As the coating thickness is increased, metastable anatase and cubic aluminum oxide were transformed into more stable rutile and corundum, respectively, by the local heating effect of powerful discharges.

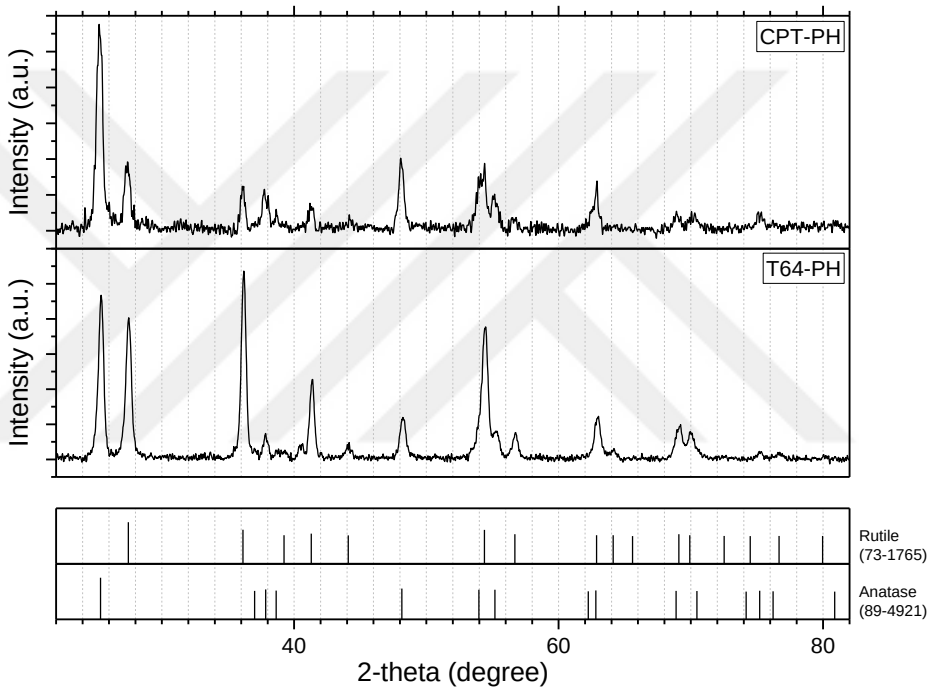


Figure 6.8 XRD patterns of coatings produced on CP-Ti and Ti6Al4V alloys using phosphate-based electrolyte

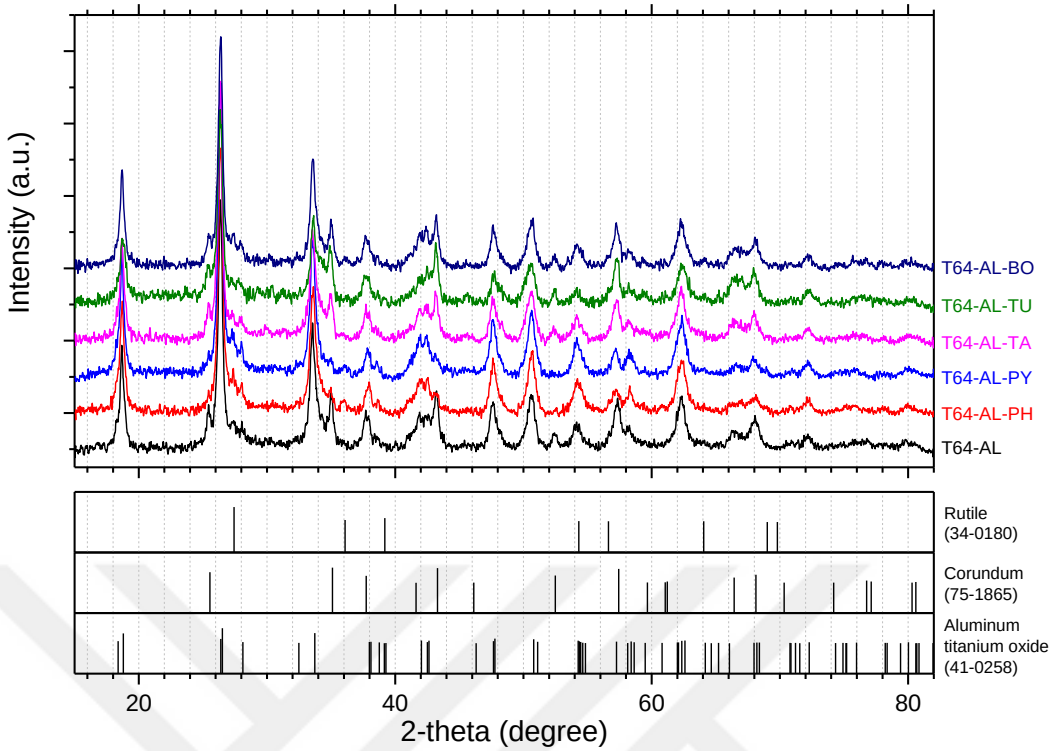


Figure 6.9 XRD patterns of powder material that is obtained by rubbing the PEO coatings produced on Ti6Al4V alloy using aluminate-based electrolytes

The relative amounts of phases calculated using the XRD patterns of powder oxide materials are listed in Table 6.2. The amount of aluminum titanium oxide is much higher than rutile and corundum. It is also observed that the coatings produced in aluminate-phosphate and aluminate-pyrophosphate electrolytes have less amount of corundum than those produced in other electrolytes. This suggests that the addition of phosphate and pyrophosphate into the aluminate electrolyte suppresses the formation of corundum. The highest amount of corundum was obtained with the addition of tungstate into the aluminate electrolyte.

Table 6.2 Relative amounts of phase constituents in PEO coatings produced using aluminate-based electrolytes

Coating	Al_2TiO_5 (wt. %)	Corundum (wt. %)	Rutile (wt. %)
T64-AL	68.8	27.7	3.5
T64-AL-PH	79.2	16.5	4.4
T64-AL-PY	83.9	9.7	6.4
T64-AL-TA	73	23.5	3.5
T64-AL-TU	69.1	30.9	ND*
T64-AL-BO	71.2	24.3	4.5

*Not detected

The through-thickness phase profiles of coatings produced on Ti6Al4V alloy using aluminate-based electrolytes are shown in Figure 6.10 through Figure 6.15. As seen in XRD patterns, aluminum titanium oxide existed throughout the thickness of coating but the corresponding peak intensities at around 26.5° and 50.8° (2θ) are decreased slightly closer to the substrate/coating interface. Corundum has a similar phase profile to aluminum titanium oxide, except that some peaks belonging to corundum disappear near the substrate, especially for polished coating of 10 μm thickness. On the other hand, the intensity of rutile peak at around 27.4° (2θ) is increased significantly as the thickness of coating was reduced to 10 μm thickness by successive polishing. This was an expected result, since the incorporation of electrolyte species into the coating is limited to some extent as the coating thickness is increased, and the formation of corundum is reduced near the substrate/coating interface. The excess amount of titanium oxide close to the substrate, which was not contributed to the formation of aluminum titanium oxide, transformed into rutile phase.

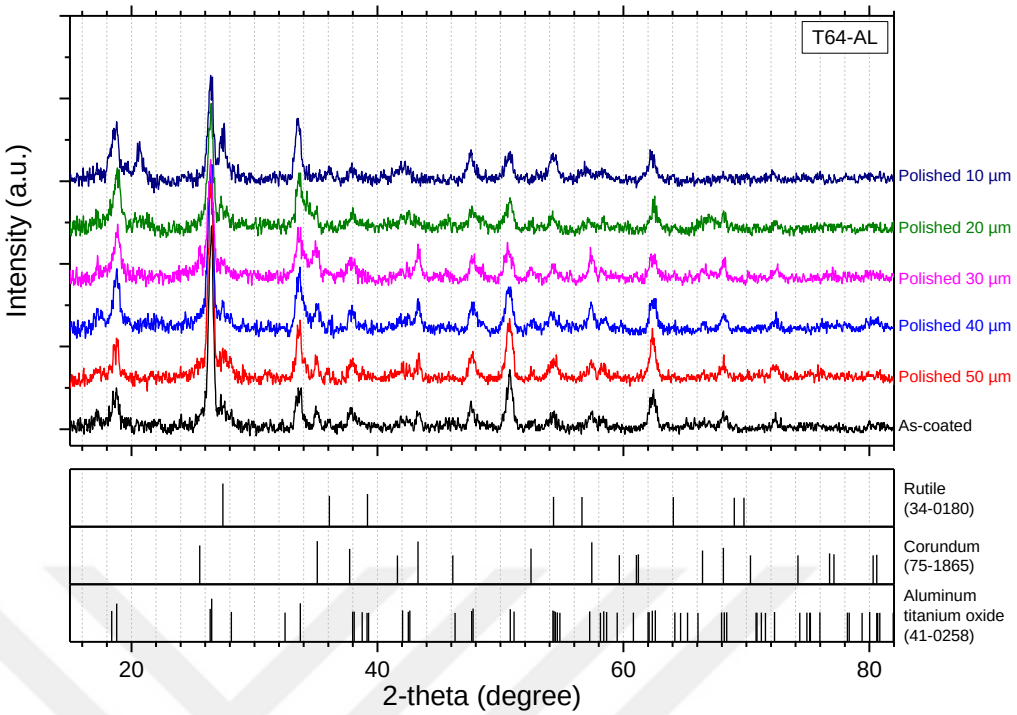


Figure 6.10 Through-thickness phase profile of coatings produced in aluminate electrolyte

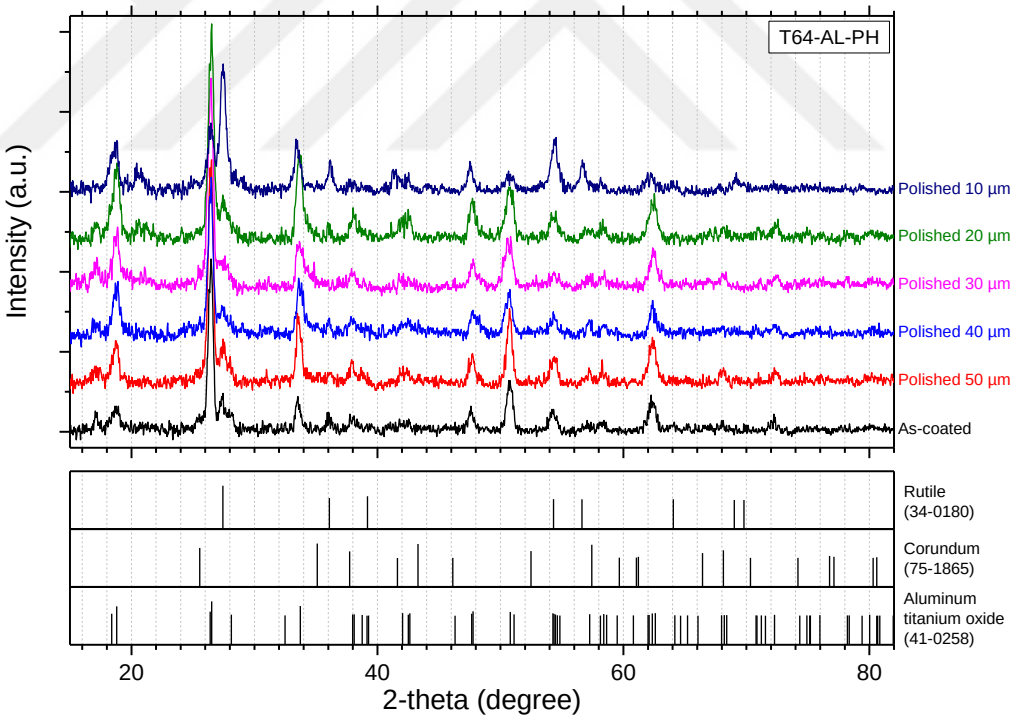


Figure 6.11 Through-thickness phase profile of coatings produced in aluminate-phosphate electrolyte

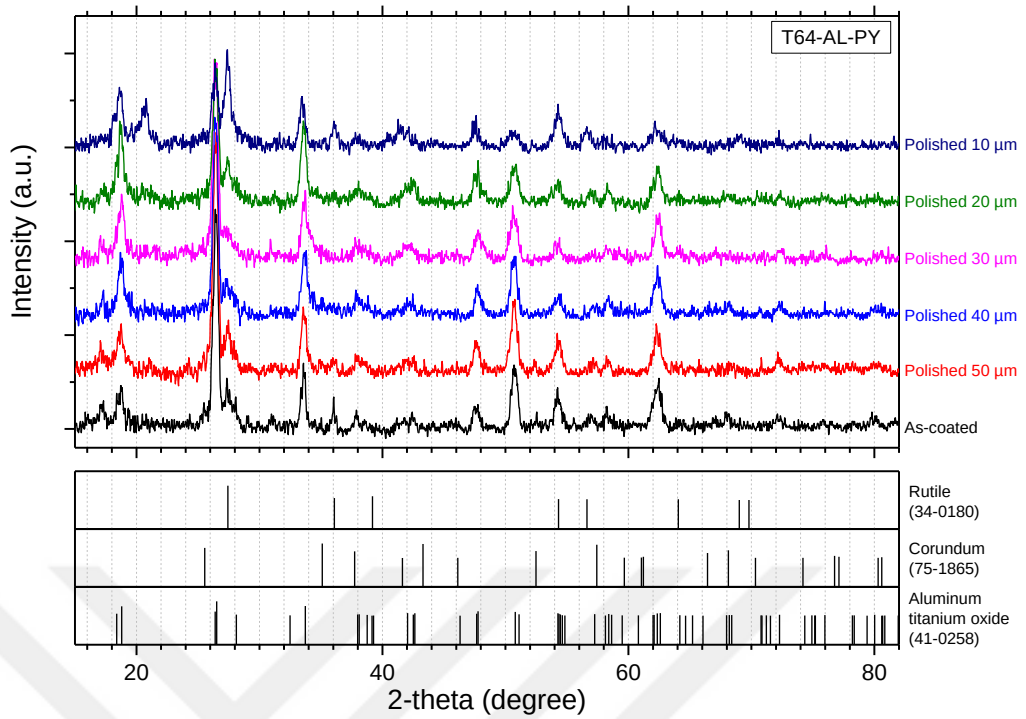


Figure 6.12 Through-thickness phase profile of coatings produced in aluminate-pyrophosphate electrolyte

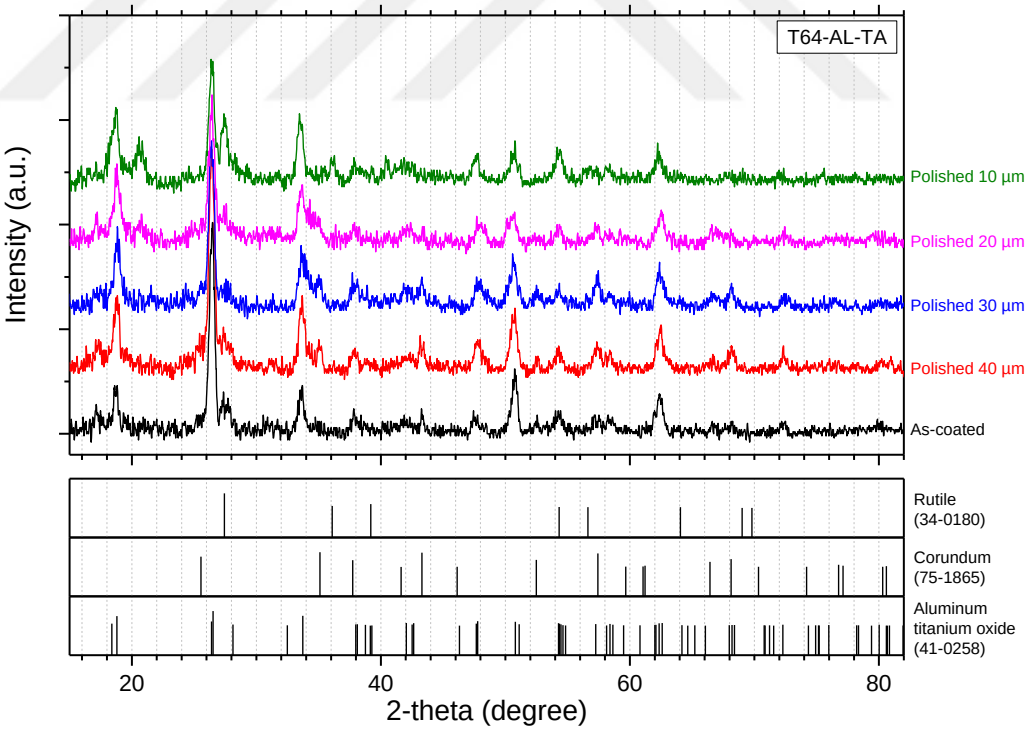


Figure 6.13 Through-thickness phase profile of coatings produced in aluminate-tartrate electrolyte

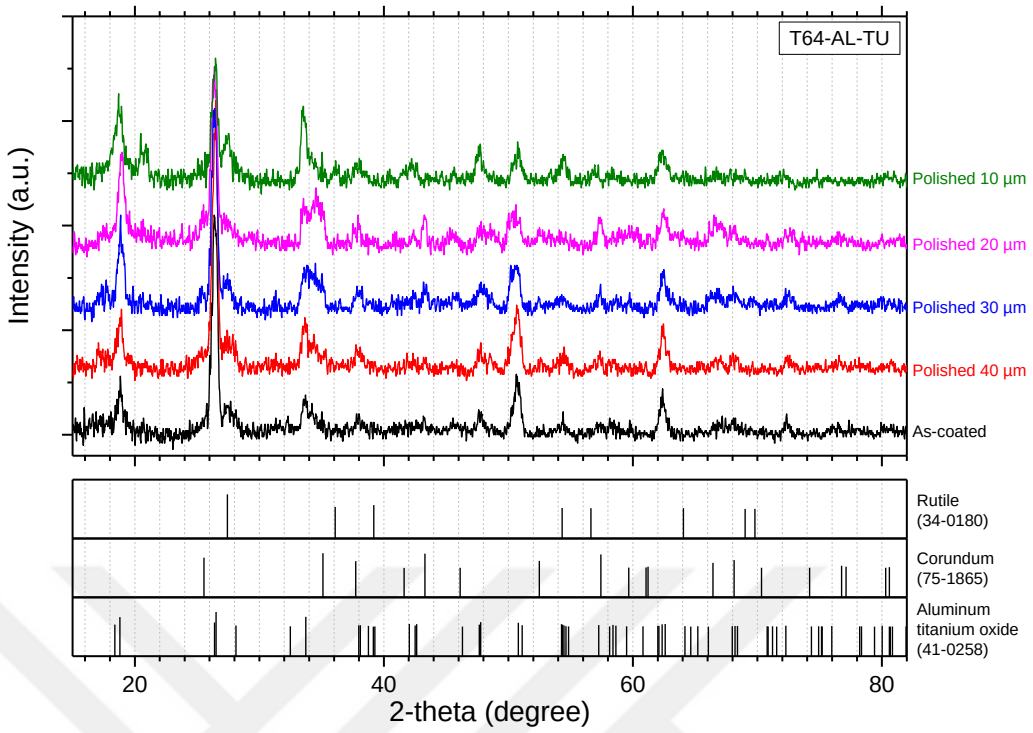


Figure 6.14 Through-thickness phase profile of coatings produced in aluminate-tungstate electrolyte

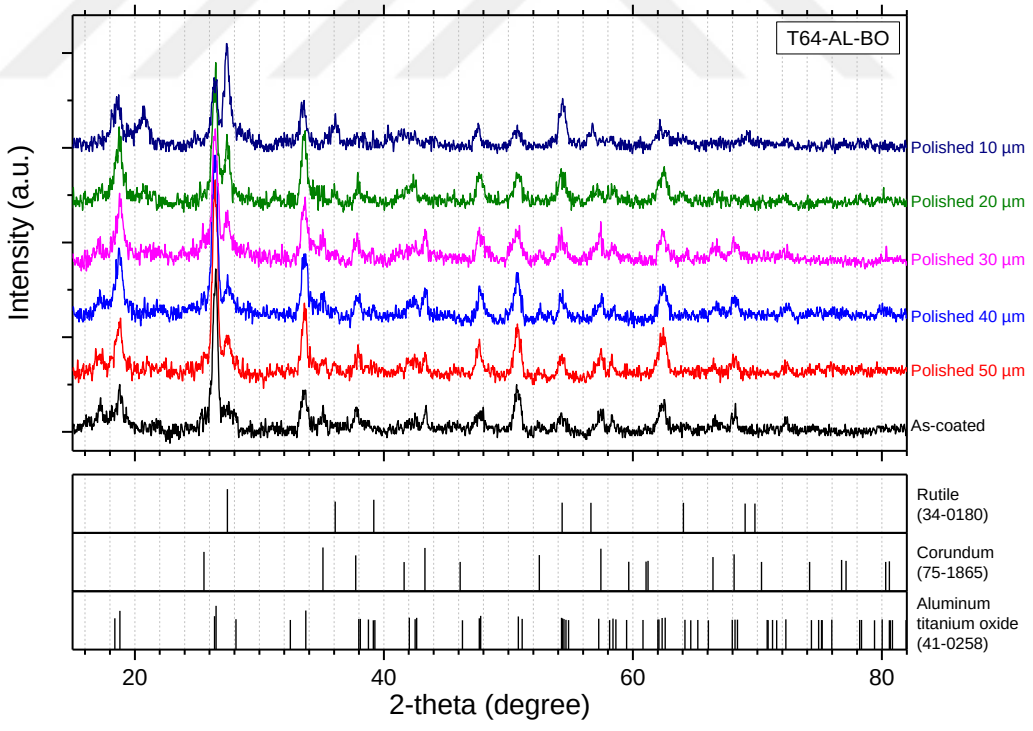


Figure 6.15 Through-thickness phase profile of coatings produced in aluminate-borate electrolyte

6.5 Electrochemical Corrosion Properties

6.5.1 Potentiodynamic Polarization

The potentiodynamic polarization graphs of coatings tested in 3.5 wt.% NaCl solution, and the corrosion properties such as corrosion potential and corrosion current density that are obtained by Tafel extrapolation are shown in Figure 6.16 and Table 6.3, respectively. The corrosion potential explains the tendency of a material to corrosion and is mainly related to the chemical composition of the material. As is seen in Table 6.3, all coatings produced using phosphate-based and aluminate-based electrolytes increased the corrosion potential values of CP-Ti and Ti6Al4V alloys in the noble direction, indicative of a stable coating in the corrosive medium. It has been also observed that the aluminate-based electrolytes provided higher corrosion potential values than phosphate-based electrolyte. Moreover, the corrosion current density is utilized to calculate the electrochemical corrosion rate of specimens. Thin coatings produced using phosphate-based electrolyte decreased the corrosion rate of titanium alloys slightly, but thick coatings formed in aluminate-based electrolytes increased the corrosion rate of Ti6Al4V alloy by a factor of about 2.5. Thus, in order to obtain high corrosion resistance, it is more beneficial to apply thin coatings on titanium alloys than thick coatings. It has been suggested that the barrier layer at the substrate/coating interface, as is seen in the cross-section of coatings formed in phosphate-based electrolyte (Figure 6.3), inhibits the diffusion of corrosive species such as chloride ions into the substrate during polarization test and this results in improved corrosion resistance. However, the micropores that are located at the substrate/coating interface of thick coatings, as is seen in Figure 6.6, can be the main reason for decreased corrosion resistance. Further decrease in the corrosion rate of coated CP-Ti alloy was obtained by application of silane-based film on the surface. As seen in Table 6.3, silane treatment decreased the corrosion rate of coating produced on CP-Ti using phosphate-based electrolyte by a factor of 18. It has been observed that the silane treatment penetrates into the micropores making it hydrophobic rather than forming a coating that covers the whole pores on the

surface. Hydrophobic surface retards the breaking of the oxide film on the substrate alloy and thus prevents the titanium alloy underneath from further corrosion.

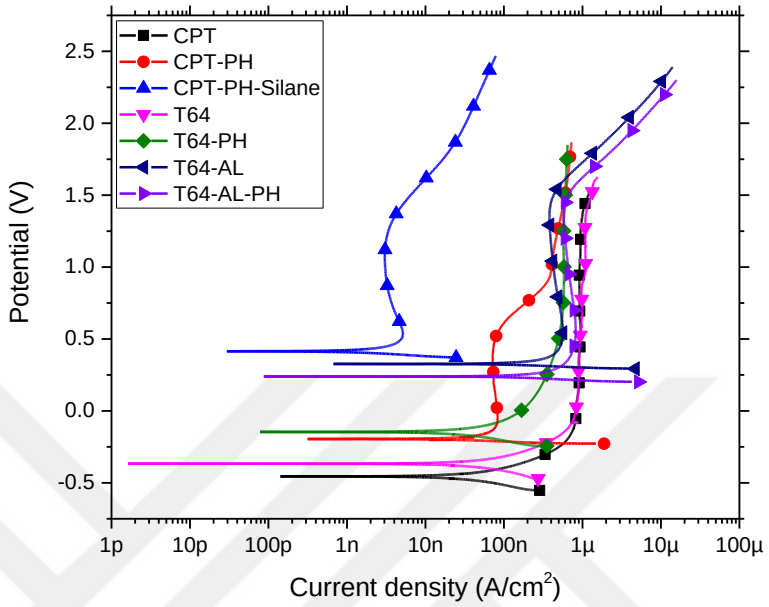


Figure 6.16 Potentiodynamic polarization graphs of coatings tested in a naturally aerated 3.5 wt.% NaCl solution at a scan rate of 0.25 mV/s at ambient temperature

Table 6.3 Corrosion properties of coatings that were obtained by Tafel extrapolation

Specimen	Corrosion potential (V)	Corrosion current density (A/cm^2)	Corrosion rate ($mg/cm^2 \cdot year$)
CPT	-0.456	$88 \cdot 10^{-9}$	0.35
CPT-PH	-0.196	$46 \cdot 10^{-9}$	0.18
CPT-PH-Silane	0.412	$2.86 \cdot 10^{-9}$	0.01
T64	-0.367	$102 \cdot 10^{-9}$	0.39
T64-PH	-0.147	$89.2 \cdot 10^{-9}$	0.34
T64-AL	0.326	$245 \cdot 10^{-9}$	0.93
T64-AL-PH	0.239	$272 \cdot 10^{-9}$	1.04

6.5.2 Electrochemical Impedance Spectroscopy

The Nyquist and Bode plots of uncoated and coated CP-Ti alloy in phosphate-based electrolyte are shown in Figure 6.17 through Figure 6.19. The equivalent circuit models that were used for fitting the impedance spectra and the corresponding

results are given in Figure 6.20 and Table 6.3, respectively. As seen in Figure 6.17, the impedance spectrum of uncoated Ti6Al4V has a capacitive loop indicating single time constant that consists of a resistor and a constant phase element in parallel. In this model, R_{sol} is the solution resistance, R_{ct} is the charge transfer resistance at the metal/electrolyte interface, Q_0 is the constant-phase element representing the capacitance of double layer. The impedance response of electrodes rarely show the ideal response expected for single electrochemical reactions. Thus, the constant-phase element (CPE) is used in equivalent circuit models instead of capacitors. The impedance associated with a constant-phase element can be expressed as:

$$Z = \frac{1}{Q_0(j\omega)^n} \tag{6.1}$$

where n and Q are parameters associated with a constant-phase element. When this equation describes a capacitor, the constant Q_0 = C (the capacitance) and the exponent n = 1. For a constant phase element, the exponent n is less than one (Orazem & Tribollet, 2008).

The impedance spectra of coatings exhibited two time constants characteristic of PEO coatings on titanium (Gnedenkov et al., 2006; Matykina et al., 2013). In the equivalent circuits, R_{sol} is the solution resistance, R_{po} is the resistance of the porous layer in parallel with constant phase element Q_{po}, and R_b is the coating/substrate interface resistance or barrier layer resistance in parallel with Q_b. The equivalent circuit model also included an additional element of Warburg impedance which describes the diffusion processes inside the micropores of coating with irregular shape. For all coated substrate alloys, the sum of resistance values (R_{po} and R_b) basically shows the total impedance of the system. It has been observed that the application of PEO coating increased the total impedance of CP-Ti alloy considerably by a factor of about 30. In addition, the silane-treated coating improved the barrier properties of coating and nearly a threefold increase in the total impedance of as-prepared coating was obtained.

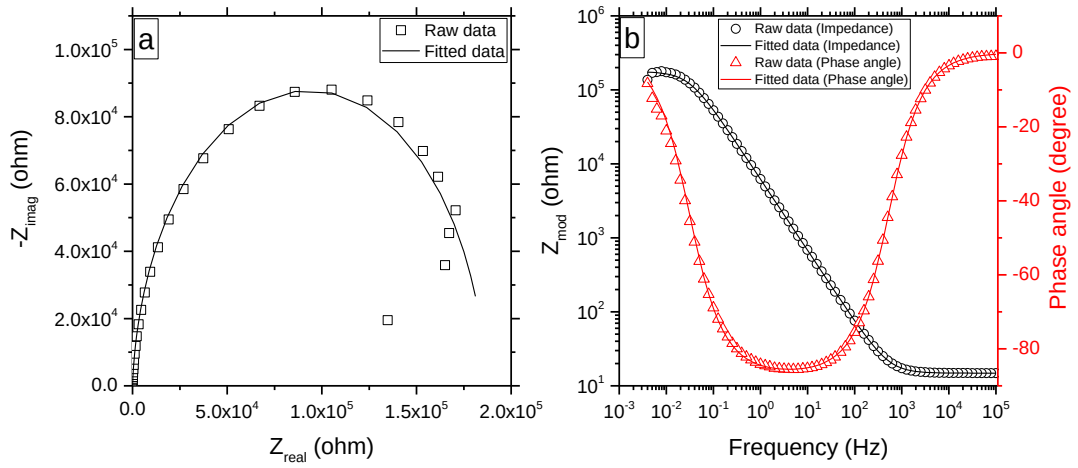


Figure 6.17 (a) Nyquist and (b) Bode plots of bare CP-Ti alloy in wt.% 3.5 NaCl solution

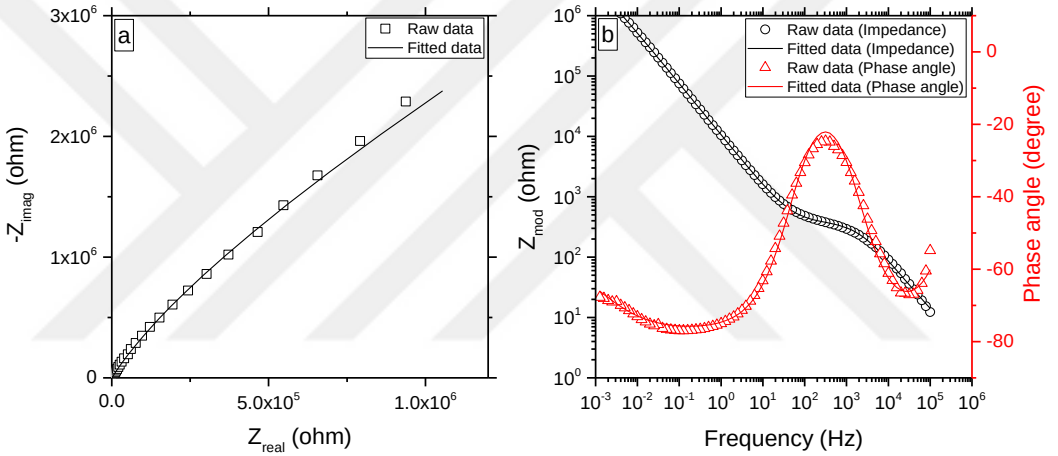


Figure 6.18 (a) Nyquist and (b) Bode plots of as-prepared coating on CP-Ti in wt.% 3.5 NaCl solution

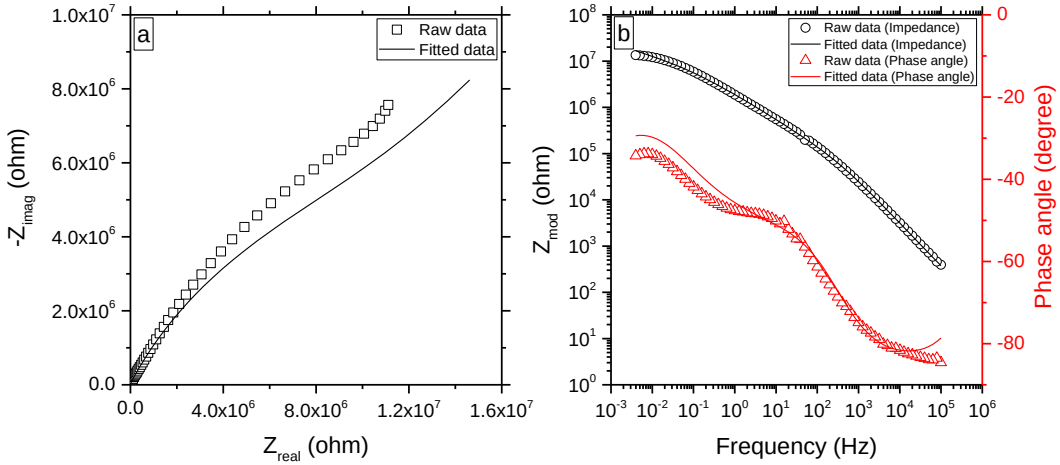


Figure 6.19 (a) Nyquist and (b) Bode plots of thin coating on CP-Ti with silane treatment in wt.% 3.5 NaCl solution

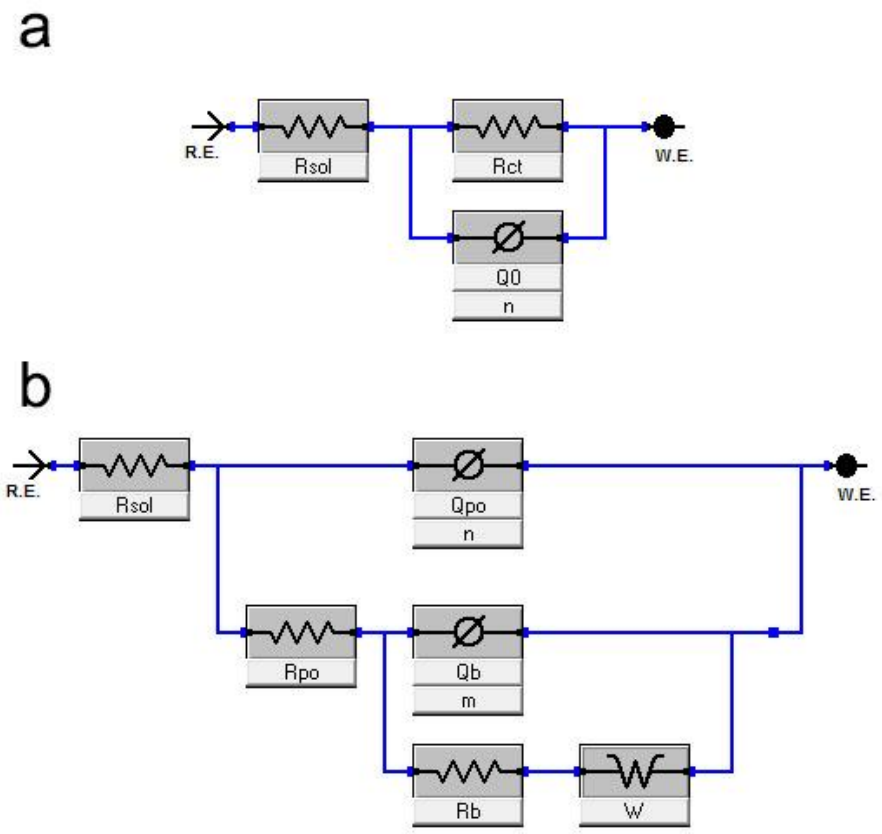


Figure 6.20 Equivalent circuit models that were used in fitting the impedance spectra of (a) bare CP-Ti, (b) CPT-PH and CPT-PH-Silane coatings

Table 6.4 EIS fitting results obtained using the equivalent circuit models

Electrical circuit element	CPT	CPT-PH	CPT-PH-Silane
R_{sol} (ohm)	14.82 ± 0.087	3.76 ± 0.38	31.64 ± 10.43
R_{ct} (ohm)	$186.7 \cdot 10^{3} \pm 2.02 \cdot 10^{3}$	-	-
Q_0 ($S \cdot s^n$)	$27.56 \cdot 10^{-6} \pm 167.9 \cdot 10^{-9}$	-	-
n	0.961 ± 0.0013	-	-
R_b (ohm)	-	$5.217 \cdot 10^{6} \pm 1.54 \cdot 10^{6}$	$17.72 \cdot 10^{6} \pm 1.55 \cdot 10^{6}$
Q_b ($S \cdot s^m$)	-	$18.9 \cdot 10^{-6} \pm 179.5 \cdot 10^{-9}$	$174.5 \cdot 10^{-9} \pm 4.57 \cdot 10^{-9}$
m	-	0.851 ± 0.003	0.531 ± 0.008
R_{po} (ohm)	-	390.7 ± 6	$109.8 \cdot 10^{3} \pm 16.2 \cdot 10^{3}$
Q_{po} ($S \cdot s^n$)	-	$880.3 \cdot 10^{-9} \pm 71.7 \cdot 10^{-9}$	$11.1 \cdot 10^{-9} \pm 0.78 \cdot 10^{-9}$
n	-	0.853 ± 0.007	0.928 ± 0.006
W ($S \cdot s^{1/2}$)	-	$1.67 \cdot 10^{-6} \pm 352.8 \cdot 10^{-9}$	$561.9 \cdot 10^{-9} \pm 50.2 \cdot 10^{-9}$

6.6 Mechanical Properties

6.6.1 Hardness Measurement and Nanoindentation

One beneficial mechanical property of ceramic coatings is their hardness, which is frequently utilized when required to increase the durability of materials in tribological applications. It has been demonstrated that the hardness of ceramic materials is determined by some intrinsic material properties such as grain size, porosity, purity and phase composition, and other experimental factors including applied load and temperature (McColm, 1990). If a polycrystalline ceramic is not evidently cracked during indentation hardness testing and if also the indentation area covers many grains, then the structural properties such as porosity and phase composition became the decisive factors for hardness evaluation.

The hardness and elastic modulus of thin coatings produced in phosphate-based electrolyte were measured by out-of-plane indentations on slightly polished surfaces, since it was difficult to apply indentations on cross-sections due to the porous structure of coating and its low thickness value. The hardness values measured on polished surface of thin coatings on CP-Ti and Ti6Al4V alloys are 4.01 ± 0.63 GPa and 4.29 ± 0.78 GPa, respectively. In addition, the elastic modulus values of the same coatings were calculated as 82.37 ± 8.47 GPa and 75.35 ± 8.40 GPa, respectively.

The hardness and elastic modulus values that were measured by in-plane indentations on the cross-sections of coatings formed in aluminate-based electrolytes and the hardness values that were measured by out-of-plane indentations on polished surfaces of the same coatings are shown in Figure 6.21 and Figure 6.22, respectively. In case of in-plane indentation, the coatings formed in aluminate-phosphate and aluminate-pyrophosphate electrolytes have generally lower hardness and elastic modulus than other coatings. In case of out-of-plane indentations, it has been observed that the hardness of coatings produced in aluminate-phosphate and aluminate-pyrophosphate electrolytes are decreased to lower values above a critical thickness of 30 μm from the substrate/coating interface, supporting the test results

obtained from in-plane indentations. The hardness and elastic modulus of coating produced in aluminate-tungstate electrolyte fluctuated considerably through the thickness and exhibited the highest value at a distance of 20 μm from the substrate/coating interface both for in-plane and out-of-plane indentations. The hardness and elastic modulus of coating produced in aluminate electrolyte are slightly changed through the thickness of coating.

The variation of hardness and elastic modulus can be attributed to the changes in porosity and relative amounts of phase contents through the thickness of coating. In case of thin coatings formed in phosphate-based electrolyte, the increased porosity in the coating structure resulted in lower hardness and elastic modulus values compared to thick coatings formed in aluminate-based electrolytes. The corundum found in the XRD patterns of some coatings formed in aluminate-based electrolytes may be another reason for increased hardness values, since corundum is much harder than aluminum titanium oxide and rutile. As seen in the XRD spectrum of polished coating produced in aluminate-tungstate electrolyte (Figure 6.14), the intensities of corundum peaks at angles of 35.1° and 43.3° (2θ) are increased at a distance of 20 μm from the substrate/coating interface, where the hardness value is also increased considerably. The decreased hardness of coatings formed in aluminate-phosphate and aluminate-pyrophosphate electrolytes, especially in the outer layers, may also be attributed to the decreased amount of corundum.

Since the hardness of coatings produced in aluminate-based electrolytes was increased at the inner layer of coating, the outer layers of these coatings were polished off to obtain a final thickness of about 25 μm. Then, the scratch and wear tests were applied on polished coatings, which are expected to have improved scratch and wear resistances owing to increased hardness values.

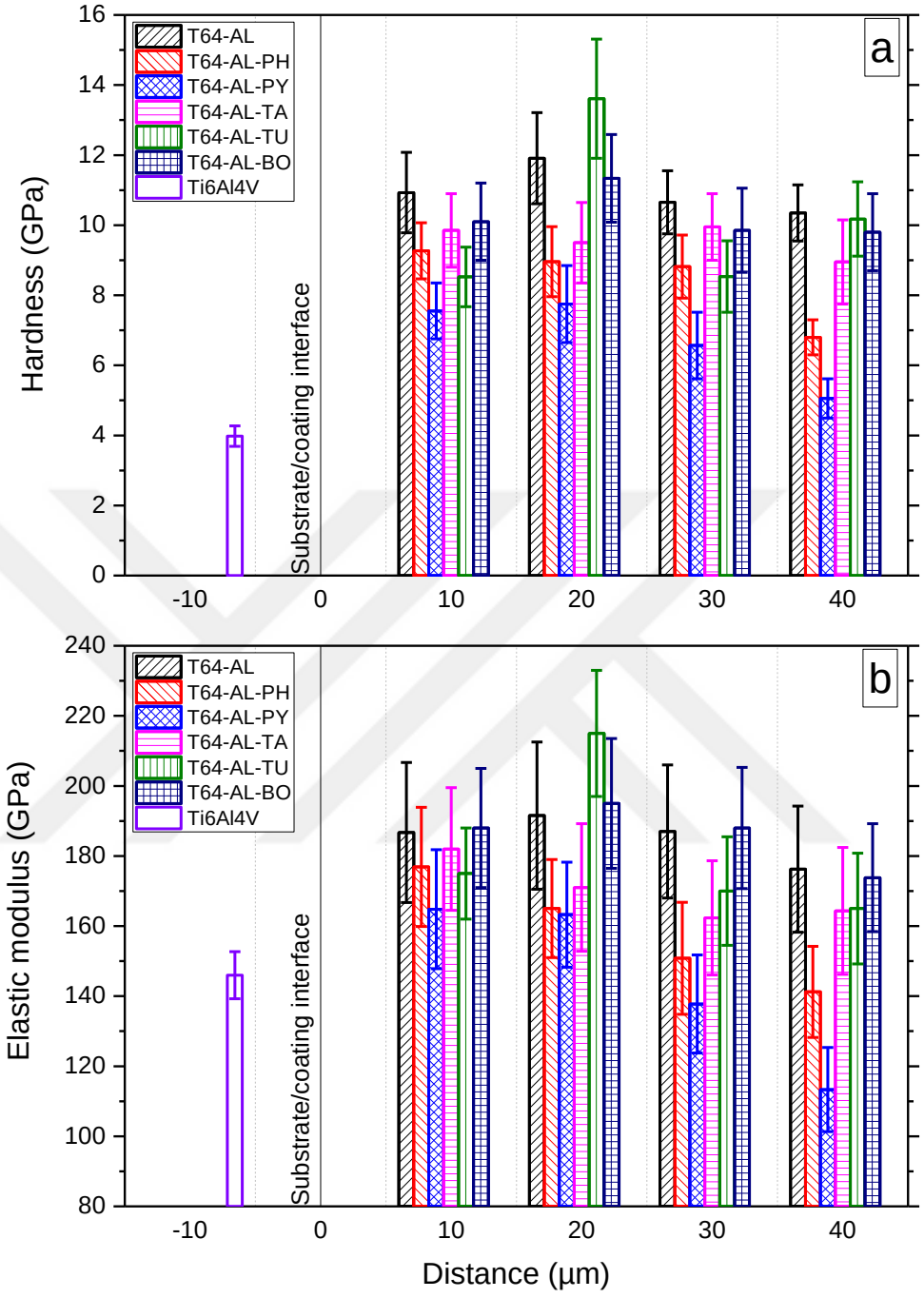


Figure 6.21 (a) The hardness and (b) elastic modulus values that were measured by in-plane indentations on cross-section of coatings produced in aluminate-based electrolytes

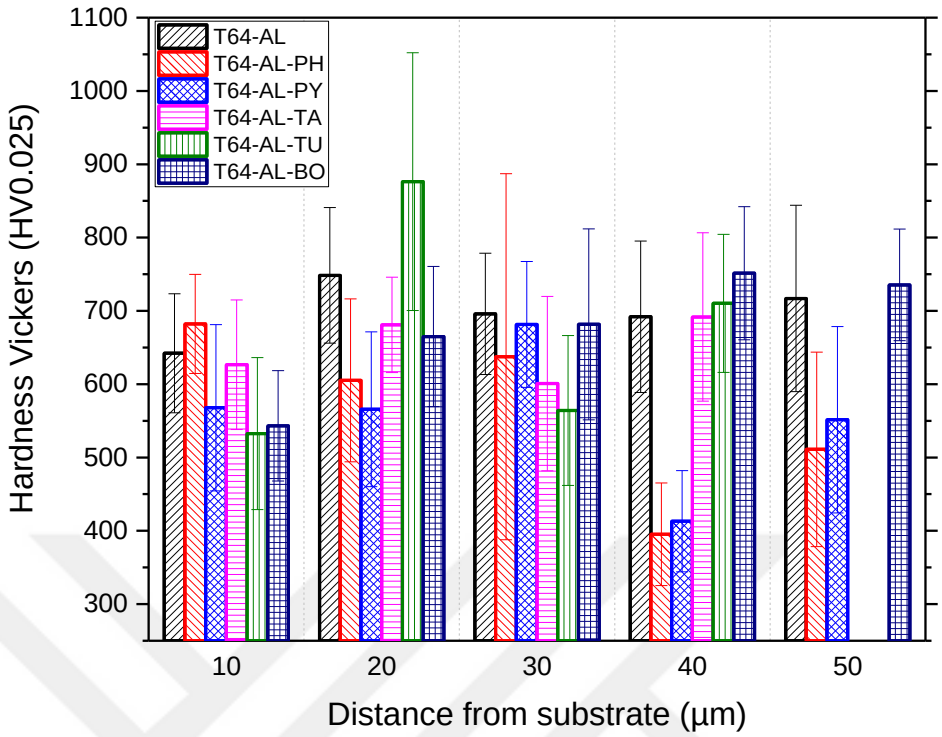


Figure 6.22 The Vickers hardness values that were measured by out-of-plane indentations on polished surfaces of coatings produced in aluminate based electrolytes

6.6.2 Scratch Test

In scratch test, the critical load value, at which a specific, well-defined, recognizable damage event occurs, is determined by analyzing the scratch tracks under optical microscope. The bright regions in the optical microscope images of scratch tracks are related to the spallation of coating. Since the cohesive damage events such as chipping and cracking are not clearly observed under optical microscope due to its limited resolution, SEM is utilized to study the cohesive damage events occurred during progressive loading. In addition to image analysis, supplementary data graphics including acoustic emission, penetration depth and friction coefficient are also used to determine the critical load values.

The optical microscope images of scratch tracks produced on coatings by progressive loading up to a maximum load of 30 N and the corresponding

supplementary data graphics are shown in Figure 6.23 through Figure 6.26. The coatings formed in phosphate-based electrolyte were broken off the surface at a certain distance, which is indicated as vertical lines in supplementary data graphics, but the coatings formed in aluminate-based electrolytes possessed only cohesive damage events such as cohesive chipping or cracking during progressive loading. Therefore, the critical load values namely L_{c1} and L_{c2} that are listed in Table 6.5 correspond to the normal load values where the first cohesive damage event and adhesive failure of coatings are observed, respectively. As is seen in Table 6.5, the coatings produced on CP-Ti and Ti6Al4V alloys using phosphate-based electrolyte showed much lower scratch resistance than those produced using aluminate-based electrolytes. The improved scratch resistance of coatings formed in aluminate-based electrolytes can be related to their enhanced load bearing capacity which is provided by increased thickness values. Since the micropores in the coating structure act as stress risers and initiate microcracks resulting in spallation of coating, the increased porosity of coatings formed in phosphate-based electrolyte may be another reason for their reduced scratch resistance. It is also observed that the friction modifier top-coat decreased the friction coefficient during scratch test and retarded the penetration of stylus deeper into the coating, thus, increased the critical load values of as-prepared coatings. As seen in Figure 6.27, the coatings formed in aluminate containing electrolytes remained on the surface up to a maximum load of 70 N. At some weak points where the adhesion of coating to the substrate is decreased, some coatings were broken off the surface leaving bright regions in the scratch track. However, a progressive damage such as gross spallation was not observed with increasing load.

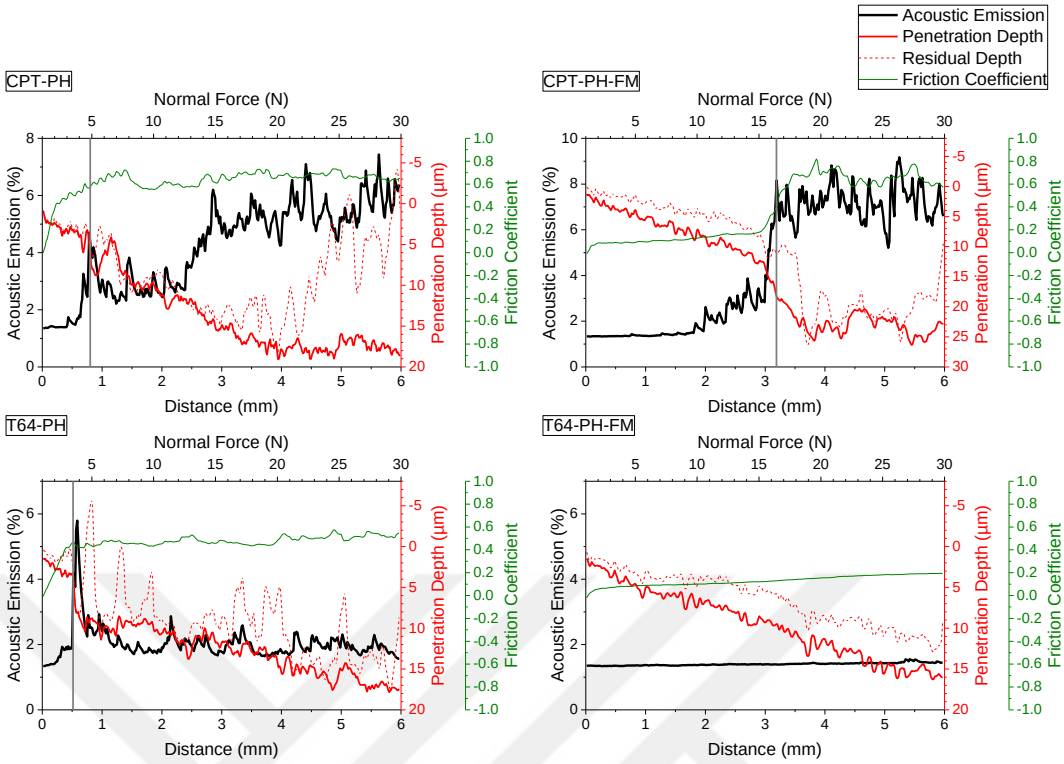


Figure 6.23 Supplementary data graphics which were obtained during scratch tests of coatings formed in phosphate-based electrolyte up to a maximum load of 30 N

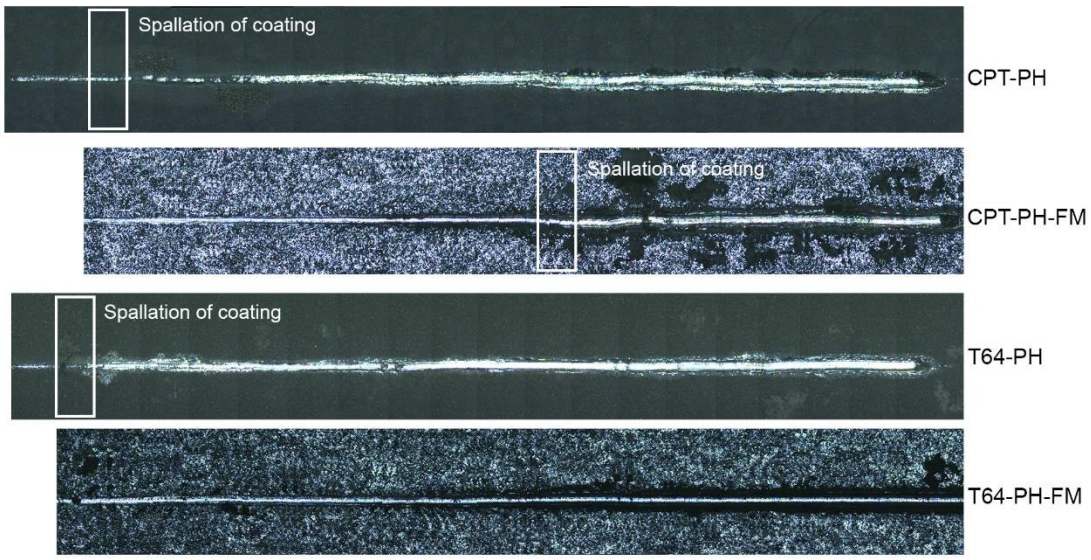


Figure 6.24 Optical microscope images of scratch tracks on coatings formed in phosphate electrolyte with and without top-coat. The maximum applied load and the scratch length are 30 N and 6 mm, respectively.

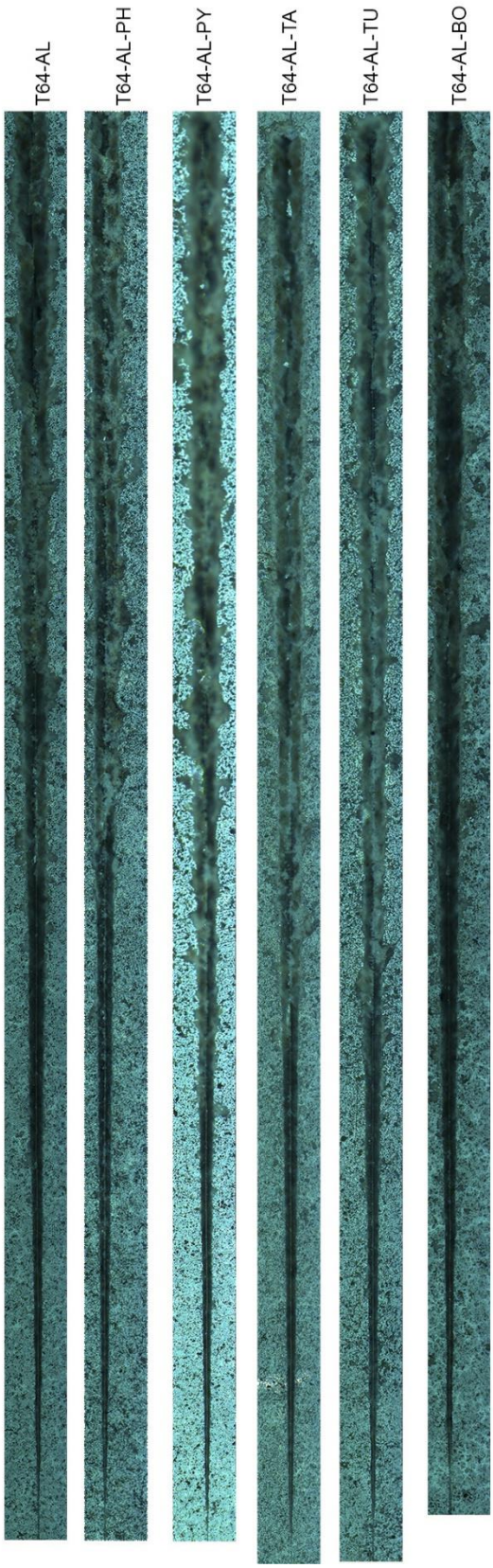


Figure 6.25 Optical microscope images of scratch tracks on polished coatings of 25 μm thickness. The maximum applied load and the scratch length are 30 N and 6 mm, respectively

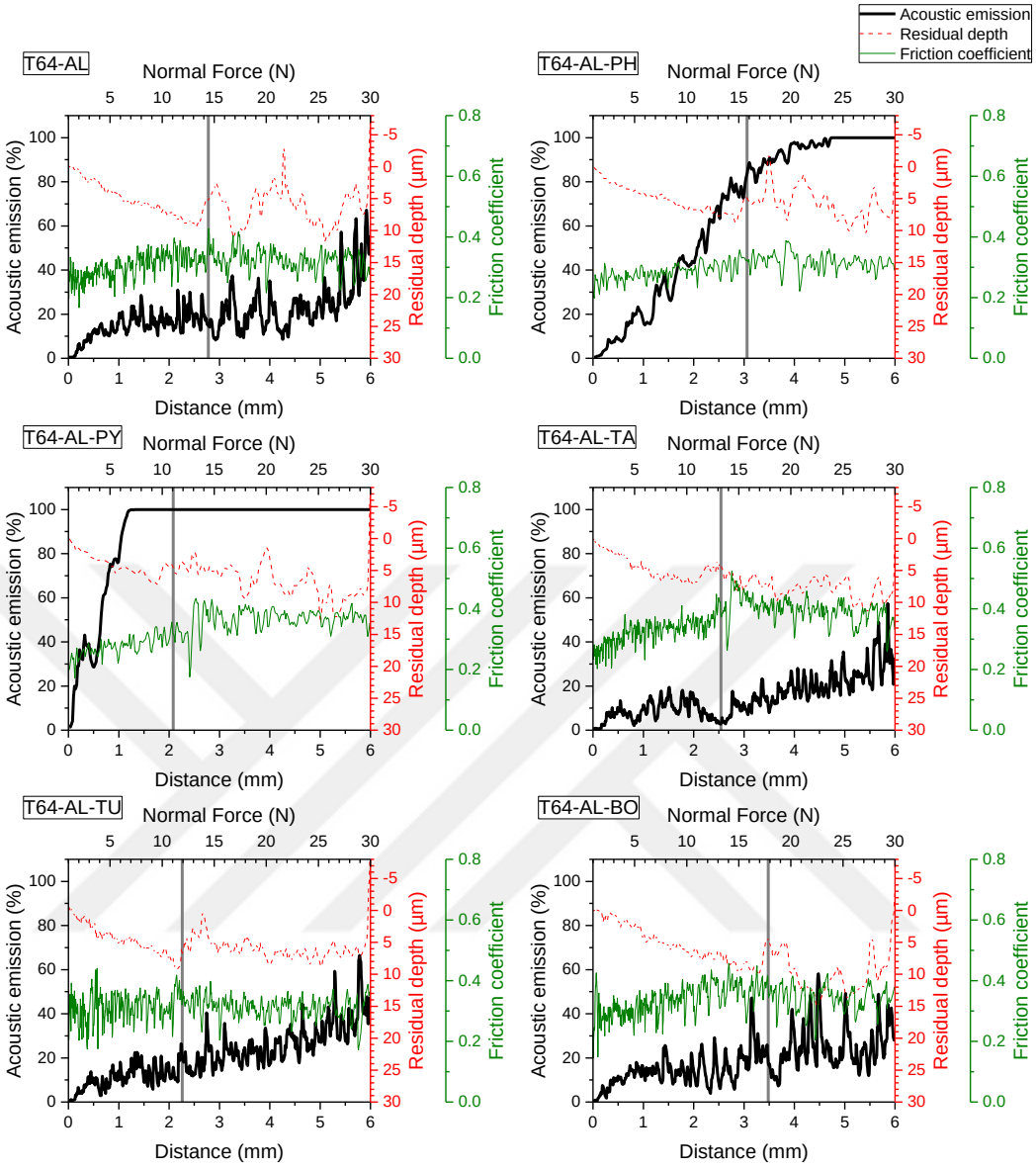


Figure 6.26 Supplementary data graphics which were obtained during scratch tests of polished coatings of 25 µm thickness formed in aluminate-based electrolytes up to a maximum load of 30 N

The scratch tracks were examined using SEM to reveal the failure mechanisms that were taken place during progressive loading. In case of the coatings formed on CP-Ti and Ti6Al4V alloys using phosphate-based electrolyte, large sections of detached coating within and extending beyond the scratch track were observed (Figure 6.28). Gross spallation of these coatings may indicate low adhesion strength or high residual stresses that were developed during PEO treatment. For CP-Ti alloy, the coating with top-coat was broken off the surface at a certain distance, but for Ti6Al4V alloy, MoS_2 top-coat remained within the scratch track throughout the

scratch test (Figure 6.28). As is seen in Figure 6.29, coating cracking along the scratch direction and cohesive chipping at the edges of scratch track were the two main failure mechanisms for all coatings produced using aluminate-based electrolytes. When the scratch tracks were formed by loading progressively up to a maximum load of 70 N, series of nested microcracks were observed within the scratch track, and cohesive chipping was seen at the edges of scratch track (Figure 6.30). These cohesive damage events are strongly depended on the degree of plastic deformation in the substrate and elastic properties of coating. During progressive loading, the tensile stresses behind the stylus result in through-thickness cracking in the coating, whereas the cohesive chipping is generally caused by the elastic recovery behind the stylus.

Table 6.5 Critical load values that indicate the first cohesive damage event (L_{c1}) and spallation of coating (L_{c2})

Coating	**L_{c1}* (N)**	**L_{c2}** (N)**
CPT-PH	-	4.9
CPT-PH-FM	-	16.3
T64-PH	-	3.5
T64-PH-FM	-	30<
T64-AL	13.9	70<
T64-AL-PH	15.3	70<
T64-AL-PY	10.4	70<
T64-AL-TA	12.7	70<
T64-AL-TU	11.3	70<
T64-AL-BO	17.4	70<

*L_{c1} : Critical load value at which the first cohesive failure within the coating is observed

**L_{c2} : Critical load value at which the adhesive failure is observed

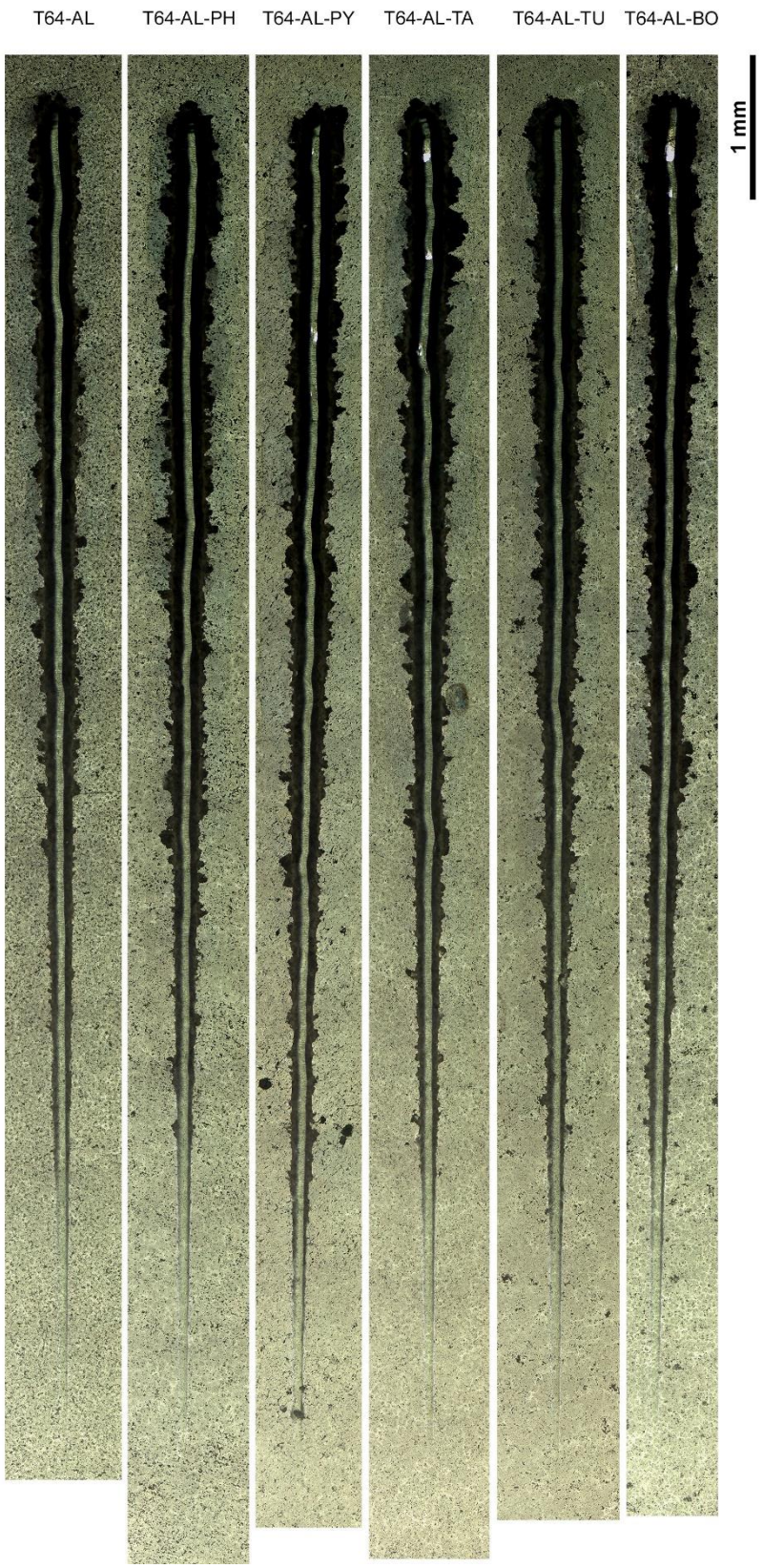


Figure 6.27 Optical microscope images of scratch tracks on polished coatings of 25 µm thickness. The maximum applied load and the scratch length are 70 N and 10 mm, respectively

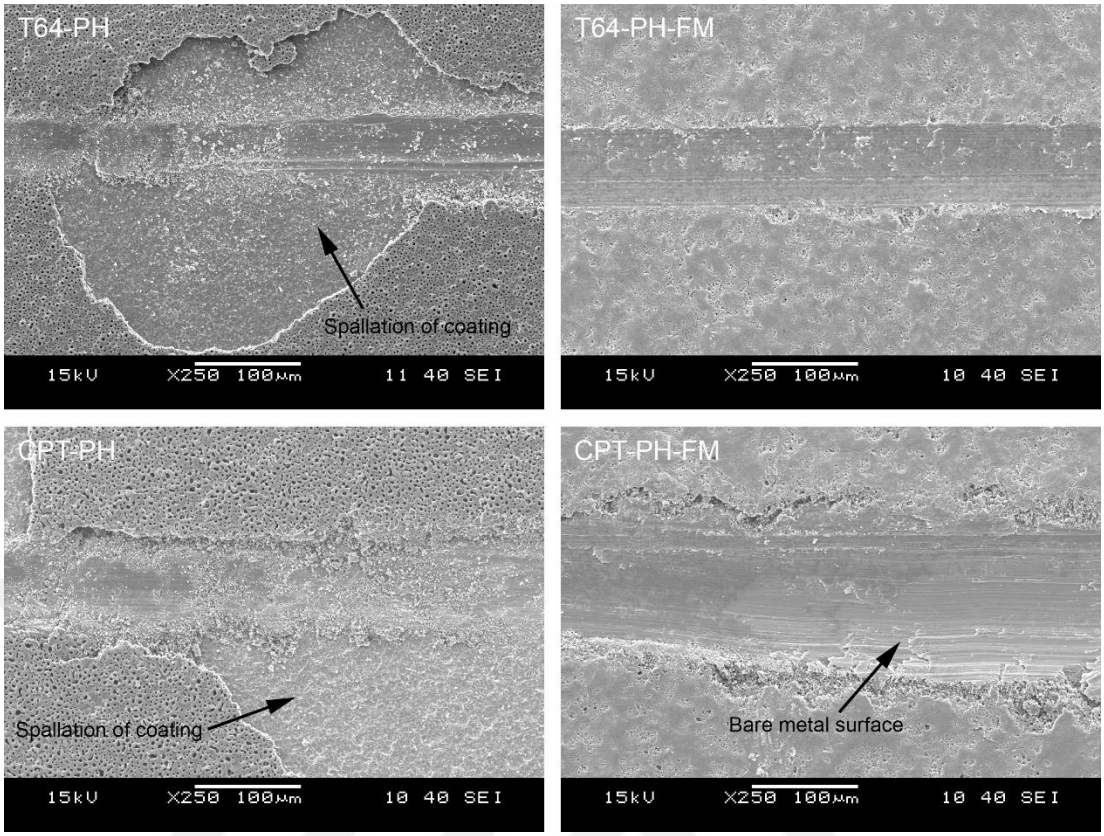


Figure 6.28 SEM images of scratch tracks that were formed using a maximum load of 30 N on the coatings which were formed in phosphate-based electrolyte

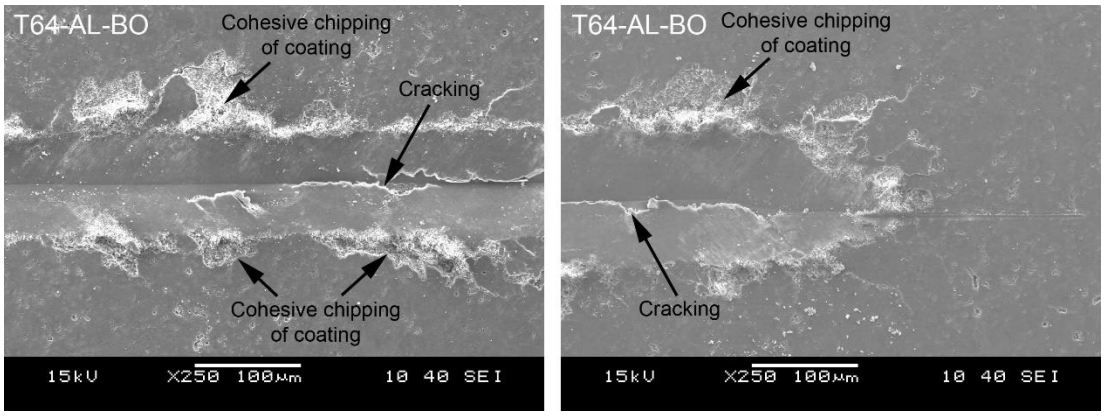


Figure 6.29 SEM images of scratch track that was formed using a maximum load of 30 N on the polished coating which was formed in aluminate-borate electrolyte. The image on the left hand-side represents the first cohesive damage event such as cracking or cohesive chipping, and the image on the right hand-side corresponds to the endpoint of scratch track

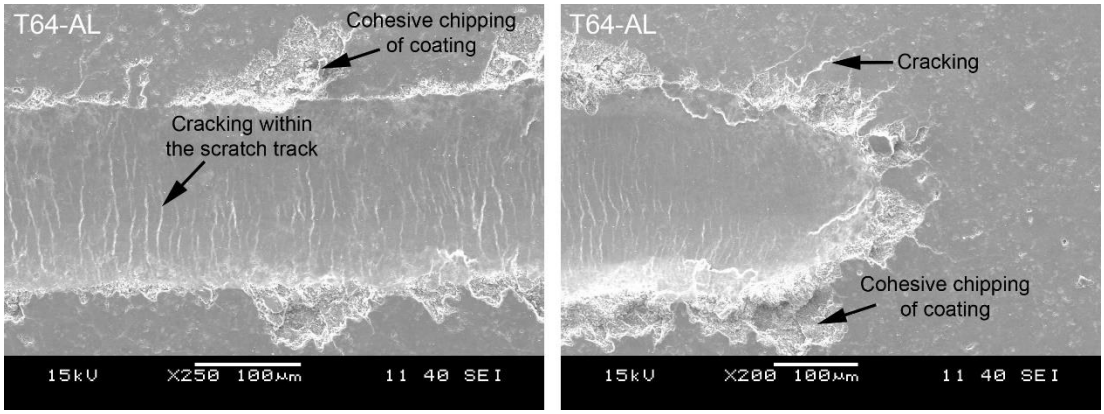


Figure 6.30 SEM images of scratch track that was formed using a maximum load of 70 N on the polished coating which was formed in aluminate electrolyte.

6.7 Tribological Properties

6.7.1 Wear Behavior

The wear rates and wear profiles of bare titanium alloys and PEO coatings formed in phosphate-based electrolyte are shown in Figure 6.31a and Figure 6.32, respectively. It has been observed that as-prepared PEO coatings both on CP-Ti and Ti6Al4V alloys were broken off the surface in the initial stages of sliding wear and the counter-face caused excessive wear damage in substrate alloy. As is seen in Figure 6.33, the friction coefficients of as-prepared coatings in phosphate-based electrolyte are almost the same with those of bare substrate alloys indicating that the coating was removed from the surface completely at the very beginning of wear test and a metal-to-metal contact was established between the steel and titanium alloy. The adhesive failure is most probably due to the decreased load bearing capacity of coating, which promoted the plastic deformation of substrate alloy during sliding wear, and eventually, caused brittle fracture of oxide coating. Unexpectedly, as-prepared PEO coatings both on CP-Ti and Ti6Al4V alloys showed slightly higher wear rates than bare substrate alloys. This is attributed to the progressive removal of hard particles from the coating surface during the sliding wear. After the coating was broken off the surface, these particles were entrapped at the substrate alloy/steel ball interface, causing three body abrasion of substrate material. Application of top-coat

on PEO coatings improved their wear resistance by decreasing the friction coefficient values below 0.16 (Figure 6.33).

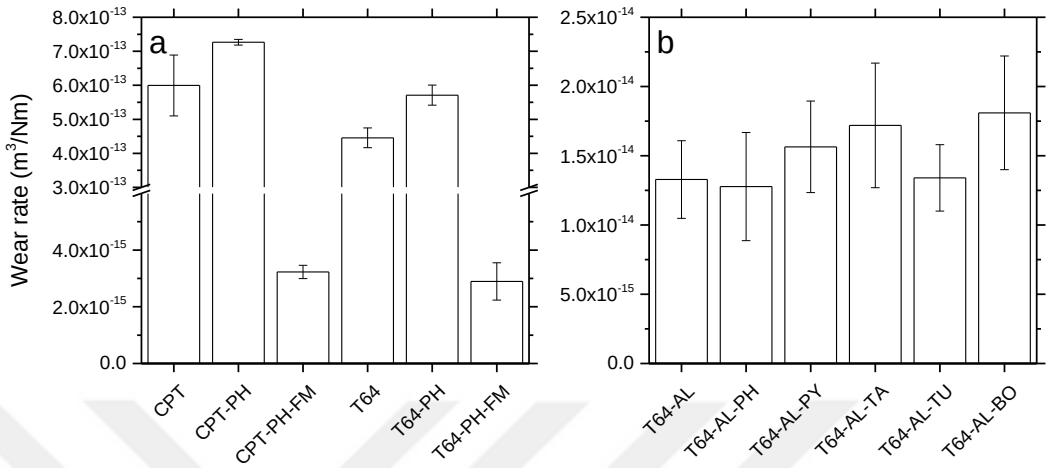


Figure 6.31 (a) Wear rates of coatings formed in phosphate-based electrolyte against AISI 52100 steel ball at an applied load of 10 N and (b) wear rates of AISI 52100 steel ball rubbed against polished coatings (25 μm) formed in aluminate-based electrolytes at an applied load of 10 N

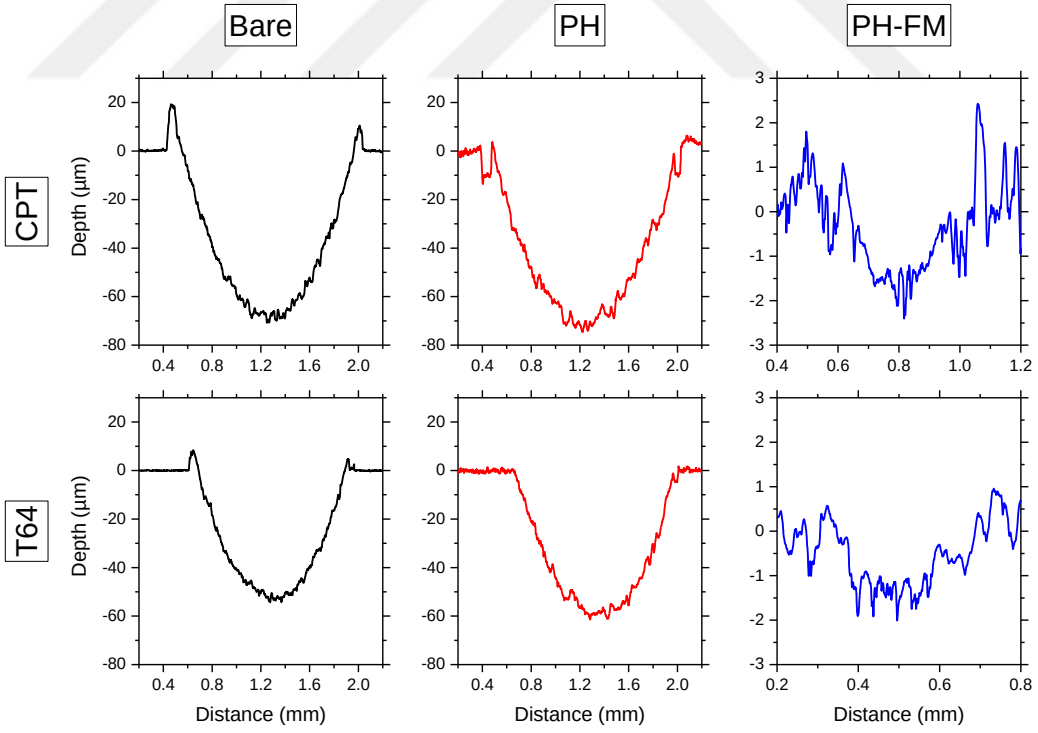


Figure 6.32 Wear profiles of coatings formed in phosphate-based electrolyte against AISI 52100 steel ball at an applied load of 10 N

When the coatings produced on Ti6Al4V alloy using aluminate-based electrolytes were rubbed against steel ball, significant amount of material was lost from the steel ball, then adhered on the coating surface. As is seen in Figure 6.34, the coefficient of friction rapidly increased in the initial period. After reaching to its maximum value, the friction coefficient decreased to lower values and slightly increased until the end of wear test, indicating that a stable tribofilm was formed on the coating surface. Since the wear track was covered with steel material, it was unlikely to obtain a wear groove, which is used to calculate the wear rate. Thus, the wear rate of steel ball was used to compare the wear resistance of coatings. The wear rates of steel balls, as shown in Figure 6.31b, have little change indicating that all coatings have nearly similar wear resistance when they were tested against steel ball. The increased wear resistance of coatings formed in aluminate-based electrolytes can be attributed to their high load bearing capacities.

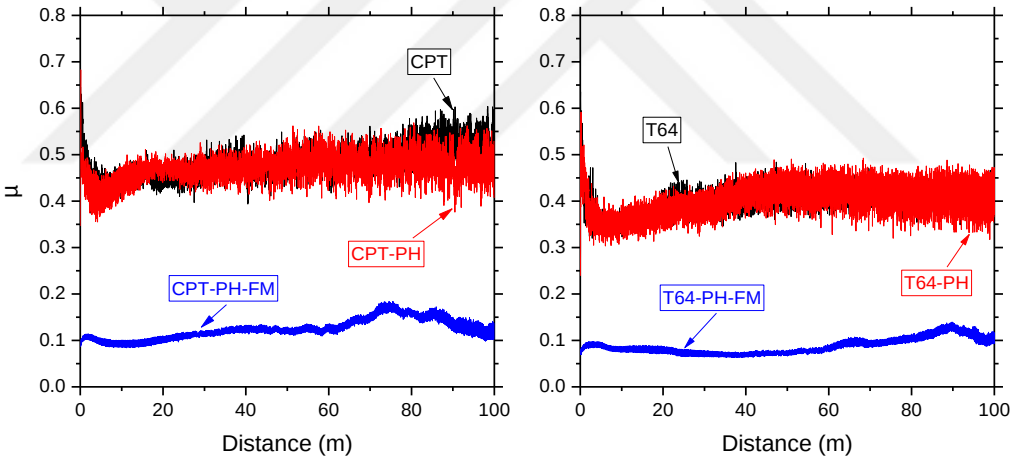


Figure 6.33 Friction coefficient of bare titanium alloys and coatings formed in phosphate-based electrolyte with and without top-coat against AISI 52100 steel ball at an applied load of 10 N

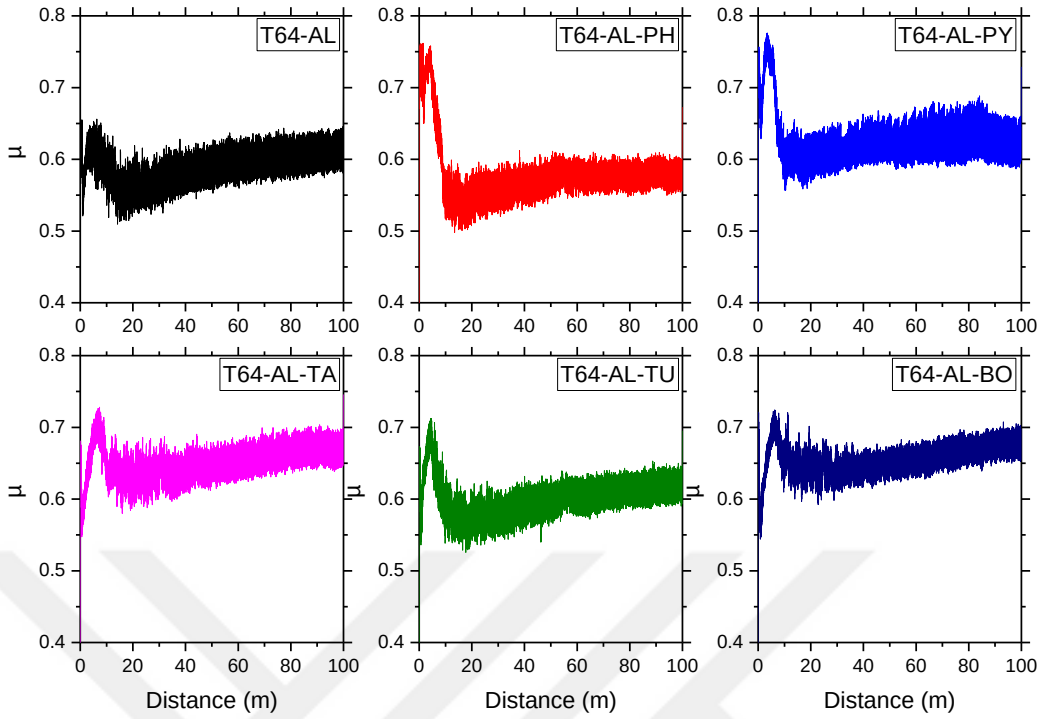


Figure 6.34 Friction coefficient of polished coatings (25 μm) formed in aluminate-based electrolytes against AISI 52100 steel ball at an applied load of 10 N

PEO coatings formed in aluminate-based electrolytes did not show a significant wear loss when tested against steel ball, furthermore, the steel material was adhered on the coating surface during sliding wear and made it hard to detect the wear loss in PEO coating. Thus, the wear performance of coatings formed in aluminate-based electrolytes were also evaluated using aluminum oxide ball, which is more abrasive than steel material. The wear rates and wear profiles of coatings rubbed against aluminum oxide ball are shown in Figure 6.35 and Figure 6.36, respectively. The critical load value at which the coating was removed from the substrate surface was used to rank the wear performance of coatings. At the minimum load of 1 N, all coatings remained on the substrate surface without adhesive failure, but, as is seen in the wear profiles, the aluminum oxide ball penetrated deeper into the coating formed in aluminate-phosphate electrolyte as compared with the other coatings. The coatings formed in aluminate-phosphate, aluminate-pyrophosphate and aluminate-borate electrolytes were completely removed from the surface at a normal load of 2 N, however, the coatings produced using aluminate and aluminate-tartrate electrolytes remained on the surface up to a critical load of 4 N. The coating formed in

aluminate-tungstate electrolyte broken off the surface at a normal load of 6 N, which is the highest critical load obtained in wear tests. The improvement in the tribological properties of some coatings is not only related to the increased hardness but also associated with the less porous structure as shown in cross-sectional SEM images (Figure 6.6). During the sliding wear test, the stress field generated within the coating and substrate by the reciprocating motion of the counter body may lead to subsurface microcracks. The nucleation of microcracks is more likely to take place predominantly from pores, because pores act as stress risers and cause high stress concentration, resulting in increased cracking along grain boundaries. As the counter body moves back and forth, the microcracks leads to the detachment of a fragment from the coating surface, leading to increased material loss and eventually adhesive failure of coating.

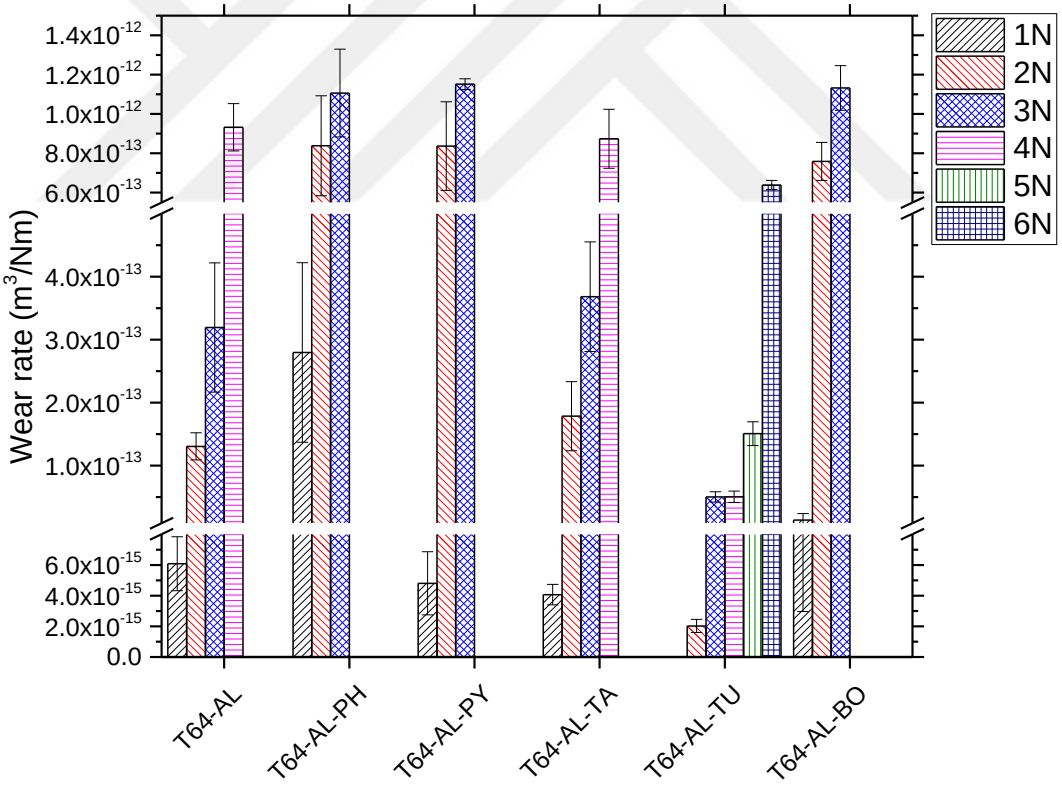


Figure 6.35 Wear rates of polished coatings (25 μm) formed in aluminate-based electrolytes against aluminum oxide ball

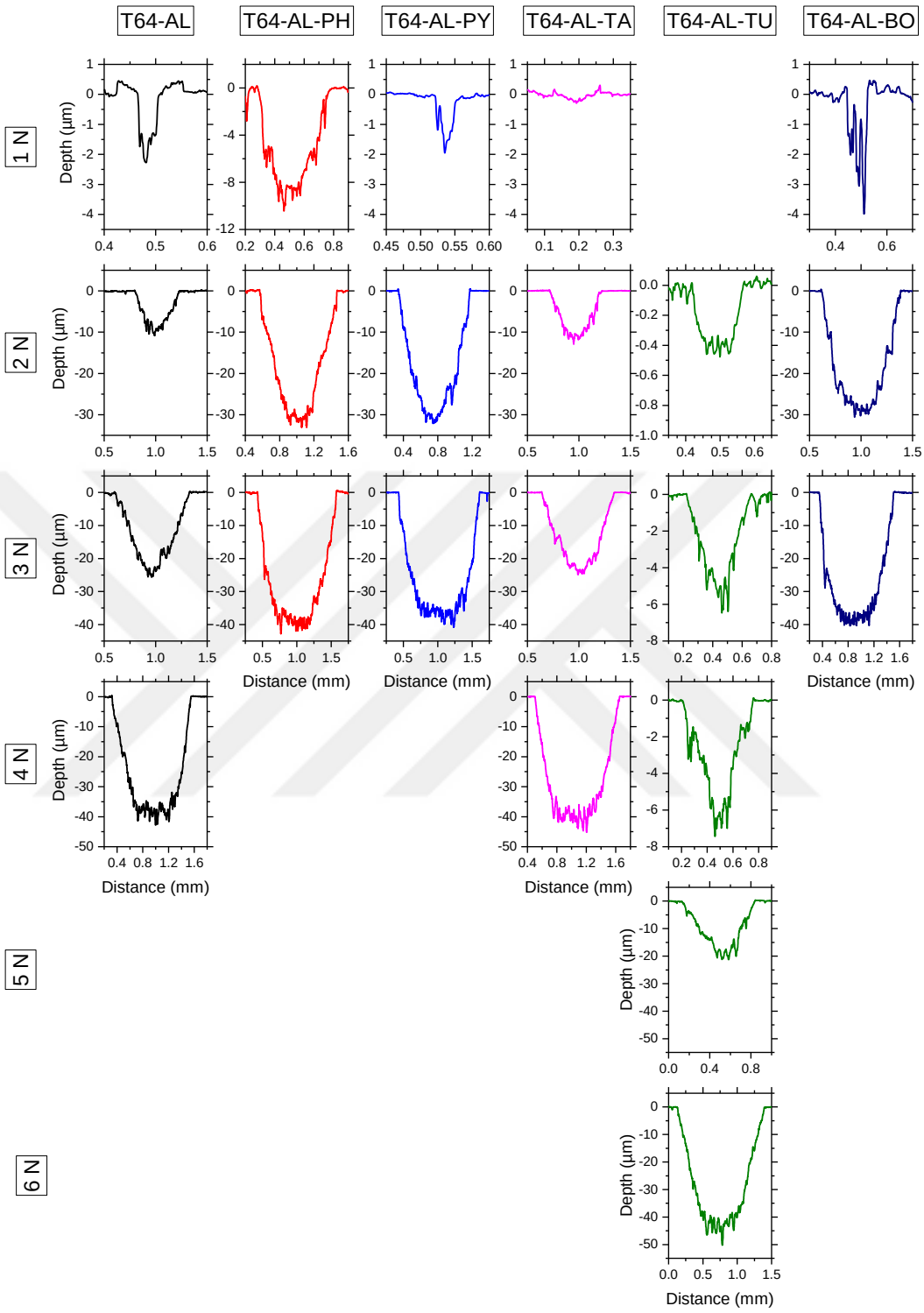


Figure 6.36 Wear profiles of polished coatings (25 µm) formed in aluminate-based electrolytes against aluminum oxide ball

6.7.2 Wear Mechanisms

The worn surfaces of coatings produced on Ti6Al4V using phosphate-based electrolyte with and without application of MoS_2 top-coat are shown in Figure 6.37. In case of the coating without top-coat, both abrasive and non-abrasive (adhesive) wear mechanisms were acting together during the sliding wear test against steel ball (Figure 6.37a and b). It was observed that the coating was removed from the surface in the initial period of sliding wear test by the applied shear stresses, which are extended to a specified depth value determined by the mechanical properties of both substrate and coating materials. After the removal of oxide layer, adhesive junctions were established at the asperities of two contacting metal surfaces, and following this, wear particles are produced by plastic tearing of adhesive junctions when the strength of junction or the pure strength of one of the metallic materials is exceeded depending on which is weaker. During repeated rubbing, these particles may be oxidized in presence of humidity, and may be also work-hardened by plastic deformation. Depending on the counter-faces and their motion, wear particles can roll over, become embedded to the counter-faces or pass through with little damage. Consequently, the abrasion of counter-face by hard wear particles resulted in fine parallel scratches and plastic tearing of ridges at the edges of the scratches, as seen in the detailed SEM image of wear track (Figure 6.37b). In case of the coating with top-coat, the solid lubricant layer remained within the wear track throughout the duration of wear test and protected the coating from excessive wear damage by decreasing the frictional forces. But, at some regions, the top-coat was partially removed from the surface and small-scale micropores were observed in these regions, as indicated in Figure 6.37c. The rod-shaped solid lubricant particles embedded into the binding resin can be easily seen in the detailed SEM image (Figure 6.37d). In addition, microcracks due to the applied compressive and shear stresses can be also observed in the wear track.

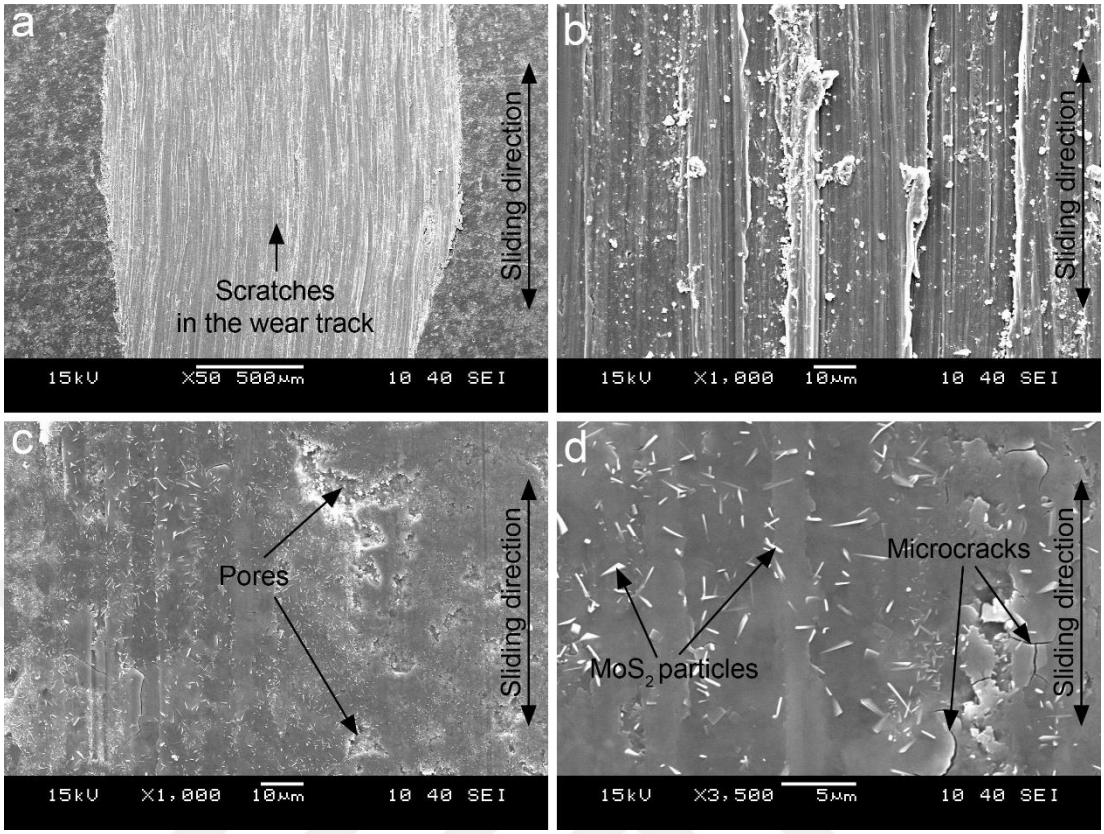


Figure 6.37 (a,b) Macro and detailed SEM images of worn coatings produced on Ti6Al4V using phosphate-based electrolyte without top-coat and (c,d) detailed SEM images of worn coatings produced on Ti6Al4V using phosphate-based electrolyte with MoS_2 top-coat

The SEM images of wear track on PEO coating produced on Ti6Al4V alloy using aluminate electrolyte is shown in Figure 6.38. It has been observed that the coating did not fail when rubbed against steel ball. In the running-in period, the material is transferred from the steel ball to the coating surface leading to formation of a stable tribofilm. After running-in period, the applied stresses brake off the tribofilm at some regions leaving a fragmented view as is seen in Figure 6.38b. It is suggested that abrasive wear of steel ball occurs in the initial period and then metal-to-metal contact is established causing micropolishing at the contact regions. The scratches on the flattened surface of steel ball is shown in Figure 6.39 to indicate the abrasive wear of steel ball.

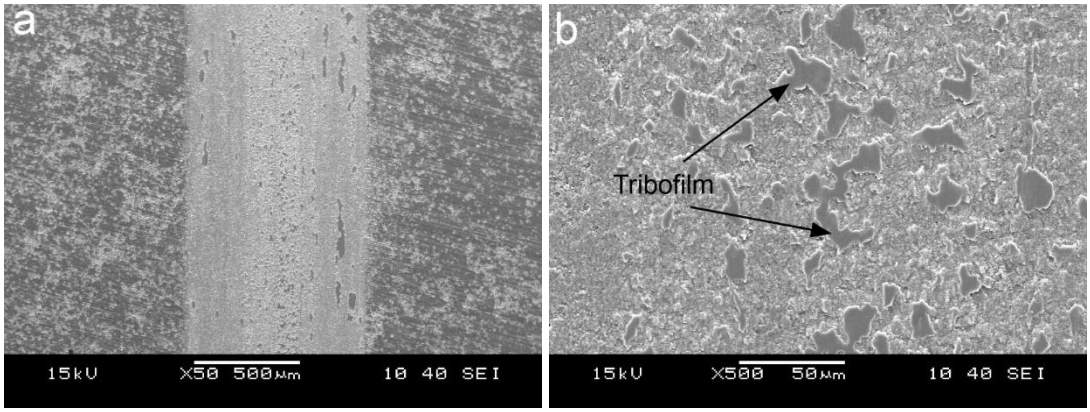


Figure 6.38 (a,b) Macro and detailed SEM images of wear track on polished coating (25 µm) produced on Ti6Al4V using aluminate electrolyte

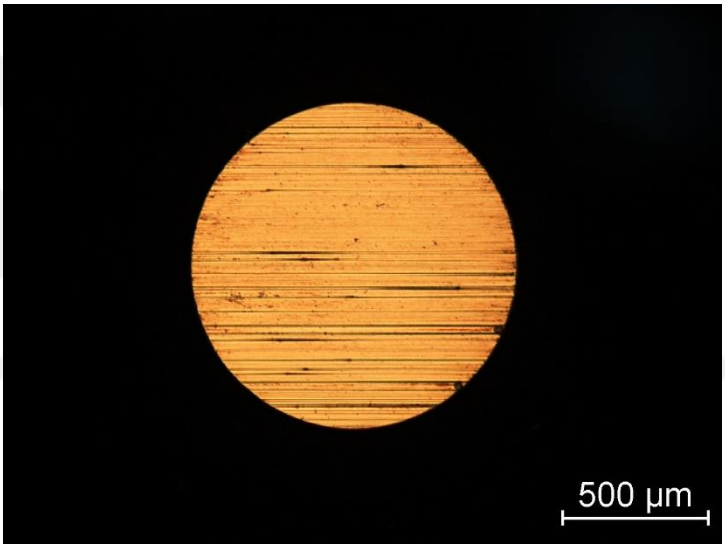


Figure 6.39 The optical microscope image of flattened surface of steel ball rubbed against PEO coating produced on Ti6Al4V using aluminate electrolyte

In case of the coating rubbed against alumina ball, adhesive failure of coating occurred at a critical load, after which the material loss was increased significantly due to the abrasion of titanium alloy. The wear tracks of coating that was produced using aluminate electrolyte are shown in Figure 6.40 through Figure 6.43 in order to investigate the wear mechanisms during the sliding wear test against alumina. At an applied load of 1 N, fatigue cracks due to repeated rubbing, and cohesive chipping of coating by two-body abrasion were observed (Figure 6.40). At an applied load of 2 N, the principal wear mechanism was micropolishing of surface, as shown in Figure 6.41a and b. During micropolishing, chipping of coating also occurred. At an applied

load of 3 N, the alumina ball deeply abraded the coating resulting in a rough surface which is covered with wear debris (Figure 6.42a). The lamellar structures of wear debris as seen in Figure 6.42b are possibly formed by cyclic loading, during which the wear particles are smeared on the surface, overlapped and then plastically deformed. At the critical load of 4 N, the coating was removed completely and the bare metal surface was abraded by alumina ball leading to scratches in the wear track (Figure 6.43a). After adhesive failure of coating, titanium metal transferred to the surface of alumina ball leaving traces of adhesive tearing on worn surface as seen in Figure 6.43b.

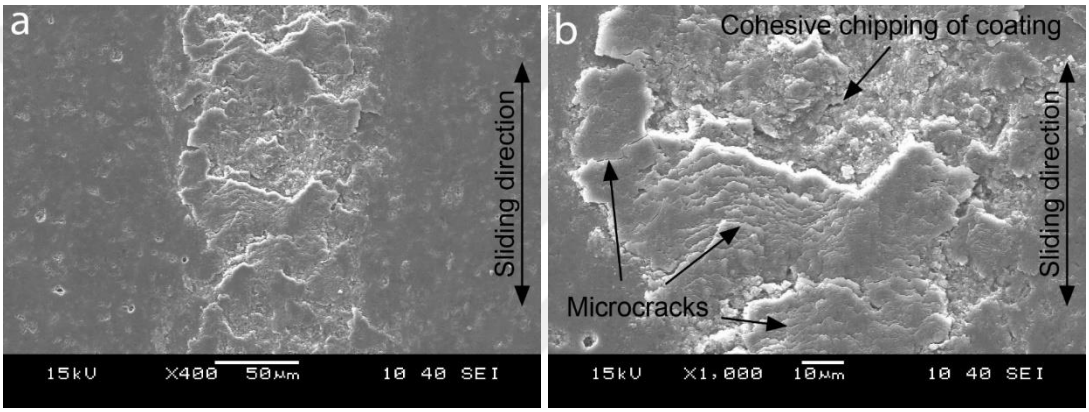


Figure 6.40 (a) Macro and (b) detailed SEM images of wear track obtained by applying 1 N normal load on polished coating (25 μm) formed in aluminate electrolyte

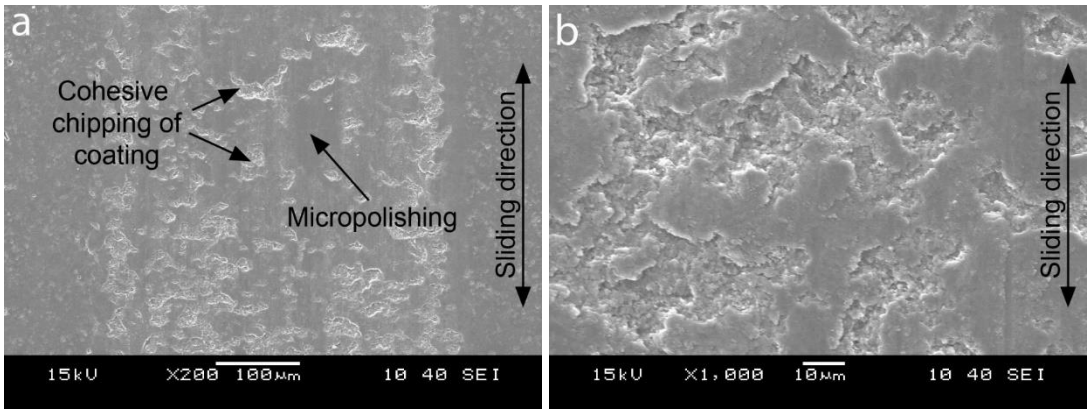


Figure 6.41 (a) Macro and (b) detailed SEM images of wear track obtained by applying 2 N normal load on polished coating (25 μm) formed in aluminate electrolyte

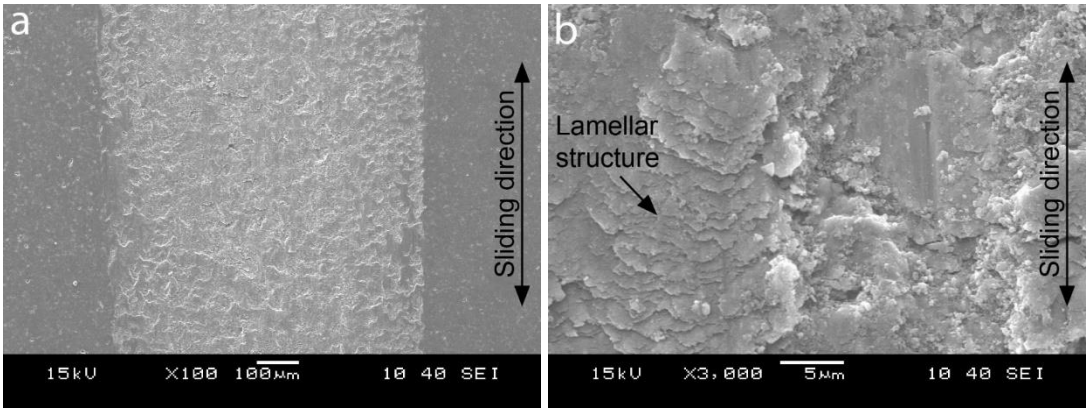


Figure 6.42 (a) Macro and (b) detailed SEM images of wear track obtained by applying 3 N normal load on polished coating (25 µm) formed in aluminate electrolyte

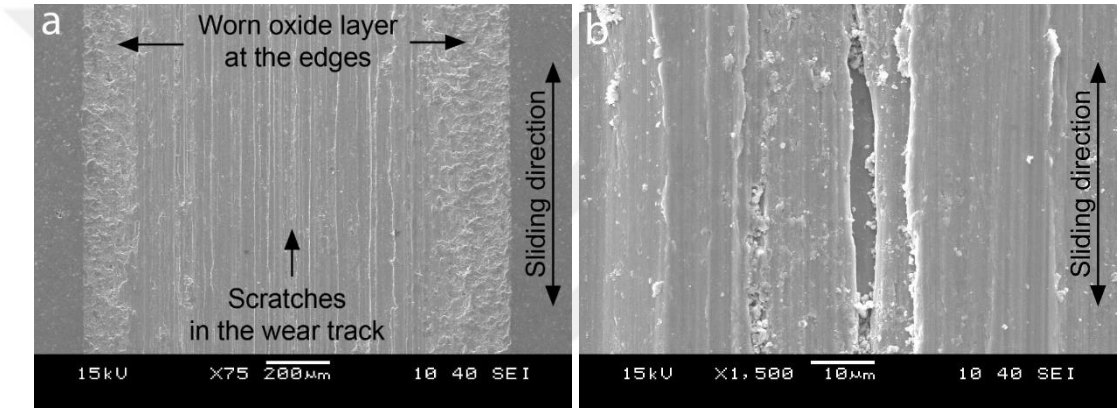


Figure 6.43 (a) Macro and (b) detailed SEM images of wear track obtained by applying 4 N normal load on polished coating (25 µm) formed in aluminate electrolyte

CHAPTER SEVEN
CONCLUSIONS

Structural Properties

The aluminate-based electrolytes allow thick coatings in the range of 45-60 μm to be produced on Ti6Al4V alloy by incorporating electrolyte species into the coating structure. But, the coatings that are formed in phosphate-based electrolyte have a limited thickness of about 10 μm, since the dissolution rate of titanium alloy equals to the deposition rate of oxide material after a certain time during PEO process.

The coatings produced using phosphate-based electrolyte are composed of rutile and anatase, indicating that the coating growth is assisted by the substrate oxidation. On the other hand, the coatings formed in aluminate-based electrolytes consist of aluminum titanium oxide, corundum and rutile. The incorporation of electrolyte species into the oxide layer during PEO processing in aluminate-based electrolytes results in the formation complex phase structures. While the rutile content is increased near the substrate/coating interface, the amount of corundum is increased towards the free surface of coating.

Addition of different chemicals into the aluminate electrolyte influences the microstructural properties of coatings in different ways. It has been shown that the phosphate and pyrophosphate additives suppress the formation of corundum during PEO processing and decreases the surface roughness of coatings. The aluminate and aluminate-tungstate electrolytes form less porous coating structures but increase the surface roughness values.

The surfaces of coatings are covered with numerous micropores, which represent the individual plasma discharges formed during PEO process. As the process duration is increased, the size of micropores become larger due to the formation of stronger and long-living microarcs. The surface morphology of thin coatings formed in phosphate-based electrolyte differs from that of thick coatings produced using

aluminate-based electrolytes. Thin coatings have only small-sized micropores on the surface, whereas thick coatings have bigger micropores with sintered particles, which are formed by the rapid solidification of molten oxide material that are erupted from discharge channels.

Electrochemical Corrosion Properties

The application of thin coatings using phosphate-based electrolyte decreases the corrosion rate of titanium alloys slightly, whereas thick coatings that are formed in aluminate-based electrolytes increased the corrosion rate of substrate alloys by a factor of about 2.5. The improvement in the corrosion resistance of thin coatings may be attributed to the barrier layer at the substrate/coating interface.

Further enhancement in the corrosion resistance of thin coating is achieved by silane treatment, which decreased the corrosion rate of coating by a factor of 18.

EIS test results suggests a two-layered structure with a top porous layer and a dense bottom layer. It has been observed that the application of thin coating on CP-Ti alloy using phosphate-based electrolyte increases the overall impedance of substrate alloy by a factor of about 30. The PEO coating with silane treatment has the highest impedance value of about 18 Mohms.

Mechanical Properties

The hardness and elastic modulus of coatings formed in phosphate-based electrolyte are in the ranges of 3.5-5 GPa and 65-90 GPa, respectively. On the other hand, depending on the electrolyte composition, the hardness and elastic modulus of coatings formed in aluminate-based electrolytes are in the ranges of 5-14 GPa and 100-230 GPa, respectively.

The critical load values of coatings produced on CP-Ti and Ti6Al4V alloys using phosphate-based electrolyte are 4.9 N and 3.5 N, respectively. The application of

MoS_2 top-coat increased the critical load values considerably. The coating on CP-Ti with top-coat has a critical load value of 16.3 N, whereas the critical load of coating on Ti6Al4V with top-coat is higher than 30 N. In case of the coatings formed in aluminate-based electrolytes, the critical load values are higher than 70 N. The improvement in the scratch resistance is attributed to the high load bearing capacity of thick coatings formed in aluminate-based electrolytes.

Tribological Properties

The thin coatings that are formed in phosphate-based electrolyte broken off the surface when tested against steel ball at a normal load of 10 N, causing excessive wear damage in titanium alloy. The application of friction modifier MoS_2 on the coating surface decreases the friction coefficient below 0.2 and protects the coating from adhesive failure. When the steel ball rubbed against thick coatings formed in aluminate-based electrolytes, significant amount of material lost from the steel ball and adhered on the coating surface, while there is no evidence for coating removal.

The thick coatings formed in aluminate-based electrolytes are removed from the substrate surface completely at a certain load when tested against aluminum oxide ball. The coatings produced using aluminate-phosphate, aluminate-pyrophosphate and aluminate-borate have the lowest critical load of 2 N, whereas the coating produced in aluminate and aluminate tartrate electrolytes show a crtical load of 4 N. However, the highest critical load of 6 N is obtained when the coating is formed in aluminate-tungstate electrolyte. It is shown that the wear resistance of coatings is generally increased by the increasing amount of corundum in their structure. Beside this, the decreased porosity also improves the cohesive strength within the coating, leading to further enhancement in wear resistance.

The abrasive wear of steel ball is occurred when it is rubbed against thick coatings formed in aluminate-based electrolytes. When the coatings formed in aluminate-based electrolytes are tested against aluminum oxide ball, different wear mechanisms including micropolishing, microcracking and cohesive chipping are observed before

the critical load value, after which the coating is removed completely causing abrasion of titanium alloy.

Future Works

It has been found that the most promising electrolytes for obtaining hard and thick coatings on titanium alloys are composed of aluminates. The combination of high load bearing capacity and increased hardness value improves the mechanical and tribological properties of coatings that are formed in aluminate containing electrolytes. In order to increase the hardness of coating and improve its wear resistance, hard nanoparticles made of corundum can be incorporated into the coating structure through the field-assisted deposition during PEO processing.

The corrosion resistance of PEO coatings is strongly affected by the phase components and porosity, as well as the chemical properties of surface such as surface tension and hydrophobicity. Since the corrosive species in the solution penetrates into the coating via micropores, different post-treatments can be utilized to seal the pores and cracks, and hence increase the electrochemical corrosion resistance. In addition to sodium chloride solution, the electrochemical corrosion tests can be carried out in acidic solutions at high temperatures to study the effect of environmental conditions on the electrochemical behavior of coatings.

It is known that the parts made of titanium alloys such as bushing, bolt and nut undergo small fluctuations at the contact area by vibration or some other forces. The minute relative motion under load may result in fretting wear damage under working conditions. Thus, the fretting wear of coatings on titanium alloys can also be studied.

REFERENCES

Albella, J. M., Montero, I. & Martínez-Duart, J. M. (1984). Electron injection and avalanche during the anodic oxidation of tantalum. *Journal of The Electrochemical Society, 131* (5), 1101-1104.

Albella, J. M., Montero, I., Fernandez, M., Gomez-Aleixandre, C. & Martínez-Duart, J. M. (1985). Double anodization experiments in tantalum. *Electrochimica Acta, 30* (10), 1361-1364.

Albella, J. M., Montero, I. & Martinez-Duart, J. M. (1987). A theory of avalanche breakdown during anodic oxidation. *Electrochimica Acta, 32* (2), 255-258.

Aliasghari, S., Skeldon, P. & Thompson, G. E. (2014). Plasma electrolytic oxidation of titanium in a phosphate/silicate electrolyte and tribological performance of the coatings. *Applied Surface Science, 316*, 463-476.

Arrabal, R., Matykina, E., Hashimoto, T., Skeldon, P. & Thompson, G. E. (2009). Characterization of ac peo coatings on magnesium alloys. *Surface and Coatings Technology, 203* (16), 2207-2220.

Babaei, M., Dehghanian, C. & Vanaki, M. (2015). Effect of additive on electrochemical corrosion properties of plasma electrolytic oxidation coatings formed on cp ti under different processing frequency. *Applied Surface Science, 357, Part A*, 712-720.

Belevantsev, V. I., Markov, G. A., Terleeva, O. P. & Shulepko, E. K. (1989). Model of transition from anodization to microarc stage. *Izvestiya Sibirskogo Otdeleniya Akademii Nauk Sssr Seriya Khimicheskikh Nauk, 3* (6), 73-80.

Belevantsev, V. I., Terleeva, O. P., Markov, G. A., Shulepko, E. K., Slonova, A. I. & Utkin, V. V. (1998). Micro-plasma electrochemical processes. *Protection of Metals, 34* (5), 469-484.

Bhushan, B. (2013). *Introduction to tribology* (2nd ed.). United Kingdom: Wiley.

Brennan, J. B. & Leona, M. (1944). *Corrosion resistant coating*. United States Patent no: 2346658.

Briant, C. L., Wang, Z. F. & Chollocoop, N. (2002). Hydrogen embrittlement of commercial purity titanium. *Corrosion Science, 44* (8), 1875-1888.

Brown, B. F. (1972). *Stress-corrosion cracking in high strength steels and in titanium and aluminum alloys*. Accession Number: (ADA030783). Retrieved August, 4, 2016 from http://www.dtic.mil/dtic/tr/fulltext/u2/740749.pdf.

Brown, S. D., Kuna, K. J. & Van, T. B. (1971). Anodic spark deposition from aqueous solutions of naalo2 and na2sio3. *Journal of The American Ceramic Society, 54* (8), 384-390.

Buckley, D. H. (1965). *Influence of crystal orientation on friction characteristics of titanium single crystals in vacuum*. Document Number: (NASA-TN-D-2988). National Aeronautics and Space Administration. Retrieved August, 4, 2016 from http://ntrs.nasa.gov/archive/nasa/casi.ntrs.nasa.gov/19650023044.pdf.

Buckley, D. H. & Johnson, R. L. (1966). Friction and wear of hexagonal metals and alloys as related to crystal structure and lattice parameters in vacuum. *A S L E Transactions, 9* (2), 121-135.

Buckley, D. H. (1967). Friction characteristics in vacuum of single and polycrystalline aluminum oxide in contact with themselves and with various metals. *A S L E Transactions, 10* (2), 134-145.

Buckley, D. H. (1968). The influence of the atomic nature of crystalline materials on friction. *A S L E Transactions, 11* (2), 89-100.

Buckley, D. H. (1977). International conference on colloids and surfaces the metal-to-metal interface and its effect on adhesion and friction. *Journal of Colloid and Interface Science, 58* (1), 36-53.

Budinski, K. G. (1991). Tribological properties of titanium alloys. *Wear, 151* (2), 203-217.

Burns, J. R. (1967). *Lubrication of titanium 'state of the art'*. Accession Number: (AD0652001). DTIC Document. Retrieved August, 4, 2016 from http://www.dtic.mil/dtic/tr/fulltext/u2/652001.pdf.

Caprani, A. & Frayret, J. P. (1979). Behaviour of titanium in concentrated hydrochloric acid: Dissolution-passivation mechanism. *Electrochimica Acta, 24* (8), 835-842.

Ceschini, L., Lanzoni, E., Martini, C., Prandstraller, D. & Sambogna, G. (2008). Comparison of dry sliding friction and wear of ti6al4v alloy treated by plasma electrolytic oxidation and pvd coating. *Wear, 264* (1–2), 86-95.

Cheng, Y.-l., Wu, X.-Q., Xue, Z.-g., Matykina, E., Skeldon, P. & Thompson, G. E. (2013). Microstructure, corrosion and wear performance of plasma electrolytic oxidation coatings formed on ti–6al–4v alloy in silicate-hexametaphosphate electrolyte. *Surface and Coatings Technology, 217*, 129-139.

Cheng, Y., Wu, F., Matykina, E., Skeldon, P. & Thompson, G. E. (2012). The influences of microdischarge types and silicate on the morphologies and phase compositions of plasma electrolytic oxidation coatings on zircaloy-2. *Corrosion Science, 59*, 307-315.

Di Quarto, F., Piazza, S. & Sunseri, C. (1988). Electrical and mechanical breakdown of anodic films on tungsten in aqueous electrolytes11part of this work was presented at the “giornate della elettrochimica italiana” held in bologna, 28–30 october 1986. *Journal of Electroanalytical Chemistry and Interfacial Electrochemistry, 248* (1), 99-115.

Di, S., Guo, Y., Lv, H., Yu, J. & Li, Z. (2015). Microstructure and properties of rare earth ceo2-doped tio2 nanostructured composite coatings through micro-arc oxidation. *Ceramics International, 41* (5, Part A), 6178-6186.

Dittrich, K. H., Krysmann, W., Kurze, P. & Schneider, H. G. (1984). Structure and properties of anof layers. *Crystal Research and Technology, 19* (1), 93-99.

Donachie, M. J. (2000). Corrosion resistance. In *Titanium: A technical guide* (2nd ed.) (123-130). United States of America: ASM International.

Dunleavy, C. S., Golosnoy, I. O., Curran, J. A. & Clyne, T. W. (2009). Characterisation of discharge events during plasma electrolytic oxidation. *Surface and Coatings Technology, 203* (22), 3410-3419.

Dunleavy, C. S., Curran, J. A. & Clyne, T. W. (2013). Time dependent statistics of plasma discharge parameters during bulk ac plasma electrolytic oxidation of aluminium. *Applied Surface Science, 268*, 397-409.

Dwyer, R. J. (1955). *Method of increasing emissivity of tantalum*. United States Patent no: 2720488.

Evangelides, H. A. (1955). *Method of electrolytically coating magnesium and electrolyte therefor*. United States Patent no: 2723952.

Fei, C., Hai, Z., Chen, C. & Yangjian, X. (2009). Study on the tribological performance of ceramic coatings on titanium alloy surfaces obtained through microarc oxidation. *Progress in Organic Coatings, 64* (2–3), 264-267.

Finsterwalder Isolations GmbH (1954). *Improved process for the electrolytic oxidizing of aluminium or aluminium alloys* Patent no: GB717015.

Furey, M. J. (1966). The action of iodine in producing extremely low friction. *Wear, 9* (5), 369-387.

Gnedenkov, S. V., Sinebryukhov, S. L., Skorobogatova, T. M. & Gordienko, P. S. (1998). Properties of coatings formed on titanium by microarc oxidation in hypophosphite-aluminate electrolytes. *Russian Journal of Electrochemistry, 34* (9), 1046-1051.

Gnedenkov, S. V., Sinebryukhov, S. L. & Sergienko, V. I. (2006). Electrochemical impedance simulation of a metal oxide heterostructure/electrolyte interface: A review. *Russian Journal of Electrochemistry, 42* (3), 197-211.

Gordienko, P. S., Nedozorov, P. M., Zavidnaya, A. G. & Yarovaya, T. P. (1991). The elements composition of anodic films on nbtsu alloy obtained at sparking potentials in aqueous electrolytes. *Elektronnaya Obrabotka Materialov* (1), 38-41.

Griess, J. C. (1968). Crevice corrosion of titanium in aqueous salt solutions. *Corrosion, 24* (4), 96-109.

Gruss, L. & Mackus, T. (1973). The anodic oxidation of several rare earth metals in sodium aluminate solution. *Journal of The Electrochemical Society, 120* (3), 337-340.

Güntherschulze, A. & Betz, H. (1932). Neue untersuchungen über die elektrolytische ventilwirkung. *Zeitschrift für Physik, 78* (3-4), 196-210.

Güntherschulze, A. & Betz, H. (1937). Untersuchungen über die funken der elektrolytischen ventilwirkung. *Zeitschrift für Physik, 107* (5-6), 347-353.

Habazaki, H., Tsunekawa, S., Tsuji, E. & Nakayama, T. (2012). Formation and characterization of wear-resistant peo coatings formed on β-titanium alloy at different electrolyte temperatures. *Applied Surface Science, 259*, 711-718.

Hokkirigawa, K., Kato, K. & Li, Z. Z. (1988). The effect of hardness on the transition of the abrasive wear mechanism of steels. *Wear, 123* (2), 241-251.

Hradcovsky, R. & Bayles, S. (1974). *Process for forming a coating comprising a silicate on valve group metals*. United States Patent no: 3832293.

Hradcovsky, R. (1978). *Process for forming a silicate coating on metal*. United States Patent no: 4082626.

Hradcovsky, R. (1987). *Method of coating articles of aluminum and an electrolytic bath therefor*. United States Patent no: 4659440.

Hradcovsky, R. J. & Bayles Jr., H. S. (1976). *Coated valve metal article formed by spark anodizing*. United States Patent no: 3956080.

Hussein, R. O., Nie, X. & Northwood, D. O. (2010). Influence of process parameters on electrolytic plasma discharging behaviour and aluminum oxide coating microstructure. *Surface and Coatings Technology, 205* (6), 1659-1667.

Hussein, R. O., Nie, X. & Northwood, D. O. (2013). An investigation of ceramic coating growth mechanisms in plasma electrolytic oxidation (peo) processing. *Electrochimica Acta, 112* (0), 111-119.

Hutchings, I. M. (1992). *Tribology: Friction and wear of engineering materials*: Edward Arnold.

Ikonopisov, S. (1977). Theory of electrical breakdown during formation of barrier anodic films. *Electrochimica Acta, 22* (10), 1077-1082.

Ikonopisov, S. & Elenkov, N. (1978). Interfacial control of the electronic current through the barrier-type anodic films in contact with an electrolyte. *Journal of Electroanalytical Chemistry and Interfacial Electrochemistry, 86* (1), 105-114.

Jovovic, J., Stojadinovic, S., Sisovic, N. M. & Konjevic, N. (2011). Spectroscopic characterization of plasma during electrolytic oxidation (peo) of aluminium. *Surface & Coatings Technology, 206* (1), 24-28.

Jovović, J., Stojadinović, S., Šišović, N. M. & Konjević, N. (2012). Spectroscopic study of plasma during electrolytic oxidation of magnesium- and aluminium-alloy. *Journal of Quantitative Spectroscopy and Radiative Transfer, 113* (15), 1928-1937.

Karanik, Y. A., Markov, G. A., Minin, V. F., Nikolaev, A. V. & Peshchevitskij, B. I. (1977). *Metal mould making method* Patent no: SU582894.

Kharitonov, D. Y., Gutsevich, E. I., Novikov, G. I. & Fridman, A. A. (1988). On mechanism of pulsed electrolytic spark oxidation in saturated sulfuric acid. *TsNIIAtomInform*.

Khruschov, M. M. (1974). Principles of abrasive wear. *Wear, 28* (1), 69-88.

Klapkiv, M. D., Nykyforchyn, H. M. & Posuvailo, V. M. (1995). Spectral analysis of an electrolytic plasma in the process of synthesis of aluminum oxide. *Materials Science, 30* (3), 333-343.

Klapkiv, M. D. (1996). State of an electrolytic plasma in the process of synthesis of oxides based on aluminum. *Materials Science, 31* (4), 494-499.

Klapkiv, M. D. (1999). Simulation of synthesis of oxide-ceramic coatings in discharge channels of a metal-electrolyte system. *Materials Science, 35* (2), 279-283.

Kostman, S. J. (1968). Lubricants and wear coatings for titanium. In Conrad, H., Jaffee, R., Kessler, H. & Minkler, W. (Eds.). *Applications related phenomena in titanium alloys* (268-282). Pennsylvania: American Society For Testing And Materials (ASTM).

Krisanfova, O. A., Volkova, L. M., Gnedenkov, S. V., Kaidalova, T. A. & Gordienko, P. S. (1995). Synthesis of chemical-compounds films on titanium surface under microplasma discharges. *Russian Journal of Inorganic Chemistry (Zurnal Neorganiceskoj Himii), 40* (4), 558-562.

Kurze, P., Krysmann, W. & Marx, G. (1980). *Verfahren zur erzeugung alpha-al2o3 -haltiger schichten auf aluminiummetallen* Patent no: DD142360.

Kurze, P., Marx, G., Krysmann, W. & Dittrich, K.-H. (1982). *Verfahren zur oberflächenbehandlung von titanium und -legierungen* Patent no: DD156003.

Kurze, P., Krysmann, W. & Schneider, H. G. (1986). Application fields of anof layers and composites. *Crystal Research and Technology, 21* (12), 1603-1609.

Kurze, P., Krysmann, W., Schreckenbach, J., Schwarz, T. & Rabending, K. (1987). Colored anof layers on aluminum. *Crystal Research and Technology, 22* (1), 53-58.

Li, X.-J., Cheng, G.-A., Xue, W.-B., Zheng, R.-T. & Cheng, Y.-J. (2008). Wear and corrosion resistant coatings formed by microarc oxidation on tial alloy. *Materials Chemistry and Physics, 107* (1), 148-152.

Long, H. D. K. (1959). *Anodizing magnesium*. United States Patent no: 2901409.

Malyshev, V. N., Bulychev, S. I., Markov, G. A., Fyedorov, V. A., Petrosyants, A. A., Kudinov, V. V. & Shorshorov, M. H. (1985). Physico-mechanical characteristics and wear resistance of coatings deposited by the method of microarc oxidation. *Fiz. Khim. Obrab. Mater.* (1), 82-87.

Markov, G. A. & Markova, G. V. (1976). *A method of forming anodes of electrolytic condensers*. USSR Patent no: SU00526961A1.

Markov, G. A., Tatarchuk, V. V. & Mironova, M. K. (1983). Microarc oxidation of aluminum in the concentrated sulfuric-acid. *Izvestiya Sibirskogo Otdeleniya Akademii Nauk Sssr Seriya Khimicheskikh Nauk, 3* (7), 34-37.

Markov, G. A., Belevantsev, V. I. & Terleeva, O. P. (1988). Wear resistance of coatings deposited by anodic-cathodic microarc method. *Friction and Wear, 9* (2), 286-290.

Markov, G. A., Belevantsev, V. I., Slonova, A. I. & Terleeva, O. P. (1989). Step-wise character of anodic-cathodic microplasma processes. *Russian Journal of Electrochemistry, 25* (11), 1473-1479.

Markov, G. A., Shulepko, E. K. & Terleeva, O. P. (1989). *Method of coating metals and alloys*. USSR Patent no: SU01200591A1.

Markov, G. A., Shulepko, E. K., Terleeva, O. P. & Slonova, A. I. (1994). Effect of microarc oxidation conditions on the uniformity of coating thickness on aluminum. *Russian Journal of Electrochemistry, 30* (1), 22-25.

Markov, G. A. & Shulepko, E. K. (1995). The current regimes and onset of the microarc stage of oxidation. *Protection of Metals, 31* (6), 643-647.

Markov, G. A., Slonova, A. I. & Terleeva, O. P. (1997). The chemical-composition, structure, and morphology of microplasma coatings *Protection of Metals, 33* (3), 289-294.

Martini, C., Ceschini, L., Tarterini, F., Paillard, J. M. & Curran, J. A. (2010). Peo layers obtained from mixed aluminate–phosphate baths on ti–6al–4v: Dry sliding behaviour and influence of a ptfe topcoat. *Wear, 269* (11–12), 747-756.

Matykina, E., Berkani, A., Skeldon, P. & Thompson, G. E. (2007). Real-time imaging of coating growth during plasma electrolytic oxidation of titanium. *Electrochimica Acta, 53* (4), 1987-1994.

Matykina, E., Arrabal, R., Mohedano, M., Pardo, A., Merino, M. C. & Rivero, E. (2013). Stability of plasma electrolytic oxidation coating on titanium in artificial saliva. *Journal of Materials Science: Materials in Medicine, 24* (1), 37-51.

McColm, I. J. (1990). Introduction and overview. In *Ceramic hardness* (1-31). New York: Springer Science Business Media.

McNeill, W. (1958). The preparation of cadmium niobate by an anodic spark reaction. *Journal of The Electrochemical Society, 105* (9), 544-547.

Mcneill, W. & Nordblom, G. F. (1958). *Method of making cadmium niobate*. United States Patent no: 2854390.

McNeill, W., Gruss, L. L. & Husted, D. G. (1965). The anodic synthesis of cds films. *Journal of The Electrochemical Society, 112* (7), 713-715.

Mcneill, W. & Gruss, L. L. (1966). *Anodic spark reaction processes and articles*. United States Patent no: 3293158.

Mercer, A. P. & Hutchings, I. M. (1988). The influence of atmospheric composition on the abrasive wear of titanium and ti-6al-4v. *Wear, 124* (2), 165-176.

Miller, P. D. & Holladay, J. W. (1958). Friction and wear properties of titanium. *Wear, 2* (2), 133-140.

Miyoshi, K. & Buckley, D. H. (1982). Adhesion and friction of transition metals in contact with non-metallic hard materials. *Wear, 77* (2), 253-264.

Nikolaev, A. V., Markov, G. A. & Peshchevitskii, B. I. (1977). A new phenomenon electrolysis. *Izvestiya Sibirskogo Otdeleniya Akademii Nauk Sssr Seriya Khimicheskikh Nauk, 5* (12), 32-33.

Oliver, W. C. & Pharr, G. M. (1992). An improved technique for determining hardness and elastic modulus using load and displacement sensing indentation experiments. *Journal of Materials Research, 7* (06), 1564-1583.

Orazem, M. E. & Tribollet, B. (2008). *Electrochemical impedance spectroscopy*. New Jersey: John Wiley & Sons, Inc.

PAR application note *Application note: Basics of electrochemical impedance spectroscopy*. (n.d.). Document Number: (AC-1). Retrieved August, 4, 2016 from http://www.princetonappliedresearch.com/download.asbx?AttributeFileId=8406b254-b6d4-4341-9f48-87a04ce7ee3d.

Phillips, I. I., Poole, P. & Shreir, L. L. (1974). Hydride formation during cathodic polarization of ti—ii. Effect of temperature and ph of solution on hydride growth. *Corrosion Science, 14* (9), 533-542.

Qin, Y., Xiong, D. & Li, J. (2015). Tribological properties of laser surface textured and plasma electrolytic oxidation duplex-treated ti6al4v alloy deposited with mos2 film. *Surface and Coatings Technology*, *269*, 266-272.

Quintero, D., Galvis, O., Calderón, J. A., Gómez, M. A., Castaño, J. G., Echeverría, F. & Habazaki, H. (2015). Control of the physical properties of anodic coatings obtained by plasma electrolytic oxidation on ti6al4v alloy. *Surface and Coatings Technology, 283,* 210-222.

Rabinowicz, E. (1995). *Friction and wear of materials* (2nd ed.). New York: Wiley.

Roberts, R. W. & Owens, R. S. (1963a). Boundary lubrication of titanium-titanium and titanium-steel. *Wear, 6* (6), 444-456.

Roberts, R. W. & Owens, R. S. (1963b). Titanium lubrication. *Nature, 200* (4904), 357-358.

Rudnev, V. S., Gordienko, P. S., Kurnosova, A. G. & Ovsyannikova, A. A. (1991). Influence of electrolyte on result of microarc oxide coating of aluminum alloys. *Protection of Metals (English translation of Zaschita Metallov)* (1), 106-110.

Sarbishei, S., Faghihi Sani, M. A. & Mohammadi, M. R. (2016). Effects of alumina nanoparticles concentration on microstructure and corrosion behavior of coatings formed on titanium substrate via peo process. *Ceramics International, 42* (7), 8789-8797.

Satoh, H., Shimogori, K. & Kamikubo, F. (1987). The crevice corrosion resistance of some titanium materials: A review of the beneficial effects of palladium. *Platinum Metals Review, 31* (3), 115-121.

Schutz, R. W. & Grauman, J. S. (1986). Fundamental corrosion characterization of high-strength titanium alloys. In *Industrial applications of titanium and zirconium: Fourth volume, astm stp 917* (130-143). Philadelphia: American Society for Testing and Materials.

Schutz, R. W. (1996). Ruthenium enhanced titanium alloys. *Platinum Metals Review, 40* (2), 54-61.

Schutz, R. W. (2005). Corrosion of titanium and titanium alloys. In *Asm handbook volume 13b: Corrosion: Materials* (252-299). United States of America: ASM International.

Shokouhfar, M., Dehghanian, C. & Baradaran, A. (2011). Preparation of ceramic coating on ti substrate by plasma electrolytic oxidation in different electrolytes and evaluation of its corrosion resistance. *Applied Surface Science, 257* (7), 2617-2624.

Shokouhfar, M., Dehghanian, C., Montazeri, M. & Baradaran, A. (2012). Preparation of ceramic coating on ti substrate by plasma electrolytic oxidation in different electrolytes and evaluation of its corrosion resistance: Part ii. *Applied Surface Science, 258* (7), 2416-2423.

Sikorski, M. E. (1964). The adhesion of metals and factors that influence it. *Wear, 7* (2), 144-162.

Simbi, D. J. & Scully, J. C. (1995). The effect of iron and three interstitial elements on the stress corrosion cracking of titanium in sea water. *Corrosion Science, 37* (8), 1325-1330.

Singh, V. B. & Hosseini, S. M. A. (1993). The electrochemical and corrosion behaviour of titanium and its alloy (vt-9) in phosphoric acid. *Corrosion Science, 34* (10), 1723-1732.

Slonova, A. I., Terleeva, O. P., Shulepko, E. K. & Markov, G. A. (1992). Aspects of the formation of microarc coatings. *Soviet Electrochemistry, 28* (9), 1280-1285.

Slonova, A. I., Terleeva, O. P. & Markov, G. A. (1997). Significance of silicate electrolyte-composition in anodic-cathodic microarc processes. *Protection of Metals, 33* (2), 208-212.

Snezhko, L. A., Papanova, I. I., Tikhaya, L. S. & Tchernenko, V. I. (1990). Growth of aluminum-oxide in solutions of sodium-silicate in the range of prebreakthrough voltages. *Protection of Metals, 26* (6), 998-1002.

Snezhko, L. A., Tikhaya, L. S., Udovenko, Y. E. & Tchernenko, V. I. (1991). Anodic spark deposition of silicates with ac. *Protection of Metals, 27* (3), 425-430.

Stojadinović, S., Jovović, J., Petković, M., Vasilić, R. & Konjević, N. (2011). Spectroscopic and real-time imaging investigation of tantalum plasma electrolytic oxidation (peo). *Surface and Coatings Technology, 205* (23–24), 5406-5413.

Stojadinović, S., Vasilić, R., Petković, M. & Zeković, L. (2011). Plasma electrolytic oxidation of titanium in heteropolytungstate acids. *Surface and Coatings Technology, 206* (2–3), 575-581.

Sundararajan, G. & Rama Krishna, L. (2003). Mechanisms underlying the formation of thick alumina coatings through the mao coating technology. *Surface and Coatings Technology, 167* (2-3), 269-277.

Tait, W. S. (1994). *An introduction to electrochemical corrosion testing for practicing engineers and scientists*. Wisconsin: PairODocs Publications.

Takamura, A. (1967). Corrosion resistance of ti and a ti-pd alloy in hot, concentrated sodium chloride solutions. *Corrosion, 23* (10), 306-313.

Tsunekawa, S., Aoki, Y. & Habazaki, H. (2011). Two-step plasma electrolytic oxidation of ti–15v–3al–3cr–3sn for wear-resistant and adhesive coating. *Surface and Coatings Technology, 205* (19), 4732-4740.

Van, T. B., Brown, S. D. & Wirtz, G. P. (1977). Mechanism of anodic spark deposition. *American Ceramic Society Bulletin, 56* (6), 563-566.

Venkateswarlu, K., Rameshbabu, N., Sreekanth, D., Bose, A. C., Muthupandi, V., Babu, N. K. & Subramanian, S. (2012). Role of electrolyte additives on in-vitro electrochemical behavior of micro arc oxidized titania films on cp ti. *Applied Surface Science, 258* (18), 6853-6863.

Vijh, A. K. (1971). Sparking voltages and side reactions during anodization of valve metals in terms of electron tunnelling. *Corrosion Science, 11* (6), 411-417.

Von Hippel, A. (1937). Electric breakdown of solid and liquid insulators. *Journal of Applied Physics, 8* (12), 815-832.

Wang, Y., Lei, T., Jiang, B. & Guo, L. (2004). Growth, microstructure and mechanical properties of microarc oxidation coatings on titanium alloy in phosphate-containing solution. *Applied Surface Science, 233* (1–4), 258-267.

Wang, Y. M., Jia, D. C., Guo, L. X., Lei, T. Q. & Jiang, B. L. (2005). Effect of discharge pulsating on microarc oxidation coatings formed on ti6al4v alloy. *Materials Chemistry and Physics, 90* (1), 128-133.

Wang, Y. M., Jiang, B. L., Guo, L. X. & Lei, T. Q. (2006). Tribological behavior of microarc oxidation coatings formed on titanium alloys against steel in dry and solid lubrication sliding. *Applied Surface Science, 252* (8), 2989-2998.

Wang, Y. M., Jiang, B. L., Lei, T. Q. & Guo, L. X. (2006). Microarc oxidation coatings formed on ti6al4v in na2sio3 system solution: Microstructure, mechanical and tribological properties. *Surface and Coatings Technology, 201* (1–2), 82-89.

Welsch, G., Boyer, R. & Collings, E. W. (1993). Technical note 2: Corrosion. In *Materials properties handbook: Titanium alloys* (1065-1077). United States of America: ASM International.

Wheeler, J. M., Collier, C. A., Paillard, J. M. & Curran, J. A. (2010). Evaluation of micromechanical behaviour of plasma electrolytic oxidation (peo) coatings on ti–6al–4v. *Surface and Coatings Technology*, *204* (21–22), 3399-3409.

Williams, D. N., Koehl, B. G. & Bartlett, E. S. (1969). The reaction of titanium with hydrogen gas at ambient temperatures. *Journal of The Less Common Metals, 19* (4), 385-398.

Wood, G. C. & Pearson, C. (1967). Dielectric breakdown of anodic oxide films on valve metals. *Corrosion Science, 7* (2), 119-125.

Xue, W., Wang, C., Chen, R. & Deng, Z. (2002). Structure and properties characterization of ceramic coatings produced on ti–6al–4v alloy by microarc oxidation in aluminate solution. *Materials Letters, 52* (6), 435-441.

Yarovaya, T. P., P.S., G., Rudnev, V. S., Nedozorov, P. M. & Zavidnaya, A. G. (1994). Thin-films containing transition element oxides - electrochemical synthesis at valve metal-surfaces. *Russian Journal of Electrochemistry, 30* (11), 1395-1396.

Yerokhin, A. L., Nie, X., Leyland, A., Matthews, A. & Dowey, S. J. (1999). Plasma electrolysis for surface engineering. *Surface & Coatings Technology, 122* (2-3), 73-93.

Yerokhin, A. L., Nie, X., Leyland, A. & Matthews, A. (2000). Characterisation of oxide films produced by plasma electrolytic oxidation of a ti–6al–4v alloy. *Surface and Coatings Technology, 130* (2–3), 195-206.

Yerokhin, A. L., Leyland, A. & Matthews, A. (2002). Kinetic aspects of aluminium titanate layer formation on titanium alloys by plasma electrolytic oxidation. *Applied Surface Science, 200* (1–4), 172-184.

Yerokhin, L., Snizhko, L. O., Gurevina, N. L., Leyland, A., Pilkington, A. & Matthews, A. (2003). Discharge characterization in plasma electrolytic oxidation of aluminium. *Journal of Physics D-Applied Physics, 36* (17), 2110-2120.

Zhang, X. L., Jiang, Z. H., Yao, Z. P. & Wu, Z. D. (2010). Electrochemical study of growth behaviour of plasma electrolytic oxidation coating on ti6al4v: Effects of the additive. *Corrosion Science, 52* (10), 3465-3473.

Zum Gahr, K.-H. (1987). Classification of wear processes. In *Tribology series: Microstructure and wear of materials* (80-131): Netherlands: Elsevier.